UNIVERSITY OF CALIFORNIA
Los Angeles

Seeking Supershear Earthquakes

A dissertation submitted in partial satisfaction
of the requirements for the degree
Doctor of Philosophy in Geophysics and Space Physics

by

Han Bao

2022

ABSTRACT OF THE DISSERTATION

Seeking Supershear Earthquakes

by

Han Bao
Doctor of Philosophy in Geophysics and Space Physics
University of California, Los Angeles, 2022
Professor Lingsen Meng, Chair

Supershear earthquakes, whose rupture speeds are faster than that of the seismic shear waves, can be highly destructive owing to the associated strong ground shaking. These events are rare, and understanding why they occur may provide insights into fault mechanics. However, identified samples of supershear earthquakes are rare, which hinders systematic analysis of their mechanism. In this work, I optimized observational methods and applied them to find more supershear earthquakes. Eventually, a global survey of earthquake rupture speeds reveals that supershear earthquakes occur much more frequently than previously thought. Our findings provide a much greater basis for evaluating the conditions favourable for driving supershear rupture. We observe that supershear rupture is more common along faults that separate oceanic and continental plates. These oceanic–continental supershear events also generate rupture in the same relative direction as the stiffer fault block moves. We find that fault zone width is thicker in regions where supershear earthquakes occur, and that supershear ruptures occur relatively frequently in mature oceanic transform faults. Our works confirm observations made from laboratory and numerical experiments and will be able to guide future research into these destructive earthquakes.

The dissertation of Han Bao is approved.

Sylvain Barbot

Caroline Denise Mari Boyce

Gilles F. Peltzer

Lingsen Meng, Committee Chair

University of California, Los Angeles

2022

To my parents...

who made me who I am

To Guannan...

who taught me how to love and be loved

TABLE OF CONTENTS

LIST OF FIGURES

ACKNOWLEDGMENTS

To me, my Ph.D. is not just five years of learning how to do research and science but also a process to learn how to live a life, to be a man, to reform my weakness, and to be more all-round. Now it comes the time to say thank you and goodbye, and I want to take this opportunity to express my sincere gratitude to those who have ever encouraged me, helped me, and had faith in me.

Firstly, I owe a great deal to the many great advisors and mentors in the academic field. I thank Lingsen Meng for his almost unconditional support and for encouraging my varied pursuits. I thank him for guiding me into the observational seismology field and providing me with tools and resources whenever needed. I thank Gilles Peltzer for his guidance and mentoring in my pursuit of interest in remote sensing and radar imaging. He provided me with financial and intellectual support that helped me see the beauty of Earth science from a broader view and helped me expand my research territory. I thank Sylvain Barbot, who offered me the opportunity to give my first invited talk at a conference, which made me feel appreciated in the early years of my Ph.D. program. His encouragement made me more motivated, dedicated, and hardworking. I learned fasting from him, which partially helped me deal with my mental struggles in 2020 and 2021. To Jean-Paul Ampuero, a giant scientist in the Earthquake science community, whom I was lucky to work with, showed me what a great scientist and a leader should look like. I have admired him and seen him as a role model since our first collaboration. I thank him for teaching me all those transferable skills: communication, writing, teamwork, relationship building, and, most importantly, leadership. To David Jackson and Peter Bird, whom I had the opportunity to work with on earthquake forecasts, I thank them for their scientific mentoring and for sharing their life wisdom with me. To Caroline Beghein, who taught me my favorite course at UCLA, Inverse Theory.

I also want to thank my coauthors, collaborators, and senior scientists who offered me kindness, inspiration, and strength. Thanks to Ryo Okuwaki, whom I would often go to first

whenever I discovered something new or exciting. He is like a friend, a big brother, and a mentor whom I looked upon in the early years of my Ph.D. To Baoning Wu, who always encouraged and inspired me and, most importantly, taught me to be humble and empower people around me. I want to thank other professors who saw the stars in my eyes: Kelin Wang, Nadia Lapusta, Thorne Lay, Huajian Yao, Ares Rosakis, David Oglesby, Haijiang Zhang, and Bin Liu. I also benefit significantly from other colleagues and friends in the field: Haiyang Kehoe, Huihui Weng, Bo Li, Luca Del Zilio, Sayyed Mirzadeh, William Savran, Jose Bayona, Yijun Zhang, Tong Zhou, Sunyoung Park, Simran Sangha.

Thanks to all the UCLA people for helping make the past five years of my life memorable. To my groupmates: Tian Feng, Liuwei Xu, Yuqing Xie, Ailin Zhang, Hui Huang, Saeed Mohanna, and Zhipeng Liu. To my great friends in LA: Akash Gupta, Tyler Powell, Yufan Xu, Kevin Shao, Leslie Insixiengmay, Ariel Graykowski, Xiyuan Bao, Abijah Simon, Erik Weidner, and Valeria Jaramillo.

To the teachers who had faith in me: Lixin Wang, who encouraged and inspired an undisciplined 16-year-old boy's ambition with both strict and warm; Jianhua Liu, who wrote me a rec-letter to Tsinghua University when I had nothing but dreams; Zheng Li and Mengdi Xia, who sparked the fire inside me to pursue academic excellence. To the many other friends whom I share priceless friendships with and who helped me develop as a person in the early years: Yong Tian, Dongyuan Li, Xinze Jiang, Jiazhu Zhu, Yisu Huang, Guiran Liu, Rubo Chen, Xinyu Dou, Boren Zhang, Yi Zhang, Jiagen Li, Kaixin Yuan, Zeyu Jin, Yi Xie, Huazhi Ge, and Tianyi Li.

To my mentors and friends in the business world: Yang Bai, who guided me into the world of management consulting; Aric Zhang and Henry Li, who offered me opportunities to learn business analysis and strategic way of thinking; Terry Zhang, Annie Zhang, Laura Chen, Yang Liu, Huan Yang, Amanda Deng, and Kay Tang, who mentored and coached me in the early stage; Anita Shao, Tao Wang, Peter Li, Yao Xiao, Huanyu Xiao, Jeehae Kim, and Andrian Lee who are like comrades in arms to me and with whom I shared hundreds

of hours fighting wars in the battlefield of business cases. To my McKinsey colleagues and mentors: Grace Shen, Xiaofan Wang, Gefei Li, Ye Yuan, Bingyue Zhang, Crystal Yu, Yutong Li, Guannan Liu, Sarah Zhang, William Yu, and Yining Xu. To Cissy Zhao and Liangcheng Zhou, who welcomed and supported me into the venture capital world. In particular, I want to thank Anita Shao, with whom we designed and lectured a 10-week Business Case Interview Bootcamp to more than 300 advanced degree scholars (PhD/JD/MD/Postdoc) from seven top universities in California (UCLA/Caltech/Stanford/USC/UCSD/UCB/UCSF). I want to thank Sophie Le, with whom we had our first startup company, ImpactPharm.

To giants and mentors out there, from whom I learned great wisdom about the world and ourselves as humans. To Giulia Sissa, who introduced me to the masterpieces of Thomas Hobbs and Niccoló Machiavelli. To David Wilkinson, who taught me Realism and Idealism and introduced me to John Mearsheimer. To Kelly McGonigal, from whom I learned willpower training, to better understand how our brain tricks us and thus better mind and body control. To Jeff Warran and Jon Kabat-Zinn, from whom I learned mindfulness meditation. To Andrew Huberman, from whom I learned better mind and body control by proactively interfering with the autonomic neural system. To Marvin Bower, from whom I learned the golden rules of leadership.

Finally, to my family. To my mom, who embraced me with great love, and from whom I learned to understand people. To my dad, who infused iron and fire in my heart and taught me to be tough and competitive. To my dear grandma, whom I miss so much, for being the champion of my childhood. Last but not least, to Guannan Dong, who's been by my side for eight years, for teaching me how to love and be loved. I am forever in your debt, and I wish you the best on your new journey.

VITA

2013–2017 B.S. in Geophysics, University of Science and Technology of China, Hefei, China

2017–present Ph.D. student in Geophysics and Space Physics, UCLA, Los Angeles, California

PUBLICATIONS

Meng, L., **Bao, H.**, Huang, H., Zhang, A., Bloore, A., & Liu, Z. (2018). Double pincer movement: Encircling rupture splitting during the 2015 Mw 8.3 Illapel earthquake. Earth and Planetary Science Letters, 495, 164-173.

Bao, H., Ampuero, J. P., Meng, L., Fielding, E. J., Liang, C., Milliner, C. W., ... & Huang, H. (2019). Early and persistent supershear rupture of the 2018 magnitude 7.5 Palu earthquake. Nature Geoscience, 12(3), 200-205.

Meng, L., Huang, H., Xie, Y., **Bao, H.**, & Dominguez, L. A. (2019). Nucleation and kinematic rupture of the 2017 Mw 8.2 Tehuantepec earthquake. Geophysical Research Letters, 46(7), 3745-3754.

Mirzadeh, S. M. J., Jin, S., Parizi, E., Chaussard, E., Bürgmann, R., Delgado Blasco, J. M., Amani, M., **Bao, H.**, & Mirzadeh, S. H. (2021). Characterization of Irreversible Land Subsidence in the Yazd-Ardakan Plain, Iran From 2003 to 2020 InSAR Time Series. Journal of Geophysical Research: Solid Earth, 126(11), e2021JB022258.

Xie, Y., **Bao, H.**, & Meng, L. (2021). Source Imaging With a Multi-Array Local Back-Projection and Its Application to the 2019 Mw 6.4 and Mw 7.1 Ridgecrest Earthquakes. Journal of Geophysical Research: Solid Earth, 126(10), e2020JB021396.

Savran, W. H., Bayona, J. A., Iturrieta, P., Asim, K. M., **Bao, H.**, Bayliss, K., Herrmann, M., Schorlemmer, D., Maechling, P.J., & Werner, M. J. (2022). pycsep: A python toolkit for earthquake forecast developers. Seismological Society of America, 93(5), 2858-2870.

Xie, Y., Meng, L., Zhou, T., Xu, L., **Bao, H.**, & Chu, R. (2022). The 2021 Mw 7.3 East Cape earthquake: Triggered Rupture in Complex Faulting Revealed by Multi-Array Back-projections. Geophysical Research Letters, e2022GL099643.

Bao, H., Xu, L., Meng, L., Ampuero, J. P., Gao, L., & Zhang, H. (2022). Global frequency of oceanic and continental supershear earthquakes. Nature Geoscience, 1-8.

Zhang, Y., **Bao, H.**, Meng, L., & Aoki, Y. (2022) Understanding and Mitigating the Spatial Bias of Earthquake Source Imaging with Regional Slowness Enhanced Back-Projection. Journal of Geophysical Research: Solid Earth

CHAPTER 1

Introduction

1.1 Supershear Earthquakes

Seismologists now know that one of the important parameters controlling earthquake damage is the speed at which an earthquake fault ruptures, and changes in this rupture speed (Madariaga, 1977; Madariaga, 1983). The rupture speed can vary substantially, and this influences the severity of the ground motion associated with the earthquake (Dunham and Bhat, 2008). Sometimes ruptures can propagate faster than the seismic shear waves, which is known as supershear ruptures. Figure 1.1 shows permissible values of the rupture speed at different rupture modes, which are distinguished by the direction of slip relative to the rupture front. Mode II slip generates both shear and dilational waves and can propagate at supershear speeds (speeds faster than the S-wave speed).

Supershear earthquakes can cause localised, strong ground motion, even far away from the fault, as the radiated waves coalesce into a pair of beams (known as a Mach cone) that propagate obliquely from the fault. Figure 1.2 shows how waves from different parts of the fault interfere with each other and how shear wavefronts emitted when the rupture passes the solid dots. When the rupture is subshear, the wavefronts are concentrated in the forward direction and separated in the backward direction. This leads to larger amplitudes and higher frequencies in the forward direction. For supershear ruptures, the source outruns the waves and a Mach front is formed (Figure 1.2). Figure 1.3 illustrates wavefronts from a three-dimensional supershear rupture on a surface-breaking fault. The superposition of

waves from all points along the rupture front generates a Mach wedge capped at the bottom by half of a Mach cone. In addition to generating shear Mach waves, a surface breaking rupture also excites Rayleigh Mach waves. Rayleigh waves are surface waves comprised of evanescent shear and dilational waves; they propage at a speed slightly less than the S-wave speed. Consequently, a supershear source is also a super-Rayleigh one, so Rayleigh Mach fronts (dark blue lines) will appear on the free surface slightly behind the shear Mach fronts. Supershear events can be highly destructive owing to the associated strong ground shaking, and understanding why and how they occur provides insights into fault mechanics and seismic hazards assessment.

Ever since Reid's illustration of earthquakes as propagating ruptures (Reid, 1910), the analysis of rupture propagation speed came a long way from studying directivity effect and spectra of long-period seismic waves (Gutenberg, 1955; Benioff, 1955; Benioff et al., 1961; Ben-Menahem and Toksoz, 1963) to the modern seismology era where a broader frequency range are exploited within frameworks of forward and inverse modeling (S. Hartzell and Helmberger, 1982; Olson and Apsel, 1982; S. H. Hartzell and Heaton, 1983; Kikuchi and Kanamori, 1991) as well as grid-search for subsequent source locations (Spudich and Cranswick, 1984; Vallée et al., 2008; Bao et al., 2019). Such a development process has witnessed the first unrealistic supershear laboratory experiment (Wu et al., 1972), the birth of the Burridge-Andrew mechanism of supershear transition (Andrews, 1976; Burridge, 1973; Das and Aki, 1977), the first reported supershear event (Archuleta, 1984; Spudich and Cranswick, 1984), the 25-year quiescence before the revolutionary experiments led by Rosakis (Rosakis et al., 1999; Xia et al., 2004), and the theoretical and observational blossom of supershear rupture transition and propagation in the 21st century.

In the 1950–1960s, it was believed that earthquake ruptures could only reach the Rayleigh wave speed. This was based partly on very idealized models of fracture mechanics, originating from results on tensile crack propagation velocities which cannot exceed the Rayleigh wave speed and which were simply transferred to shear cracks. In the early 1970s, Wu et al.

(Wu et al., 1972) conducted laboratory experiments on plastic polymer, under very low normal stresses, and found supershear rupture speeds. This was considered unrealistic for real earthquakes, both the material and the low normal stress, and the results were ignored. Soon after, Burridge, 1973 demonstrated that faults with friction but without cohesion across the fault faces could exceed the shear wave speed and even reach the compressional wave speed of the medium. But since such faults are unrealistic for actual earthquakes, the results were again not taken seriously. In the mid- to late 1970s the idea that for in-plane shear faults with cohesion, terminal speeds exceeding not only the Rayleigh wave speed but even being as high as the compressional-wave speed was possible finally started being accepted, based on the work of Andrews, 1976, Das, 1976, and Das and Aki, 1977. Once the theoretical result was established, scientists interpreting observations became more inclined to believe results showing supershear fault rupture speeds, and at the same time the data quality and the increase in the number of broadband seismometers worldwide, required to obtain detailed information on fault rupture started becoming available. Thus, the theory spurred the search for supershear earthquake ruptures.

The first earthquake for which supershear wave rupture speed was inferred was the 1979 Imperial Valley, California earthquake which had a moment-magnitude (Mw) of 6.5, studied by Archuleta, 1984, and by Spudich and Cranswick, 1984 using strong motion accelerograms. But since the distance for which the earthquake propagated at the high speed was not long, the idea was still not accepted universally. And then for nearly 25 years there were no further developments, perhaps because earthquakes which attain supershear speeds are rare, and none are known to have occurred. This provided ammunition to those who resisted the idea of supersonic earthquake rupture speeds being possible.

Then, in the late 1990 to early 2000s, there were two major developments. Firstly, a group at Caltech, led by Rosakis, measured earthquake speeds in the laboratory, not only exceeding the shear wave speed (Rosakis et al., 1999; Xia et al., 2004) but even reaching the compressional wave speed (Xia et al., 2005). Secondly, several earthquakes with su-

pershear wave rupture speeds actually occurred, with one even reaching the compressional wave speed. The first of these was the strike-slip earthquake of 1999 with Mw 7.6 in Izmit, Turkey (Bouchon et al., 2000), with a total rupture length of 150 km, and with the length of the section rupturing at supershear speeds being about 45 km. This study was based on two components of near-fault accelerograms recorded at one station (SKR). Then two larger supershear earthquakes occurred, namely, the 2001 Mw 7.8 Kunlun, Tibet earthquake (Antolik et al., 2004; Bouchon and Vallée, 2003; Robinson et al., 2006; Vallée et al., 2008; Walker and Shearer, 2009), and the 2002 Mw 7.9 Denali, Alaska earthquake (Dunham and Archuleta, 2004; Ellsworth et al., 2004; Frankel, 2004; Ozacar and Beck, 2004; Walker and Shearer, 2009). Both were very long, narrow intraplate strike-slip earthquakes, with significantly long sections of the faults propagating at supershear speeds. At last, clear evidence of supershear rupture speeds was available. Moreover, by analysing body wave seismograms very carefully, Robinson et al., 2006 showed that not only did the rupture speed exceed the shear wave speed of the medium; it reached the compressional wave speed, which is about 70% higher than the shear wave speed in crustal rocks. Once convincing examples of supershear rupture speeds started to be found, theoretical calculations were carried out (Bernard and Baumont, 2005; Dunham and Bhat, 2008) and these suggested that the resulting ground shaking can be much higher for such rapid ruptures, due to the generation of Mach wave fronts. Such wave fronts, analogous to the "sonic boom" from supersonic jets, are characteristics and their amplitudes decrease much more slowly with distance than usual spherical waves do.

However, identified samples of supershear earthquakes are still rare, which prohibits systematically studying the kinematic and dynamic features of previous supershear earthquakes. Until the year of 2019, only eight shallow strike-slip (mode-II) supershear ruptures have been occasionally reported, including the 1979 Imperial Valley (Archuleta, 1984; Spudich and Cranswick, 1984), 1999 Izmit and Düzce (Bouchon et al., 2001), 2001 Kunlun (Antolik et al., 2004; Bouchon and Vallée, 2003; Vallée et al., 2008; Walker and Shearer, 2009), 2002

Denali (Ellsworth et al., 2004; Frankel, 2004; Ozacar and Beck, 2004; Walker and Shearer, 2009), 2010 Yushu (Wang et al., 2012), 2013 Craig (Yue et al., 2013), and 2018 Palu (Bao et al., 2019) earthquakes. There are a few more reported cases but remain arguable due to limited datasets and resolution, or disagreement between different groups (Duputel et al., 2012; Olsen et al., 1997; Sangha et al., 2017; Song et al., 2008; Wald and Heaton, 1994; Wang et al., 2012; Yue et al., 2012). Note that, only one deep supershear earthquake has been reported (Zhan et al., 2014), but we only consider crustal strike-slip earthquakes here. Moreover, reporting supershear earthquakes has never been a routine or effortless task and was prone to be questionable. Inferential studies deducing rupture speeds through forward or inverse modeling are subjected to nonunique solutions and trade-offs between source parameters (rupture size, rupture speed, slip, risetime). Although having stations right on a supershear segment or close to the fault can provide significant constraint (Archuleta, 1984; Ellsworth et al., 2004; Wang et al., 2012), it seldom was a granted case. On the other hand, direct measurement of slowness with local, regional array (Spudich and Cranswick, 1984; Vallée et al., 2008) or teleseismic source tracking (Walker and Shearer, 2009) can extract rupture speed independently from the slip but tend to suffer from many artifacts and spatial bias (Bao et al., 2019)].

The scarcity of observed supershear ruptures hinders systematic analysis of their mechanisms while leaving the appearance that they are rare in nature (Bouchon et al., 2010; Das, 2015; Passelègue et al., 2013). More specifically, the lack of statistical analysis makes it difficult to validate theoretical findings and to address questions such as the following: Do structural features control the occurrence of supershear ruptures? For instance, do they happen more often on faults with wider seismogenic widths? Do they have a preferred propagation direction due to bimaterial effects? Can they propagate at sub-Eshelby speeds (slower than $\sqrt{2}$ times S-wave speed)?

Through out my Ph.D. study, I have been working on two things: (1) optimizing observational methods that can help better identify supershear ruptures, namely, the Slowness-

Enhanced Back-Projection (SEBP) and surface Mach Waves; and (2) apply such methods to find more supershear earthquakes. Such efforts enable me to conduct systematic investigations of supershear earthquakes in the past two decades and statistical analysis to validate theoretical findings of supershear ruptures.

1.2 Thesis Structure

Chapters 2, 4, 5, 6 and 7 of this thesis were originally written for individual publication. They can be read in isolation, but the main chapters are closely related to the theme of observations of supershear earthquakes.

Chapter 2, in full, is a reformatted version of the material as it is submitted to Journal of Geophysical Research: Zhang, Y., Bao, Han., Meng, L., Aoki, Y., Understanding and Mitigating the Spatial Bias of Earthquake Source Imaging with Regional Slowness Enhanced Back-Projection (2022). I was the primary investigator and author of this paper, in which we optimized the theory of the Slowness-Enhanced Back-Projection (SEBP) and investigated the uncertainties of SEBP.

Chapter 3 introduces the surface Mach Wave method that I extensively applied to identify supershear ruptures. Surface Mach waves is a unique signature of supershear ruptures, which can be effectively identified in the far-field surface wavefield. Through synthetic tests, we gained a better understanding of this method and designed an optimized version to identify Mach waves.

Chapter 4, in full, is a reformatted version of a section of the material as it appears in Nature Geoscience: Bao, H., Xu, L., Meng, L., Ampuero, J.P., Gao. L., Zhang, H., Global frequency of oceanic and continental supershear earthquakes. Nat. Geosci. (2022). https://doi.org/10.1038/s41561-022-01055-5. I was the primary investigator and author of this paper. For this part, we conducted comprehensive synthetic test to investigate uncertainties of Back-projection and extensively discuss how we applied synthetic tests to validate

rupture speed estimation using Back-projection.

Chapter 5, in full, is a reformatted version of the material as it appears in Nature Geoscience: Bao, H., Ampuero, JP., Meng, L., Fielding, E.J., Liang, C., Milliner, C.W.D., Feng, T., Huang, H., Early and persistent supershear rupture of the 2018 magnitude 7.5 Palu earthquake. Nat. Geosci. 12, 200–205 (2019). https://doi.org/10.1038/s41561-018-029. I was the primary investigator and author of this paper, in which we identified a supershear rupture speed of the 2018 magnitude 7.5 Palu earthquake.

Chapter 6, in full, is a reformatted version of the material as it appears in Nature Geoscience: Bao, H., Xu, L., Meng, L., Ampuero, J.P., Gao. L., Zhang, H., Global frequency of oceanic and continental supershear earthquakes. Nat. Geosci. (2022). https://doi.org/10.1038/s41561-022-01055-5. I was the primary investigator and author of this paper, in which we conduct a global investigation of earthquake rupture speeds and reveal that supershear earthquakes occur much more frequently than previously thought.

Chapter 7, in full, is a reformatted version of a section of the material as it is submitted to Journal of Geophysical Research: Zhang, Y., Bao, Han., Meng, L., Aoki, Y., Understanding and Mitigating the Spatial Bias of Earthquake Source Imaging with Regional Slowness Enhanced Back-Projection (2022). I was the primary investigator and author of this paper. For this part, we showed that besides supershear earthquakes, we can also apply back-projection on other kinds of rupture kinematics. In particular, we applied Slowness-enhanced Back-projection on the 2011 Tohoku earthquake, we find that high-frequency radiators did not reach beyond the down-dip limit of interplate seismicity, indicating that it is likely that the coseismic slip did not penetrate into the brittle-ductile transition zone. Such observations suggest that the enhanced dynamic weakening mechanism due to thermal pressurization effects may not be activated during the Tohoku earthquake as is proposed for other large earthquakes that penetrated the roots of seismogenic zones.

Finally, in Chapter 8, we briefly summarize the main findings presented in this thesis and discuss future perspectives following my work.

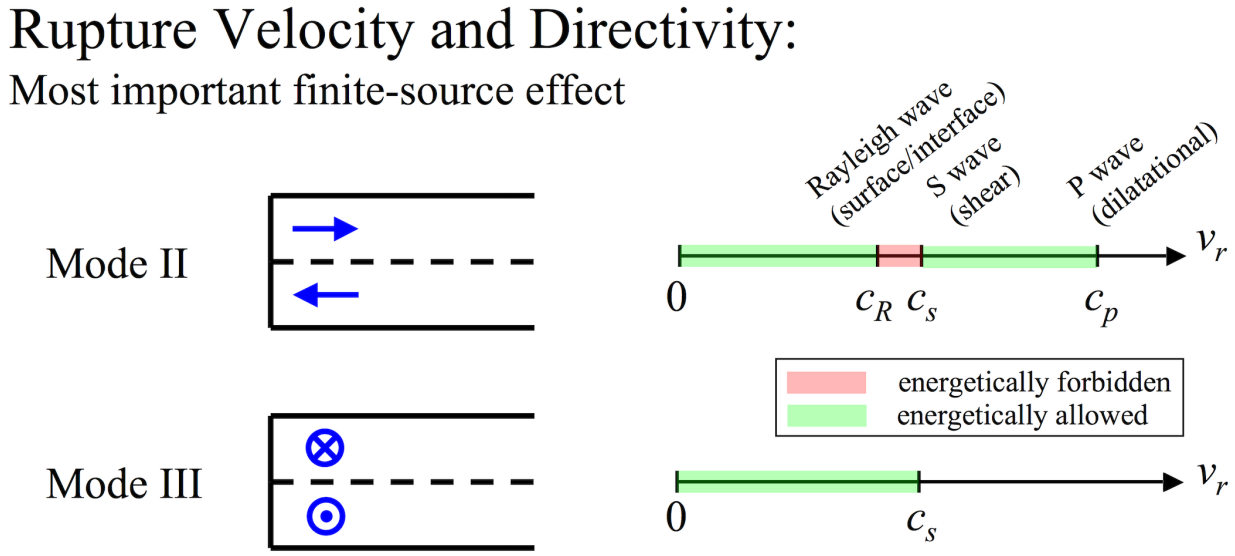

Figure 1.1: (credit to Eric Dunham) Permissible values of the rupture speed, v_r, are determined by the rupture mode. There are two modes of shear rupture, which are distinguished by the direction of slip relative to the rupture front. The blue arrows indicate the displacement of the two sides of the fault (the fault is the dashed line). Slip in mode III ruptures excites only shear waves, so the S-wave speed, c_s, becomes the limiting rupture speed in this geometry. Mode II slip generates both shear and dilational waves, which can interact in rather interesting ways (e.g., to produce Rayleigh surface waves). Mode II ruptures typically propagate below the Rayleigh speed, c_R, but can also propagate at intersonic speeds (speeds between the S-wave speed, c_s, and the P-wave speed, c_p).

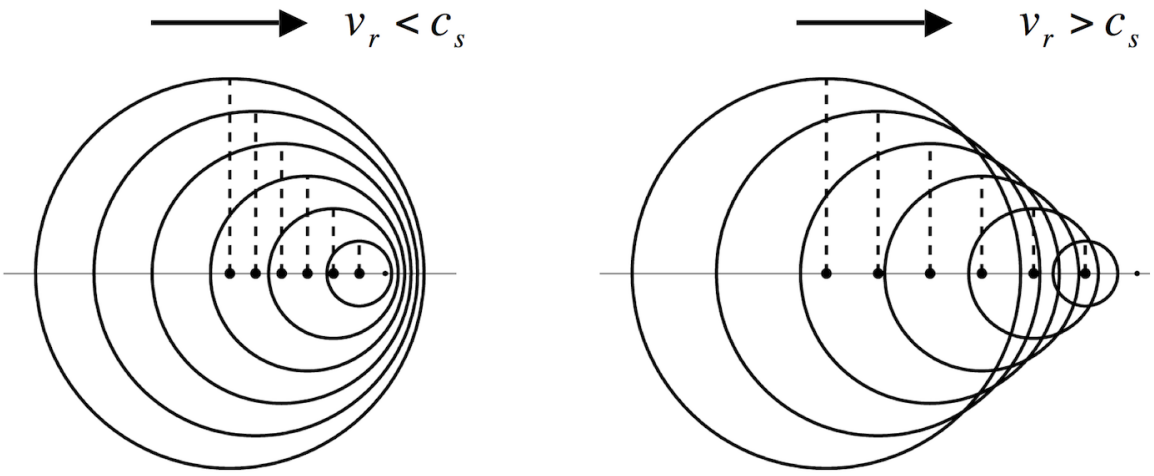

Figure 1.2: (credit to Eric Dunham) Wavefronts from a two-dimensional subshear (left) and supershear (right) rupture on a linear fault. Each point along the rupture emanates shear waves. When the rupture speed is slow than the shear wave, the first arrival in the rupture front direction come from the earliest ruptured point; however, when the rupture speed is faster than the shear wave, the first arrival in the rupture front direction come from the latest ruptured point. As a result, supershear ruptures generate two surface wave fronts on each side that propagate at the wave speeds.

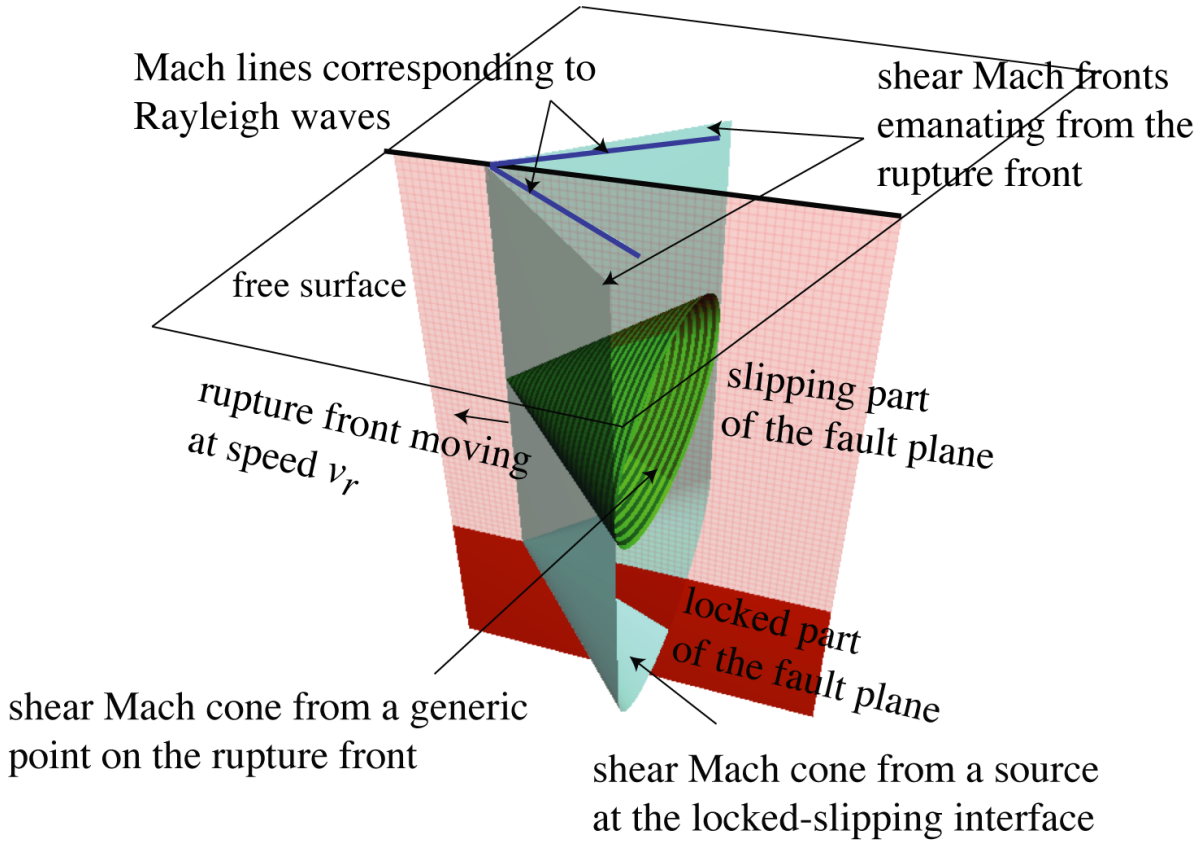

Figure 1.3: (credit to Eric Dunham) Wavefronts from a three-dimensional supershear rupture on a surface-breaking fault. Each point along the rupture emanates shear waves in the form of a Mach cone (green). The superposition of waves from all points along the rupture front generates a Mach wedge capped at the bottom by half of a Mach cone (light blue). In addition to generating shear Mach waves, a surface breaking rupture also excites Rayleigh Mach waves. Rayleigh waves are surface waves comprised of evanescent shear and dilational waves; they propage at a speed slightly less than the S-wave speed. Consequently, a supershear source is also a super-Rayleigh one, so Rayleigh Mach fronts (dark blue lines) will appear on the free surface slightly behind the shear Mach fronts.

CHAPTER 2

Slowness Enhanced Back-projection

Abstract

We investigate characteristics of spatial biases in the Back-projection method and the effectiveness of the Slowness Enhanced Back-projection (SEBP). Here, the spatial bias refers to the location error in Back-projection caused by travel time errors due to heterogeneous 3D Earth structure. SEBP reduces such bias by calibrating the gradient of travel time (slowness) in the source estimated from aftershock data. Using the Command Island region, Alaska, as a test area, we analyze 22 evenly distributed M4-M6 earthquakes. We find a systematic correlation between the amplitude of the spatial bias and the event separation distance (distances between reference and investigated events) which justifies the calibration based on slowness. Previous SEBP assumes uniform slowness across the entire source zone. Here, we find that for a large event (rupture length $>$ 150 km), the amplitudes and directions of spatial biases follow distinct regional patterns corresponding to each fault segment. In light of this, we propose a regional SEBP approach that introduces spatially variable slowness correction. The regional SEBP in the test area resulted in a $\sim$ 50% reduction in the average length of spatial bias, from $\sim$20 km to $\sim$10 km, which is more effective than the uniform SEBP that gives a 25% error reduction.

2.1 Introduction

Back-projection (BP) is an observational technique that tracks growth of large earthquake ruptures from coherent seismic phases recorded across a seismic array (see Kiser and Ishii, 2017 for a comprehensive review of BP). High-frequency rupture characteristics resolved from BP provide unique perspectives on understanding detailed rupture kinematics and geometrical complexities of large earthquakes (Bao et al., 2019; Fukahata et al., 2013; Ishii et al., 2005; Kiser and Ishii, 2011; Meng et al., 2012; Meng et al., 2018; Meng et al., 2019; Okuwaki and Yagi, 2018; Okuwaki et al., 2014; Satriano et al., 2012; Wang and Mori, 2011). Recent studies also demonstrated the effectiveness of the BP method in detecting and locating seismicity (Fan and Shearer, 2016; Feng et al., 2020; Kiser and Ishii, 2011).

However, previous studies found that locating seismicity using BP suffers from notable spatial bias, De, defined as the vector deviation between an event's BP inferred (BPI) location from its catalog location. The event catalog locations are usually relocated with local or regional networks and are thus considered to be more accurate than BPI locations. The uncertainty of BPI location is attributed to both the noise and travel time errors. Since the ambient noise is weak compared with the waveform amplitude of M>6 earthquakes imaged with BP, the noise relevant to BP refers to the incoherent part of the waveforms caused by coda waves, local scattering, and variation of site effects. Xu et al., (2022) shows that the perturbation of BPI location due to noise is on the order of 1 - 4 km depending on the noise amplitude and the array aperture. A bigger source of De is the travel time errors introduced by approximating the 3-D Earth velocity structure with a 1-D reference model. Previous teleseismic BP studies in Tohoku, Nepal, Mexico, and Chile found the spatial bias associated with travel-time errors is on the order of 20 - 30 km (Fan and Shearer, 2017; Meng et al., 2019; Meng et al., 2016; Palo et al., 2014). In addition to BP spatial bias, waveform complexity such as water reverberation and coda waves generated by near-trench 3D structures also leads to artificial sources in BP imaging (Zeng et al., 2019). The structural effect also distorts the

BP amplitude. Okuwaki et al., 2019 shows that the amplitude variation of Green's functions results in depth-dependent intensity of BP sources along a subducting plate interface.

Understanding spatial biases of BP is of significance not only for detecting and locating epicenters of earthquakes but also for observational studies of large earthquakes. This is because spatial biases can distort measurements of rupture properties (e.g. rupture lengths, speeds, and directivities), and thus result in erroneous interpretations of earthquake physics (Bao et al., 2019). Since the spatial biases are primarily caused by our insufficient knowledge of the 3D velocity heterogeneity, several studies attempted to calibrates the travel times using aftershocks near the mainshock rupture (Ishii et al., 2007; Meng et al., 2016; Palo et al., 2014). For instance, Ishii et al., 2007 measured the time shifts to align the aftershock arrivals and obtained the time correction for a given source grid point from weighted-average of the nearby aftershock measurements. Palo et al., 2014 further separated the travel time correction into two terms: a static term specific to a station and a dynamic term specific to each pair of source grid point and a station. The dynamic term is obtained by interpolating time shifts of aftershocks over the source area. The aftershock calibration typically requires moderate-size events (M 4.5 - 6) which are small enough to be approximated as a point source in the far-field yet large enough with sufficient Signal-to-Noise ratio (SNR) at the teleseismic receivers. A practical limitation is sparsity and uneven distribution of such aftershocks which may lead to unreliable correction if the travel times are interpolated empirically. Alternatively, Meng et al., 2016 developed a parametric approach named Slowness Enhanced Back-projection (SEBP). Instead of direct spatial interpolation of the travel times, a slowness correction term (spatial gradient of travel-time) is derived from the aftershock measurements. The total travel-time correction for a given source grid point includes the static term and the vector product of the source location and the slowness term. This slowness term is assumed to be uniform for the whole rupture region. Although SEBP has been applied to several large earthquakes with rupture length less than 150 km (Bao et al., 2019; Meng et al., 2018; Meng et al., 2019; Meng et al., 2016; Sangha et al., 2017), the effectiveness of using a uniform

slowness correction term has not been systematically investigated for earthquakes of larger sizes.

To investigate the pattern of spatial biases in large source regions, we studied the Commander Island region (Figure 2.1), which spans more than 400 km along the western Aleutian trench. We analyzed 22 M 4-6 earthquakes that occurred from 2013 to 2017. We found a systematic correlation between the amplitude of De and the event separation distance which justifies the condition to apply slowness correction. We also found that the amplitudes and directions of De follow distinct regional patterns corresponding to each fault segment, likely caused by variations of the regional velocity structures. Our results suggest that it is challenging to effectively calibrate travel time errors for the entire source region with a uniform slowness correction term. Therefore, we propose a regional Slowness Enhanced Back-projection (SEBP) approach that introduces spatially variable slowness corrections. By applying regional SEBP to the Commander Region, we found that the average of De reduced by 50% (from ∼20 km to ∼10 km), more effective than the 25% error reduction of uniform SEBP.

Investigation of Spatial Biases in the Commander Island Region

Data

To investigate characteristics of BP's spatial biases, we studied 22 moderate earthquakes (M 4-6) within the Commander Island region that occurred from 2013 to 2017 (Figure 2.1). We selected this region because of the abundance of moderate size earthquakes (M4 - 6) along the Bering Fault, the boundary between the Bering Plate and the Commander Island belt (DeMets et al., 1990). Moderate-size earthquakes have relatively high SNR so that their source locations can be well resolved by BP. Since the source region is far from densely distributed seismic networks, the global catalog locations of the investigated earthquakes may have large uncertainties. Because accurate event locations are crucial for the calibration

of SEBP, we performed teleseismic double-difference relocation to the nearby earthquakes (Pesicek et al., 2010). For the BP analysis, we adopted the waveforms of 336 stations in continental US which provide a large range and azimuthal coverage (Figure 2.1). We select stations with epicentral distances between 30° to 90°, such that waveform complexity caused by mantle discontinuities and the core-mantle boundary are absent, and that the contaminations of P_{diff} phase are not included.

Waveform data are downloaded from the Data Management Center (DMC) of the Incorporated Research Institutions for Seismology (IRIS) (https://ds.iris.edu/wilber3). Results presented in the main text are obtained from seismic data that are normalized and aligned by first P arrival and filtered to 0.5 - 2.0 Hz. Two other frequency bands (0.05 - 0.5 Hz and 1 - 4 Hz) are also used for comparative analysis which can be found in the supplementary material. We ensure that for a given event, the chosen stations are away from its nodal plane and share the same P-wave polarity. We adopt this quality control criteria to isolate the effect of travel time errors on BP spatial bias from station configuration.

We applied two BP methods: the classic beamforming BP (Ishii et al., 2005) and the MUSIC BP (Meng et al., 2011). Theoretical travel times are calculated from the layered IASP91 velocity model (Kennet, 1991), and the "reference window" strategy (Meng et al., 2012) are used to mitigate the "swimming" artifacts, a smearing artifact in images along the direction toward the arrays due to the trade-offs between the radiation origin times and source-receiver distances (Koper et al., 2012). Results presented in the main text are produced by MUSIC BP, and those of beamforming BP can be found in the supplementary material for comparison.

Obtaining the Spatial Bias

Since investigating BP's spatial uncertainty is the key focus of this study, we first provide a clear definition of the spatial bias of BP and how it is obtained. To account for the travel time variations due to 3D Earth structures, BP routinely adopts a timing correction

derived from the "hypocenter alignment" (Ishii et al., 2005, 2007). The first arrival of the mainshock is assumed to come from the hypocenter. A set of travel time errors due to 3D structures is obtained by cross-correlating the initial P-waves. Such "hypocenter correction" is usually applied to the entire rupture region. However, since it is only accurate within close proximities to the hypocenter, it does not account for the variation of travel time errors at distant source locations. Here, we consider *De* as the additional location error after applying the "hypocenter correction".

To guarantee accurate estimations of De, we first ensure that the hypocenter alignment is performed properly and has no influence on measurement of De. After the waveforms are downloaded, they are first aligned based on travel times predicted by a 1-D reference Earth velocity model (e.g. IASP91). We then adopt an iterative cross-correlation approach to align the waveforms of initial P-arrivals from low to high frequency bands. In the example shown in Figure 2.2, the waveforms are first aligned at 0.05 - 0.2 Hz in a 20-sec window and then aligned at 0.2 - 1 Hz in a 10-sec window. This procedure is repeated for 0.5 - 2 Hz if SNR is higher than 0.5. In order to avoid cycle skipping issues, we limit the maximum allowed shift to the period of the upper-bound of the frequency band. We further found that the position of the cross-correlating window is nontrivial. Although the peak amplitude is often more easily identified than the P-arrival, we note the cross-correlating window should be centered at the P-arrival, not P-wave's peak amplitude, because the first arrival comes from the hypocenter of an earthquake. This is likely more important for M 6+ events since their finite source effects are not negligible, and their centroid locations corresponding to the peak energy may have considerable deviations from their hypocenters. If the hypocenter alignment is performed correctly, a BP on the reference event itself (self-aligned BP) should collocate with its catalog location. Figure 2.2 shows the self-aligned BP of a Mw 6.3 earthquake when the cross-correlating window is centered at the maximum amplitude of waveforms versus that centered at the P-arrivals. In the former case, its BPI location (center of the integrated energy contours of the first 10 sec BPs) is 10-13 km away from the epicenter. In the latter

case, such deviations are less than 1 km, which is negligible. The process in BP of determining locations of earthquakes or sub-sources with respect to the hypocenter is similar to that of the "master event" location technique (Ito, 1985). Once the hypocenter correction is obtained for a "reference event", it is applied to the waveforms of "investigated events" to obtain their BPI locations (relative to the reference event). Based on a similar argument of finite source effects, the data window corresponding to the BPI location should also be centered at the P-arrival, not the peak amplitude. In Fan & Shearer (Fan and Shearer, 2017), many of their self-aligned BP locations deviate from their catalog locations. This is likely caused by two factors. First, their cross-correlating window is not centered at P-arrivals. Second, they used a 20-sec data window, longer than the durations of the investigated events. Therefore, the resulting BPI locations are more consistent with the centroid locations, not the hypocenter locations. Figure S2 shows the comparison when different data window lengths are applied. We conclude that it is optimal to use a 10 sec window centered at P-arrival for both the hypocenter alignment and obtaining BPI locations, demonstrated by the co-location between self-aligned BP and hypocenter location. Finally, we obtain the spatial bias by calculating the difference between the BPI location and the catalog location, similar to that of Fan & Shearer (Fan and Shearer, 2017). We here treat seismic relocated catalog as the ground truth because of the small errors of their relative locations ($\sim$ 1 km, Pesicek et al., 2010). Figure S3 gives an example for a M5.5 earthquake, the comparison of BP results when different BP parameters (stacking and integrating window lengths) are applied. We can see that various lengths of stacking window and integrating windows in BP method invariably located the kernel center of self-aligned BP images at its hypocenter, which is likely due to the fact that a M5.5 earthquake can be regarded as a point source at teleseismic distances. It suggests that as the finite-fault effect of M5 earthquakes can be ignored at teleseismic distances, they can be well resolved in spite of the variation of BP parameters.

Regional Patterns of Spatial Biases in the Commander Island Region

Figure 2.3 shows an example of spatial biases in the Commander Island region, where the BP energy contours and De are plotted for a Mw 6.3 earthquake used as a reference event. We select 9 M5+ reference events with relatively high SNR. In total, we analyze 22 events and 198 event pairs.

We found that spatial biases (De) in Commander Island have an average amplitude of 21 km and manifest regional patterns in terms of both their directions and amplitudes. As shown in Figure 2.3b, De have distinct characteristics in the north-west, middle, and the south-east parts of the study area. We segmented the investigated area into three sub-regions (Figure 2.1) and plotted the 198 measurements of De in polar diagram (Figure 2.4). Figure 2.4 shows patterns of directivities and amplitudes of De when regions of reference events and regions of investigated events are outlined. Measurements of De are plotted as bars in the polar plot. For convenience, we use a notation "R1→R2" to represent cases when reference events from region 1 are used to estimate De of events in region 2. In each polar plot, the mean value of De is marked (thick dashed line). In terms of amplitude of De, we found that the mean value of De of R1→R1 (R2→R2 / R3→R3) is 12.2 km, which is ∼50% smaller than 23.1 km of R2→R1 or R3→R1 (R1→R2 or R3→R2 / R1→R3 or R2→R3). In terms of directivies of De, for example, we found that R1→R2 is dominated by De offsetting northtoward; R1→R3 is dominated by De offsetting towards east; R2→R1 is dominated by De offsetting towards south; and both R3→R1 and R3→R2 are dominated by De offsetting towards north-east. Such regionalized features of De may be caused by segmented faulting and velocity structure beneath source regions (Figure 2.1). This finding is somewhat confirmed by Ruppert et al. (Ruppert et al., 2012) who found different zones of seismotectonic activities based on distributions of focal mechanisms in the Commander Island region. In the northwest of our investigated region near Bering Island (169°-170°E, R1 in Figure 2.1), right-lateral strike slip displacements are predominant with strike angles subparallel to the island chain (Newberry et al., 1986). A sudden stress change occurred

in the southeast of the Mednyi Island around 170° E (170°-171ºE, R2 in Figure 2.1), where diverse focal mechanisms exist, including strike-slip events with strike angles subparallel to the elongated direction of the Mednyi island and reverse events whose strike angles are diverse. Then in the east of 171° E (171°-172ºE, R3 in Figure 1), the focal mechanisms experience another change, where the strike angles of reverse events become predominantly between northeast and east (Lutikov et al., 2019). As a result, such structural complexities may be associated with regionalized seismic structures beneath the source region resulting in different patterns of travel-time variations and De.

We found that the average amplitude of De in the Commander Island region is 21 km and there is a positive correlation between amplitudes of De and event separation distance (distances between reference and investigated events). Figure 2.5a shows the 198 measurements plotted as amplitude of De versus event separation distances. In the immediate proximity of a reference event (<150 km), the median De increases almost linearly with separation distance. This is somewhat expected for a slowness correction: if the reference and investigated events share a similar regional velocity structure different from the standard 1D velocity model adopted in BP, there exists a constant slowness error and the travel-time errors and hence De should be proportional to the event separation distance projected onto the direction of the slowness error. Since the orientation of the event separation varies for different reference and investigated event pairs, De is loosely, rather than strictly, proportional to the event separation distance. On the other hand, Figure 2.4a shows that when the event separation is greater than 150 km, De seems to plateau and ceases to increase with distance. Such observations indicate at a larger scale, the difference of velocity structures beneath the reference and investigated events is no longer negligible, and a consistent slowness error does not explain the stochastic variation of travel-time errors and De. The fact that De plateaus with distance suggests that the travel-time errors are capped by the maximum lateral velocity deviation from the standard 1D Earth model. To further understand the statistics of De, we modeled its probability distribution by fitting a generalized extreme value (GEV)

distribution (Fan and Shearer, 2017; McFadden, 1978) which measures the probability distribution of a large set of independent, identically distributed random values representing observations. The modeled GEV distribution can be used to more accurately estimate the means, medians, and standard deviations of De (Figure 2.5d).

2.2 The Slowness-Enhanced Back-Projection

2.2.1 Method

In light of the regional patterns of De, we propose to modify the Slowness-Enhanced Back-projection (Meng et al., 2016). Our strategy is to divide a large source region, in this case, a region longer than 400 km, into sub-regions. Within each sub-region, a uniform slowness correction is derived and applied. We briefly describe our methodology in detail below.

In standard BP analysis, delay and sum of coherent seismic phases are used to obtain BP images:

$$BP(\xi, t) = \sum_j u_j \left(t + T_j^{mod}(\xi) + \delta T_j(\xi)\right) \tag{2.1}$$

where $BP(\xi, t)$ is the stacked beamforming power at a potential source location ξ as a function of time t, which can be expressed as a sum over n seismograms. u_j is the normalized seismogram at the j^{th} station, $T_j^{mod}(\xi)$ is the theoretical travel time from the source location ξ to the j^{th} station derived from a reference model, and T_j is the travel time error that accounts for the difference between the assumed Earth model and the real Earth velocity structure, which represents the changes in the wavefront curvature and incident angle at the receiver side. The stack $BP(\xi, t)$ estimates seismic energy released at each time t for all potential source grids, and the location ξ that yields the highest coherence and highest stacked power will be marked as the most likely source location at time t. For large earthquakes, by combining $BP(\xi, t)$ from the whole source time period, one can obtain the spatial-temporal evolution of the earthquake in seismic radiation.

Following eq. (2.1), the routinely performed "hypocenter correction" measures $T_j(\xi_h)$ by aligning the initial phase with cross-correlations assuming that the first-arrival originates from the hypocenter ξ_h. Most BP studies assumed that $T_j(\xi_h)$ is applicable for the whole source region, i.e.,

$$\delta T_j(\xi) \approx \delta T_j\left(\xi_h\right) = T_j\left(\xi_h\right) - T_j^{\mathrm{mod}}\left(\xi_h\right) \tag{2.2}$$

However, $T_j(\xi_h)$ is only exact in the vicinity of the hypocenter, which is why spatial biases exist. Previous applications of slowness calibrations show that spatial biases in one source region follow certain patterns: gradual changes of deviation amplitudes with similar deviation directions (Bao et al., 2019; Meng et al., 2019; Xie et al., 2021). Therefore, we can expand eq. (2.2) to account for the distance away from the hypocenter ξ_h using the first-order Taylor expansion:

$$\delta T_j(\xi) = \delta T_j\left(\xi_h\right) + \delta\left(\frac{\partial T}{\partial \xi}\right)_j\Bigg|_{\xi_h} \cdot \left(\xi - \xi_h\right) = \delta T_j\left(\xi_h\right) + \delta s_j \cdot \left(\xi - \xi_h\right) \tag{2.3}$$

We define $\delta(\frac{\partial T}{\partial \xi})$ as δs, the spatial derivatives of travel time errors at the source area, which shares the same unit of [s/km] as slowness. The product of δs and $(\xi - \xi_h)$ can be considered as an inner product of two vectors with respect to the three components (latitude, longitude, and depth):

$$\delta T_j(\xi) - \delta T_j\left(\xi_h\right) = \delta s_j^{NS} \cdot \left(\xi - \xi_h\right)^{NS} + \delta s_j^{EW} \cdot \left(\xi - \xi_h\right)^{EW} + \delta s_j^{UD} \cdot \left(\xi - \xi_h\right)^{UD} \tag{2.4}$$

where EW, NS, UD denote three orthogonal directions of East-West, North-South, and Up-Down, respectively. Because teleseismic travel time is not sensitive to the focal depth, we can simplify the equation by ignoring the 'vertical' component (UD):

$$\delta T_j(\xi) - \delta T_j\left(\xi_h\right) = \delta s_j^{NS} \cdot \left(\xi - \xi_h\right)^{NS} + \delta s_j^{EW} \cdot \left(\xi - \xi_h\right)^{EW} \tag{2.5}$$

Since cross-correlation alignment provides relative travel time correction to the reference seismogram, it will introduce a constant time shift with respect to the reference station. Usually, the choice of the reference station can be arbitrary and would not make any difference

because the differential travel time is self-consistent in cross-correlation. To eliminate such a constant time shift, we replace the travel time error $\delta T_j(\xi)$ with the relative travel time error $\delta \hat{T}_j(\xi)$:

$$\delta \hat{T}_j(\xi) = \delta T_j(\xi) - \delta T_{j_r}(\xi) \tag{2.6}$$

where $\delta T_{j_r}(\xi)$ is the travel time error of the reference station j_r, and eq. (5) can be re-written as:

$$\delta \hat{T}_j(\xi) - \delta \hat{T}_j(\xi_h) = \delta \hat{s}_j{}^{NS} \cdot (\xi - \xi_h)^{NS} + \delta \hat{s}_j{}^{EW} \cdot (\xi - \xi_h)^{EW} \tag{2.7}$$

Now, consider we have a group of aftershocks ($i = 1, 2, ..., M$), and their catalog locations are $\xi_i = \xi_1, \xi_2, ..., \xi_i, ..., \xi_M$. By applying the hypocenter correction, we can obtain their BPI locations ξ_i^{BP}. Considering ξ_i^{BP} as the equivalent of ξ_i in the reference velocity model, we have

$$T_j(\xi_i) - T_j(\xi_h) = T_j^{\mathrm{mod}}\left(\xi_i^{BP}\right) - T_j^{\mathrm{mod}}(\xi_h) \tag{2.8}$$

This approximation is supported by the fact that the difference in the two differential travel times between an aftershock and the mainshock hypocenter is an infinitesimal of higher order than the differential travel time itself. Then, the left-hand side of eq. (6) can be expended as

$$\begin{aligned}\delta \hat{T}_j(\xi_i) - \delta \hat{T}_j(\xi_h) = T_j(\xi_i) - T_j^{\mathrm{mod}}(\xi_i) - T_{j_r}(\xi_i) + T_{j_r}^{\mathrm{mod}}(\xi_i) \\ - T_j(\xi_h) + T_j^{\mathrm{mod}}(\xi_h) + T_{j_r}(\xi_h) - T_{j_r}^{\mathrm{mod}}(\xi_h)\end{aligned} \tag{2.9}$$

Inserting eq. (2.8) into eq. (2.9), we have

$$\delta \hat{T}_j(\xi_i) - \delta \hat{T}_j(\xi_h) \approx \hat{T}_j^{\mathrm{mod}}\left(\xi_i^{BP}\right) - \hat{T}_j^{\mathrm{mod}}(\xi_i) \tag{2.10}$$

Where

$$\begin{aligned}\hat{T}_j^{\mathrm{mod}}\left(\xi_i^{BP}\right) &= T_j^{\mathrm{mod}}\left(\xi_i^{BP}\right) - T_{j_r}^{\mathrm{mod}}\left(\xi_i^{BP}\right) \\ \hat{T}_j^{\mathrm{mod}}(\xi_i) &= T_j^{\mathrm{mod}}(\xi_i) - T_{j_r}^{\mathrm{mod}}(\xi_i)\end{aligned} \tag{2.11}$$

Validation of eq. (2.10) can be found in Supplementary Material Text S1 and Figure S6.

Combining eq. (2.7) and eq. (2.10), we have

$$\hat{T}_j^{\text{mod}}\left(\xi_i^{BP}\right) - \hat{T}_j^{\text{mod}}\left(\xi_h\right) \approx \delta\hat{s}_j{}^{NS} \cdot \left(\xi_i - \xi_h\right)^{NS} + \delta\hat{s}_j{}^{EW} \cdot \left(\xi_i - \xi_h\right)^{EW} \tag{2.12}$$

Now, the remaining unknowns, the slowness error vector $(\delta\hat{s}_j{}^{NS}, \delta\hat{s}_j{}^{EW})$ can be solved by a least-square inversion based on the time-shifts to align the aftershocks. These time-shifts can be obtained in the same fashion with the hypocenter correction. In practice, it is challenging to align the relatively small events (M 4-5.5) because of their low SNRs. We therefore use the differential travel-time of the BPI and event catalog location to infer the aftershock timeshifts.

However, for source regions as large as the Commander Island region and the Tohoku region, as we will see in the Results, spatial biases in different sub-regions have different patterns in terms of the amplitudes and directions. This indicates that a uniform slowness calibration over the entire source region can not effectively account for the spatial biases (Fan and Shearer, 2017; Palo et al., 2014). Therefore, we propose a regional SEBP approach that utilizes different slowness correction terms for each sub-region. Each sub-region k can be represented by its geometrical center ξ^k $(k = 1, 2, ...)$ and has its own center correction $\delta\hat{T}_j(\xi^k)$. Following eq. (2.7), for aftershocks ξ_i located in the region k, we have

$$\delta\hat{T}_j\left(\xi_i\right) - \delta\hat{T}_j\left(\xi^k\right) = \left(\delta\hat{s}_j^k\right)^{NS} \cdot \left(\xi_i - \xi^k\right)^{NS} + \left(\delta\hat{s}_j^k\right)^{EW} \cdot \left(\xi_i - \xi^k\right)^{EW} \tag{2.13}$$

which is equivalent to

$$\delta\hat{T}_j\left(\xi_i\right) - \delta\hat{T}_j\left(\xi_h\right) = \Delta\delta\hat{T}_j\left(\xi^k\right) + \left(\delta\hat{s}_j^k\right)^{NS} \cdot \left(\xi_i - \xi^k\right)^{NS} + \left(\delta\hat{s}_j^k\right)^{EW} \cdot \left(\xi_i - \xi^k\right)^{EW} \tag{2.14}$$

where

$$\Delta\delta\hat{T}_j\left(\xi^k\right) = \delta\hat{T}\left(\xi^k\right) - \delta\hat{T}_j\left(\xi_h\right) \tag{2.15}$$

denotes the difference between a geometrical center correction and the hypocenter correction. Using eq. (2.10), we can rewrite eq. (2.14):

$$\hat{T}_j^{mod}\left(\xi_i^{BP}\right) - \hat{T}_j{}^{mod}\left(\xi_i\right) = \Delta\delta\hat{T}_j\left(\xi^k\right) + \left(\delta\hat{s}_j^k\right)^{NS} \cdot \left(\xi_i - \xi^k\right)^{NS} + \left(\delta\hat{s}_j^k\right)^{EW} \cdot \left(\xi_i - \xi^k\right)^{EW} \tag{2.16}$$

Similar to eq. (2.12), the least-square inversion can solve for $\left[\Delta\delta\hat{T}_j\left(\xi^k\right), \left(\delta\hat{s}_j^k\right)^{NS}, \left(\delta\hat{s}_j^k\right)^{EW}\right]$. Then, the slowness correction can be mapped to obtain travel time corrections for all source grids. We demonstrate the effectiveness of SEBP in the following section, which is quantified by reductions of spatial biases.

2.2.2 The Effectiveness of the SEBP

We found that the regional SEBP effectively mitigates the spatial bias in the Commander Island region. Figures 5e 5f show the modeled GEV distribution of De after the uniform SEBP and regional SEBP is applied, respectively. We fit the GEV distribution to obtain location parameters (μ), scale parameters (σ), and shape parameters (κ), which help us to better estimate the means, medians, and standard deviations of De (Table S3). The location parameter reflects the position of the most frequent observation, while the scale parameter related to the kurtosis of observations reflect the sharpness of the distribution. Table S3 shows a reduction of the location parameter (μ) of GEV distribution by nearly 30% and 50% for the uniform SEBP and regional SEBP, respectively, compared to μ of the BP without calibration. The scale parameter (σ) is reduced by about 30% and 50% for the uniform SEBP and regional SEBP, respectively. These statistics suggest that when applying the regional SEBP, the GEV distributions of De became narrower and shifted towards the lower values (Figure 2.5e and 2.5f). We also found that the mean value of De for regional SEBP reduced from 21 km to 11 km, a 48% reduction, which is more significant than that of the uniform SEBP (24% reduction from 21 km to 16 km). Besides, Figures S7 and S8 show patterns of directions and amplitudes of De when uniform SEBP and regional SEBP are applied, respectively. For any pair of a reference and investigated region, while the directions of De are mostly similar, the average amplitudes of De for regional SEBP are shorter than that of the uniform SEBP.

2.3 Discussion and Conclusion

We systematically investigated the characteristics of De in the Commander Island as well as the effectiveness and limitation of the Slowness Enhanced Back-projection (SEBP). We found the average De in the region is $\sim$ 20 km, and the amplitude of De has a positive correlation with the hypocenter distance. We also found that the regional SEBP is more effective than the uniform SEBP and has reduced De by $\sim$ 50%, to an average value of $\sim$ 10 km. We argue that the requirement of the regional SEBP is likely due to the fact that the investigated source region is large (400 $\sim$ 500 km) and the velocity structures beneath the source region can not be considered uniform. It also suggests that the previous applications of the uniform SEBP (e.g., the 2015 Mw 7.8 Gorkha (Meng et al., 2016), the 2015 Mw 7.2 Tajikistan (Sangha et al., 2017), the 2015 Mw 8.3 Illapel (Meng et al., 2018), and the 2018 Mw 7.5 Palu earthquakes (Bao et al., 2019)) are likely due to their relatively small rupture length ($\leq$ 150 km) and hence smaller lateral velocity variation.

2.3.1 Travel-time Corrections of SEBP

The SEBP tackled the problem of spatial bias by mitigating the leading source of errors – travel time errors due to the 3-D Earth structure. Figure 9a shows an ideal scenario where wavefronts emitted from an event hypocenter $T^{mod}(\xi_h)$ at teleseismic distance are smoothly spherical and can be predicted under a 1D reference Earth model. In reality, the regional structure of the real Earth (blue shaded area) perturbs travel times and results in distorted wavefront $T(\xi_h)$ (Figure 2.6b). By aligning the first P wave arrivals, relative time errors $\delta T(\xi_h)$ of the ray paths originating from the hypocenter can be calibrated (i.e., hypocenter correction). However, as illustrated by Figure 2.6c, the hypocenter corrections are only exact at the hypocenter. As the rupture front moves away within a certain distance range, the rays originating from the assumed rupture can be still considered to travel through a similar regional structure as that under the hypocenter. But the heterogeneity of the regional

structure induces the spatial gradient of the travel-time (slowness), which also needs to be corrected by the slowness calibration δs to restore smooth wavefronts (Figure 2.6d). Our study shows that if the rupture length is less than 150 km, a uniform slowness in the entire source region is sufficient to calibrate the travel-time errors. However, when the source region is significantly larger, like the two investigated regions in our study, a uniform slowness calibration becomes less effective, because the rays from subsequent sources far away from the hypocenter travel through a different regional structure (red shaded area) (Figure 2.6e). Figure 9f illustrates that by allowing different slowness terms in each region, the calibration can more effectively correct travel time errors and mitigate spatial biases. We remark that by implementing all the travel-time corrections, the regional SEBP reduces De by $\sim$50%. This indicates that half of De are aleatory uncertainties that are caused by regional structural complexity and can be calibrated with aftershocks, while the residue errors are epistemic uncertainties caused by local velocity heterogeneities that are unique for each aftershock.

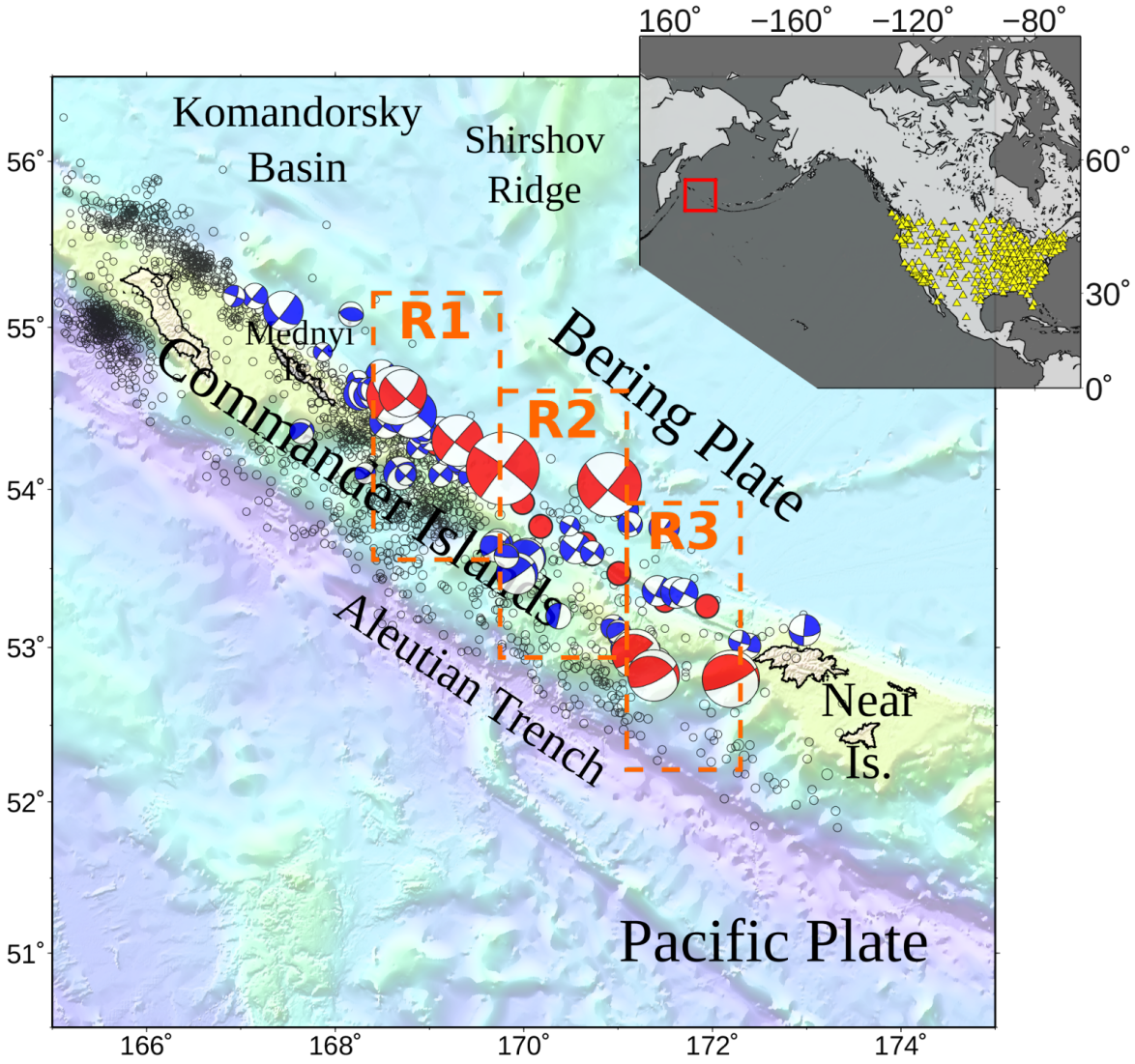

Figure 2.1: **Twenty-two M4-6 earthquakes within the Commander Islander region and the seismic stations used.** The 22 earthquakes (red circles and beach balls) that occurred from 2013 to 2017 are all shallow events (epicenter depth < 35 km based on ISC catalog, http://www.isc.ac.uk). GCMT Focal mechanisms of eight events are shown (Ekström et al., 2012). The top right inset map shows the plotted source region (red box) and the US seismic network (yellow triangles). The three dashed rectangular boxes are the three zoned regions that are selected based on the tectonic characteristics of this region (Lutikov et al., 2019; Newberry et al., 1986; Ruppert et al., 2012.

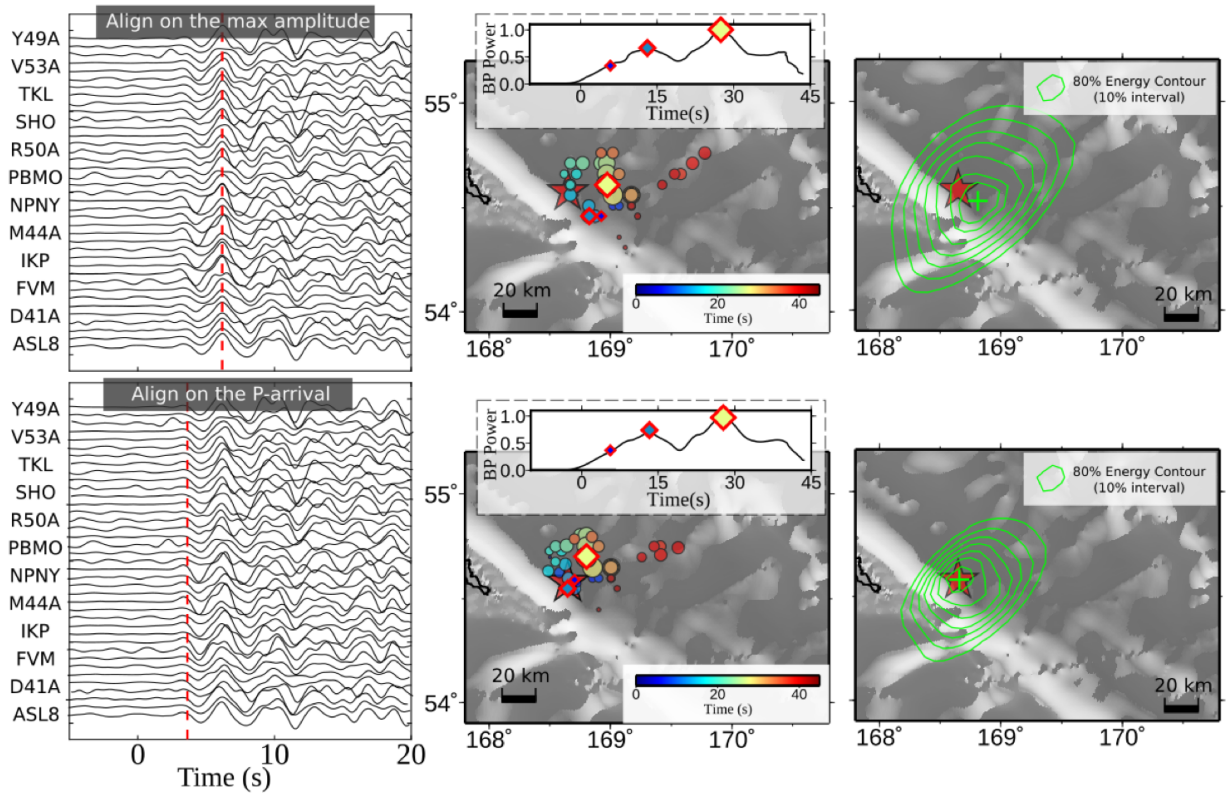

Figure 2.2: **The nontriviality of hypocenter correction (waveform alignment) in Back-projection (BP) location.** (left) Examples of velocity records [0.2 - 1.0 Hz] after hypocenter alignments whose 10-second alignment-window centers the "maximum amplitude" or the "P-arrival". Waveforms are from a Mw 6.3 earthquake that occurred on July 17th, 2017. (middle) High-frequency (circles) radiators of the Mw 6.3 events imaged by MUSIC BP are color coded by time with sizes proportional to BP's beam power. The top inset illustrates BP's beam power as a function of time. Three high-frequency radiators (diamond with red edge) are picked for easy cross-reference. Radiators after 30 sec appear to drift towards NEE, which is likely caused by depth phases of P-waves. (right) Integrated BP result (0.5 - 2 Hz, 80% energy contour) of the first 10 sec. The Back-projection inferred (BPI) location is marked by a green cross.

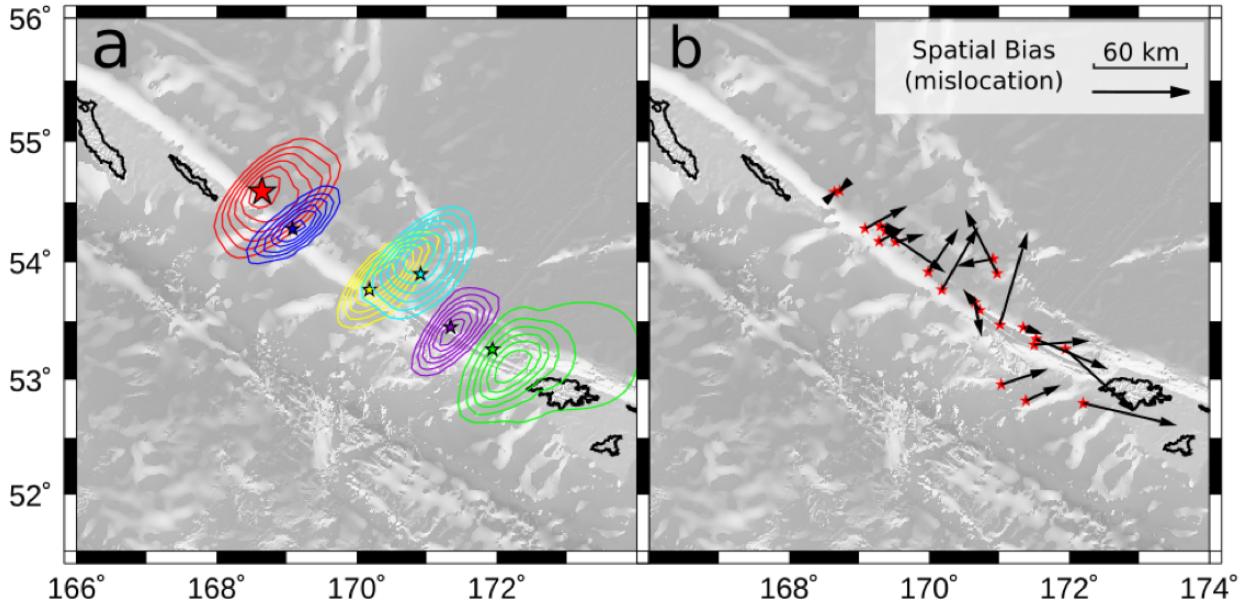

Figure 2.3: **Overview of spatial biases in the Commander Island region: BP results with time corrections from the Mw 6.3 earthquakes as the reference event applied to the other 21 events.** (a) Examples of 80% energy contour of integrated BP images of the first 10 sec. For clarity, only 6 events are shown here. (b) The spatial biases (black vector) of the 21 events, as measured by the distance of the image peak from the epicenter (De), which is defined in the same way as Fan & Shearer (2017)

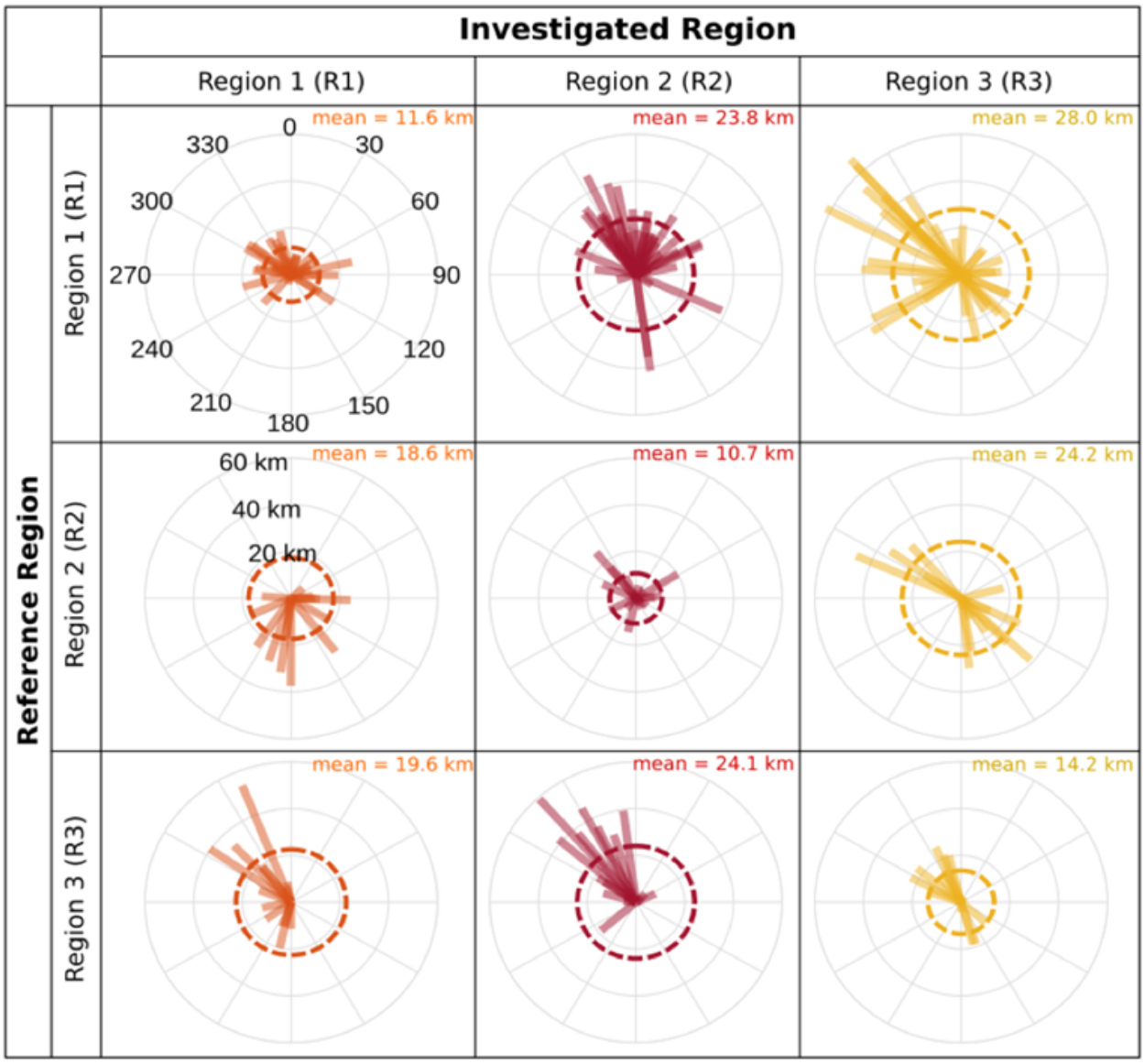

Figure 2.4: **Patterns (directivity and amplitude) of spatial biases in the Commander Island region.** The reference region represents the region where a reference event is located. The hypocenter correction of a reference event is then applied to all the events in another region (i.e. investigated region) to obtain their Back-projection inferred (BPI) locations. *De* (both distance and azimuth) of the BPI locations are plotted as bars in the polar plot. In each plot, the mean values of *De* are marked (thick dashed line).

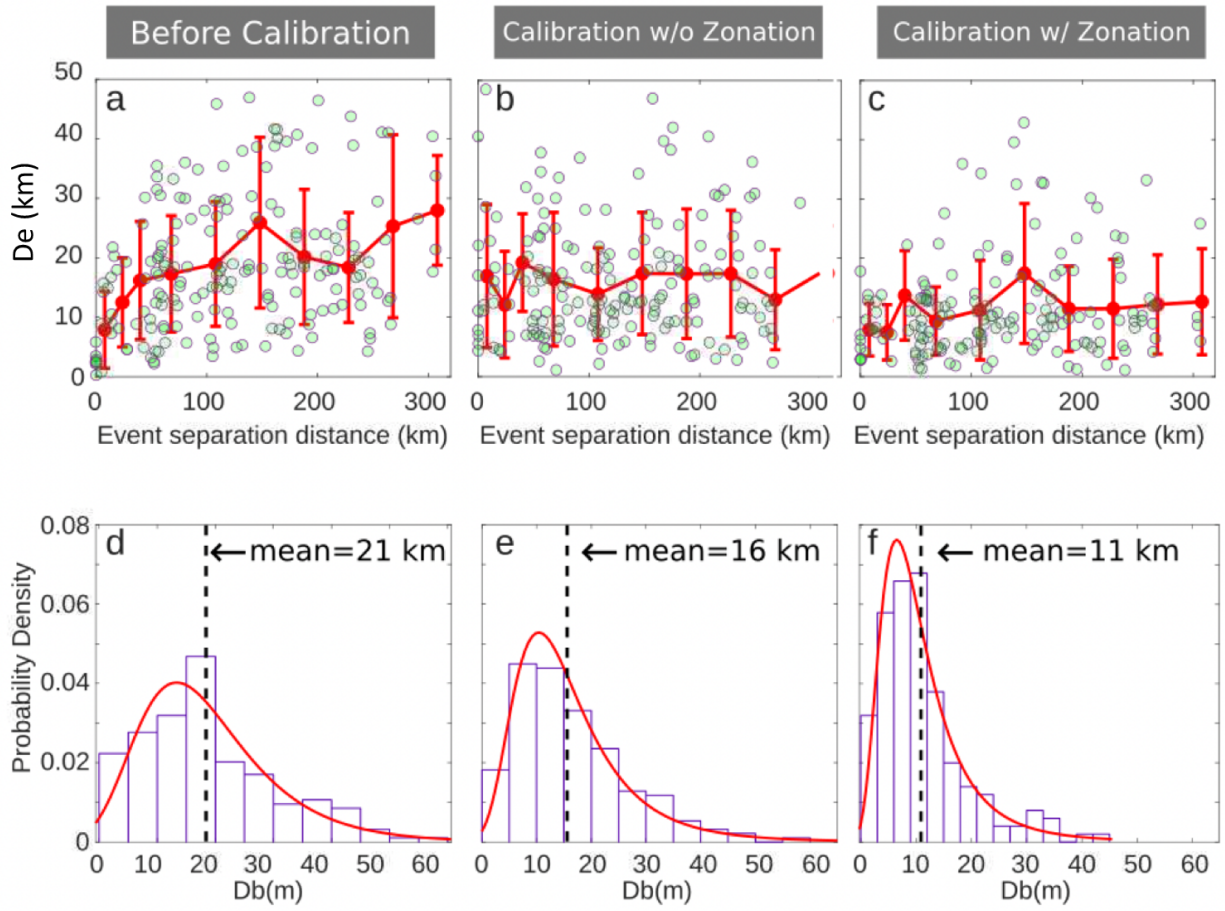

Figure 2.5: **Characteristics of spatial bias before and after slowness calibration.** (a-c) *De* as a function of event separation distance (distances between reference and investigated events). Each data point is one event pair measurement of *De* of the investigated event when applying the hypocenter correction of a reference event. Red error bars are one standard deviation of the measurements. (d-f) Distribution of *De*. The fitted probability density functions (PDF) follow generalized extreme value (GEV) distribution, whose parameters are listed in Table S3.

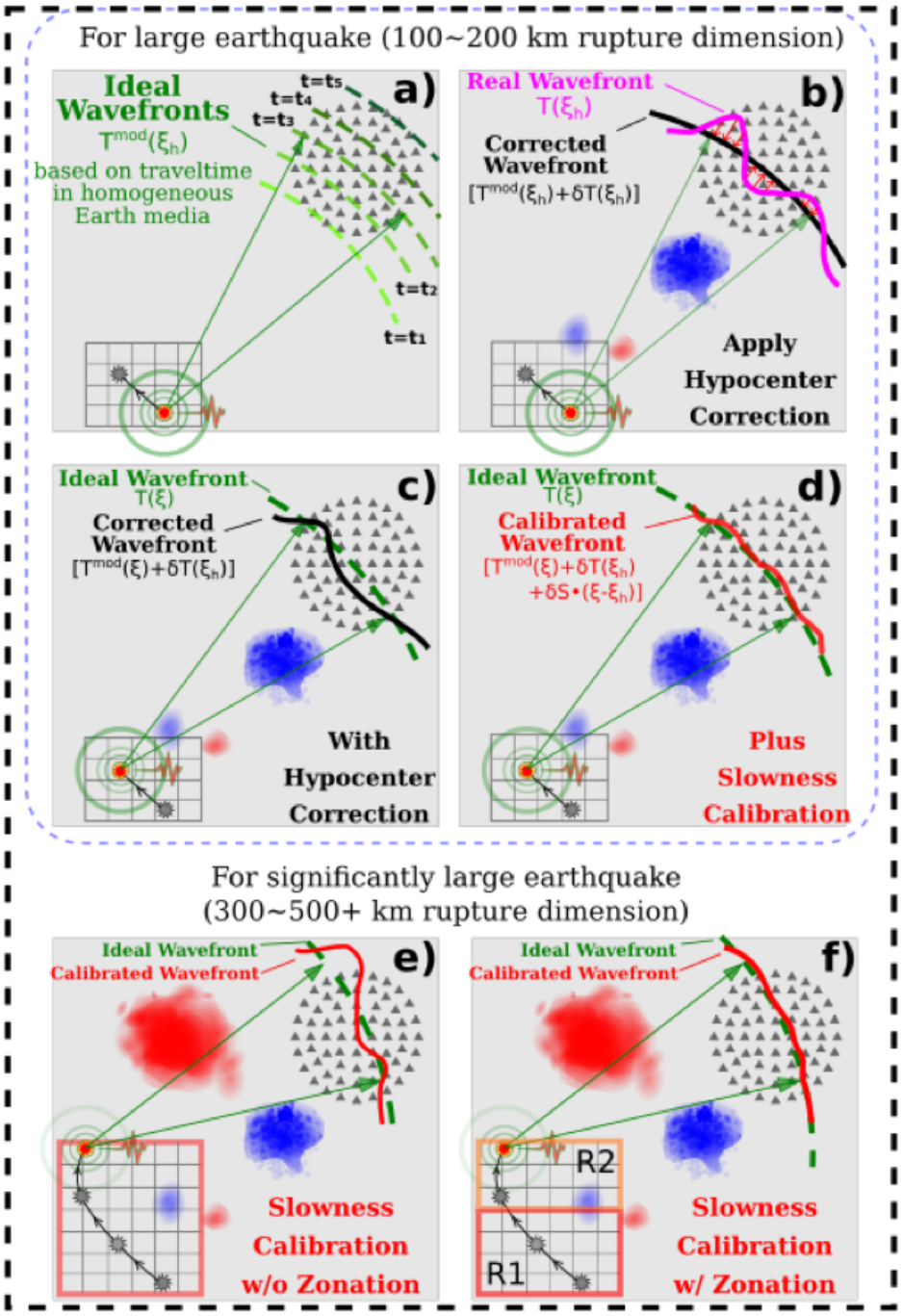
For large earthquake (100~200 km rupture dimension)
Ideal Wavefronts
$T^{mod}(\xi_h)$
based on traveltime in homogeneous Earth media
t=t5
t=t4
t=t3
t=t2
t=t1
a)
Real Wavefront
$T(\xi_h)$
Corrected Wavefront
$[T^{mod}(\xi_h)+\delta T(\xi_h)]$
b)
Apply Hypocenter Correction
Ideal Wavefront
$T(\xi)$
Corrected Wavefront
$[T^{mod}(\xi)+\delta T(\xi_h)]$
c)
With Hypocenter Correction
Ideal Wavefront
$T(\xi)$
Calibrated Wavefront
$[T^{mod}(\xi)+\delta T(\xi_h)$
$+\delta S\cdot(\xi-\xi_h)]$
d)
Plus Slowness Calibration
For significantly large earthquake
(300~500+ km rupture dimension)
Ideal Wavefront
Calibrated Wavefront
e)
Slowness Calibration w/o Zonation
Ideal Wavefront
Calibrated Wavefront
f)
R2
R1
Slowness Calibration w/ Zonation

Figure 2.6: **Cartoon illustration of Back-projection method and slowness calibration.** (a) Geometries of wavefronts (green dashed lines) depicted by the travel time table from a source region to a seismic array. The wavefronts are ideally smooth spherical if the Earth media is homogeneous. (b) The structural heterogeneity of the real Earth perturbs travel times and results in distorted wavefront (wiggly pink line). By cross-correlate aligning P wave arrivals, relative time errors of the ray paths originating from the hypocenter can be well corrected (i.e., hypocenter correction). (c) However, the hypocenter corrections are only exact at the hypocenter, because rays originating from other sources will travel through different 3-D structures, which results in distorted wavefront (wiggly black line) again. (d) The slowness calibration effectively mitigates the waveform distortion as spatial biases in the entire source region are accounted for, which resulted in less distorted wavefronts (red solid line). (e) Such a uniform slowness calibration becomes less effective when the source region is significantly large (e.g., 300+ km), and calibrated wavefronts (red wiggly line) that originate from sources far away from the hypocenter are not effectively corrected. This is likely caused by the fact that rays from sources that are far away travel through different large scale heterogeneities. (f) When applying the regional SEBP, travel time errors in the entire source region can be better calibrated, and result in less distorted wavefronts (red solid line)

CHAPTER 3

Mach Wave Validation of Supershear Ruptures

3.1 Method

Mach waves, a unique signature of supershear ruptures, can be effectively identified in the far-field surface wavefield. For earthquakes rupturing at velocities slower than Rayleigh wave speed, wavefronts from different sub-sources arrive at any far-field receiver at different times. For supershear earthquakes, only at stations located on the Rayleigh Mach cone do waves from different parts of a supershear rupture arrive simultaneously and interfere constructively, resulting in an apparent point-source. As first proposed by Vallée and Dunham, 2012, along the Mach cone, the waveform of a supershear mainshock should be identical to that of a smaller reference event, referred to as an empirical Green's function (EGF) event, with a similar focal mechanism in the vicinity of the mainshock. The Mach wave identification is conducted by evaluating the waveform similarity between a target event and its collocated EGF. The standard cross-correlation CC are often used to estimate the waveform similarity. $CC(U,u) = \sum_{i=1}^{N} U_i u_i / \sqrt{\sum_{i=1}^{N} U_i U_i \sum_{i=1}^{N} u_i u_i}$, where U and u are the discrete time-series of the mainshock and the EGF event, respectively.

To maintain the finite-source effect of the mainshock and the point-source effect of the EGF, the waveforms should be compared at periods shorter than the duration of the mainshock T0 and longer than the duration of the EGF. Considering the travel-time errors due to surface wave dispersion and 3D path effect, we manually identify the EGF Rayleigh-wave arrivals, which are simpler and more straightforward to pick than those of the mainshocks.

For each station, we choose 200 $\sim$ 400 s long cross-correlation windows to include the entire envelope of the EGF wave trains (due to dispersion, the envelope becomes longer at larger hypocenter distances). We assume the same arrival times and use the same windowing for the mainshock Rayleigh waves. Since supershear rupture rarely starts from the beginning of the earthquake, we allow lag times up to the half duration of the mainshock when calculating CC.

The source directivity effect relates the observed high waveform similarities to the locations of the Mach cones. The apparent source duration T_a of the mainshock is equal to the true duration T_0 scaled by the directivity factor (Figure 3.1): $T_a = T_0 \times D(\Phi)$. $D(\Phi) = 1 - \cos(\Phi)V_r/V_{\text{Rayleigh}}$ where Φ is the receiver azimuth relative to the rupture direction, Vr is the rupture speed, and V_{Rayleigh} is the Rayleigh wave speed at the center period T_c of the waveform filter. Given the short duration of the EGF event, the mainshock waveform is similar to that of the EGF if the mainshock also appears as an apparent point source, which requires $T_a \ll T_c$. If $T_c \sim 20$ s and $T_0 \sim 40$ s, the two events are of high similarity when $|D(\Phi)| \ll 0.5$. This condition is met near and on the Mach cone where the $D(\Phi)$ is minimized. For fast sub-Rayleigh ruptures, waveform similarity is maximized in the rupture direction. For supershear ruptures, waveform similarity reaches its maximum on the two Mach cones. The waveform similarity can also be relatively high in between the Mach Cones but still lower than that in the Mach cones if the rupture speed is only moderately faster than the S wave.

The amplitude information can also be used to identify the supershear event, since the amplitude ratio between the Rayleigh Mach wave of the supershear earthquake and that of the EGF event should equal their moment ratio:

$$\frac{\text{std}(U)}{std(u)} = \frac{M_0}{M_{EGF}}$$

where std is the standard deviation of surface waves, and M_0 and M_{EGF} are the moment of the mainshock and EGF event, respectively. However, since most of the supershear earth-

quakes do not propagate at supershear rupture speeds entirely, the moment of a supershear rupture is only a part of M_0. Therefore, the waveform amplitude ratio $\mathrm{std}(U)/\,\mathrm{std}(u)$ tends to be smaller than the moment ratio M_0/M_{EGF}. However, the azimuthal pattern of the amplitude-ratio (AR) can still distinguish sub-Rayleigh and supershear events.

$$AR = \frac{\mathrm{std}(U)/M_0}{\mathrm{std}(u)/M_{EGF}}$$

For sub-Rayleigh ruptures, the distribution is unimodal with the highest amplitude ratio in the rupture direction, while that of supershear rupture is bimodal with high amplitude ratios on each of the Mach cones.

3.2 Mach Wave Synthetic Test

The purpose of the synthetic tests is to examine the effect of the rupture speed on the cross-correlation coefficient of the empirical Green's function (EGF) and mainshock waveform. The synthetic rupture propagation can be simulated as a series of sub-sources, and the waveforms of the synthetic rupture can be modeled as the superposition of EGF (regarded as a point source) waveforms considering the rupture times and locations of different sub-sources. Since the station distribution and azimuthal coverage of the 2016 Romanche earthquake is one of the best among all examined events, we use the waveforms of the EGF event of the 2016 Romanche earthquake to form synthetic waveforms of elongated ruptures with different rupture speeds (Figure 3.2). We set up a 160 km long, westward rupture with 9 point sources with an interval of 30kms evenly distributed along the rupture path. We test eight different rupture speeds: $0.5\mathrm{Vs}, 0.7\mathrm{Vs}, 0.9\mathrm{Vs}, 1.0\mathrm{Vs}, 1.1\mathrm{Vs}, 1.2\mathrm{Vs}, 1.3\mathrm{Vs}$, and 1.5 V, where Vs is the shear wave speed assumed to be 3.5 km/s. We filter the synthetic waveforms and the EGF waveforms with a narrow-band filter, $10 \sim 20$ s. The Rayleigh wave speed of the center frequency (1/15 Hz) is assumed to be 0.9Vs. We then measure the cross-correlation (CC) coefficient between the synthetic waveforms and the EGF waveforms (Figure 3.2 & 3.3). The

waveform comparisons are shown in Figure 3.3 – 3.6.

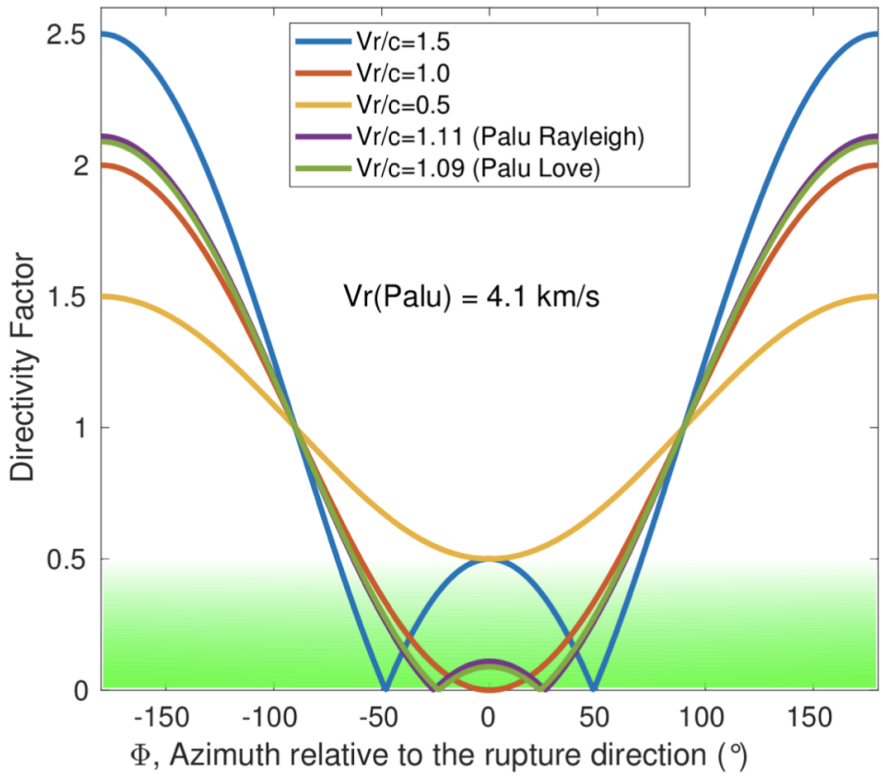

Figure 3.1: Absolute value of the directivity factor $D(\Phi) = 1 - \cos(\Phi)^*\mathrm{Vr/C}$ as a function of azimuth Φ relative to the rupture direction, for different ratios of rupture speed Vr to wave speed c. The bandpass filtered waveforms of a mainshock and a co-located foreshock are similar if the apparent corner frequency of the mainshock, $1/\left(|D|^*T\right)$ where T is the rupture duration, is substantially higher than the dominant frequency $1/T0$ of the filtered waveforms. In our analysis of the Palu earthquake $T \sim 40$ s and $T0 \sim 20$ s, thus the condition for similarity is $|D(\Phi)| << 0.5$. This condition is met at azimuths for which the $|\mathrm{D}(\Phi)|$ curve in this figure falls within the darker green band. For sufficiently fast sub-Rayleigh ruptures (red curve), waveform similarity is expected to be maximal in the direction of rupture. For supershear ruptures (blue, purple and green curves), waveform similarity is maximal on the Mach cones, i.e. at the two azimuths where $D(\Phi) = 0$, but it can be high also in between if the rupture speed is not too fast (purple and green curves, corresponding to the Palu earthquake speed compared to Rayleigh and Love waves, respectively).

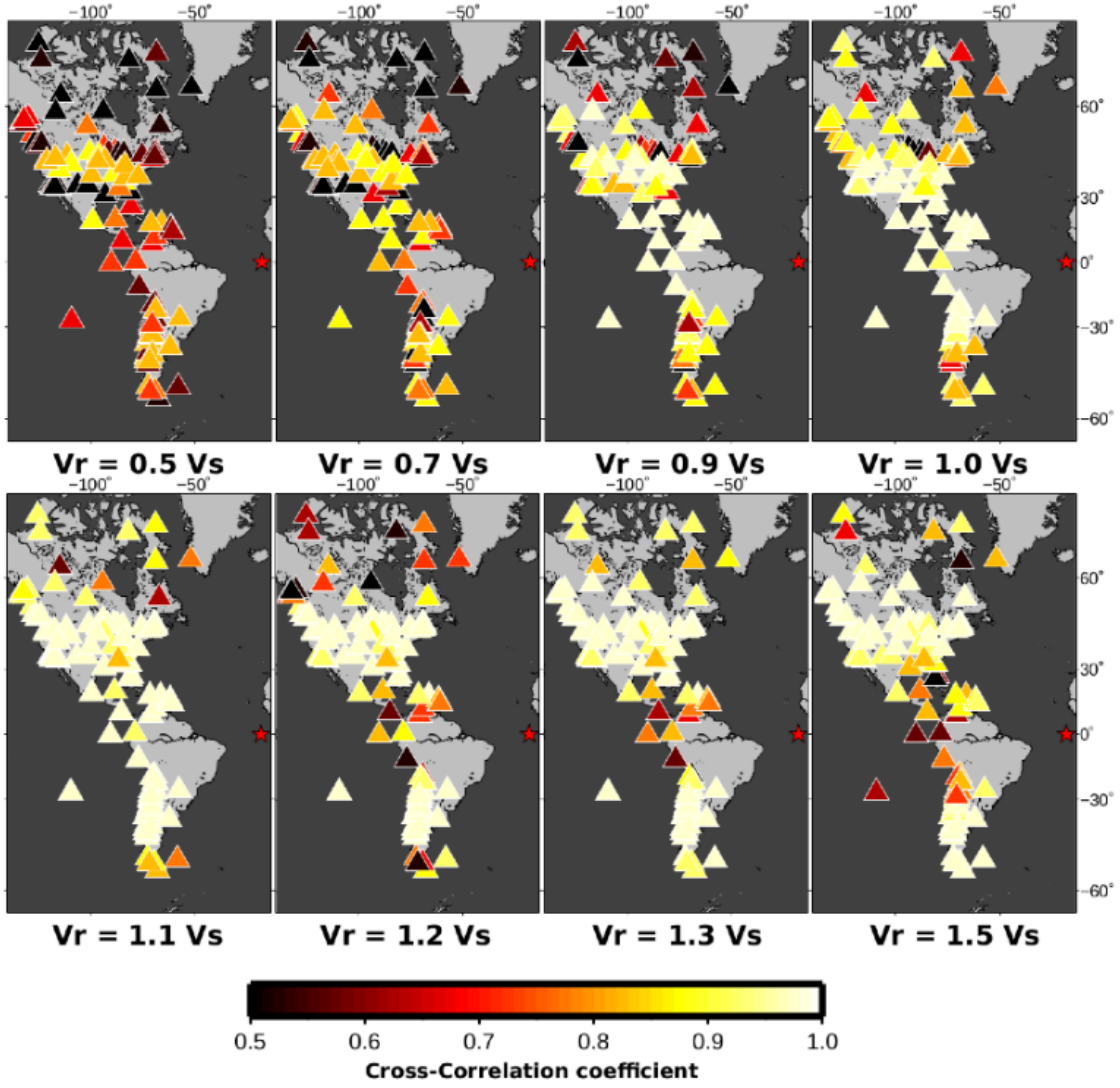

Figure 3.2: Mapview of cross-correlation coefficients (CC) of the synthetic tests. The synthetic test of elongated rupture with different rupture speed is described above. The locations of the broadband stations are indicated by triangles. Their color indicates the correlation coefficients of Rayleigh wave displacement seismograms of the synthetic seismograms of the elongated ruptures and the EGF events. See Figure 3.7 for patterns of CC as functions of azimuth. Figure 3.4 3.6 show examples of the comparison of Rayleigh waveforms between the EGF and synthetic ruptures.

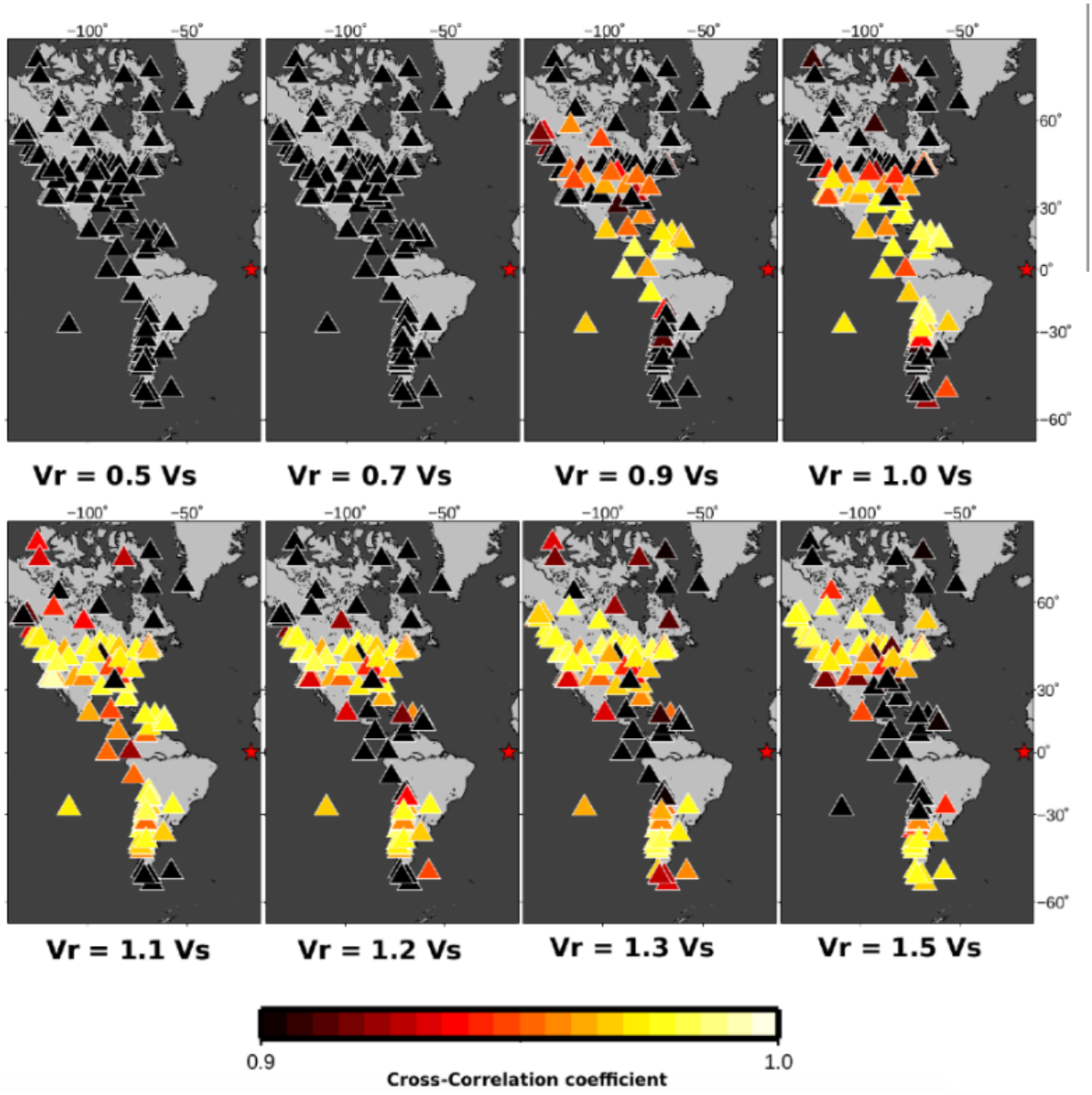

Figure 3.3: Similar to Figure 3.2, the only difference is that the color scale adjusted between 0.9 to 1.0 to highlight the small change of correlation in the frontal direction.

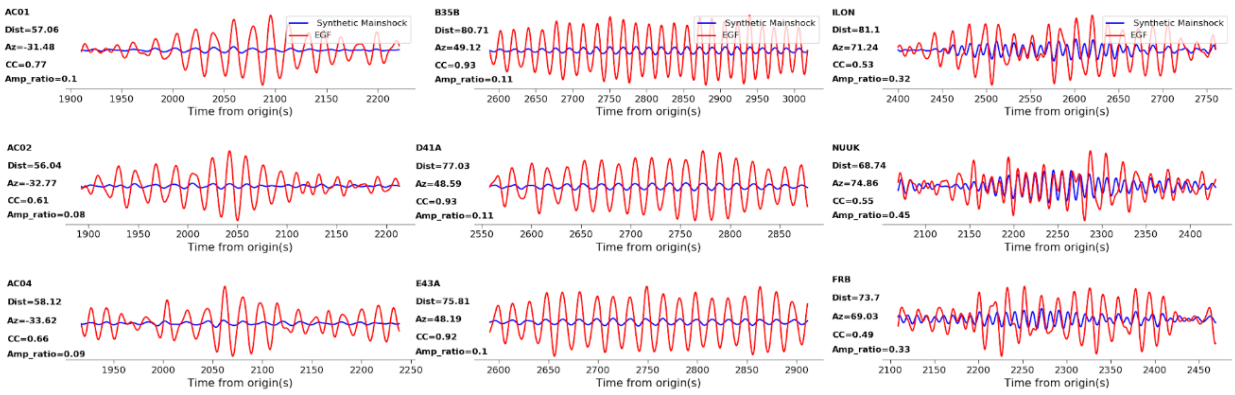

Figure 3.4: Comparison of Rayleigh waveforms between the EGF and the synthetic rupture $\mathbf{Vr = 0.5Vs}$. Rayleigh wave vertical displacement seismograms of synthetic rupture (blue) and the EGF event (red) in the 10-20s period range. Station name, hypocenter distance (Dist), azimuth from the rupture front direction (Az), cross-correlation coefficient (CC), and the amplitude ratio (Amp_ratio) are shown for each station. No Mach wave is identified. Signals of the EGF event are scaled by 1.0 times of M_0/M_{EGF}

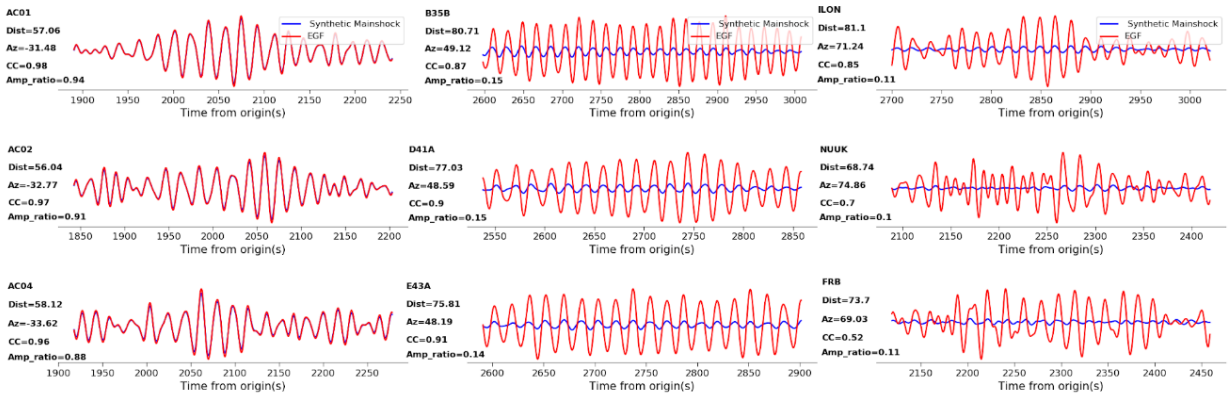

Figure 3.5: Comparison of Rayleigh waveforms between the EGF and the synthetic rupture $\mathbf{Vr = 1.0Vs}$. Rayleigh wave vertical displacement seismograms of synthetic rupture (blue) and the EGF event (red) in the 10-20s period range. Station name, hypocenter distance (Dist), azimuth from the rupture front direction (Az), cross-correlation coefficient (CC), and the amplitude ratio (Amp_ratio) are shown for each station. No Mach wave is identified. Signals of the EGF event are scaled by 1.0 times of M_0/M_{EGF}

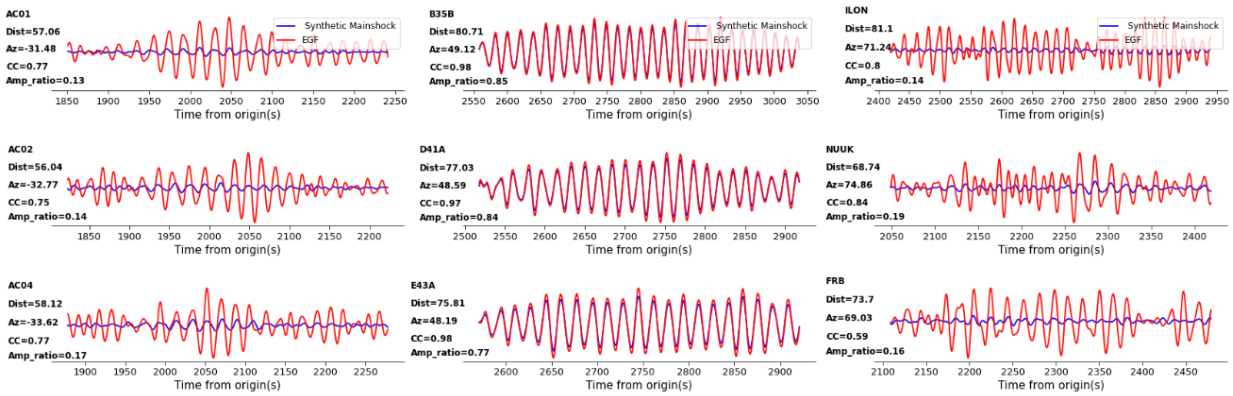

Figure 3.6: Comparison of Rayleigh waveforms between the EGF and the synthetic rupture $\mathbf{Vr = 1.5Vs}$. Rayleigh wave vertical displacement seismograms of synthetic rupture (blue) and the EGF event (red) in the 10-20s period range. Station name, hypocenter distance (Dist), azimuth from the rupture front direction (Az), cross-correlation coefficient (CC), and the amplitude ratio (Amp_ratio are shown for each station. No Mach wave is identified. Signals of the EGF event are scaled by 1.0 times of M_0/M_{EGF}

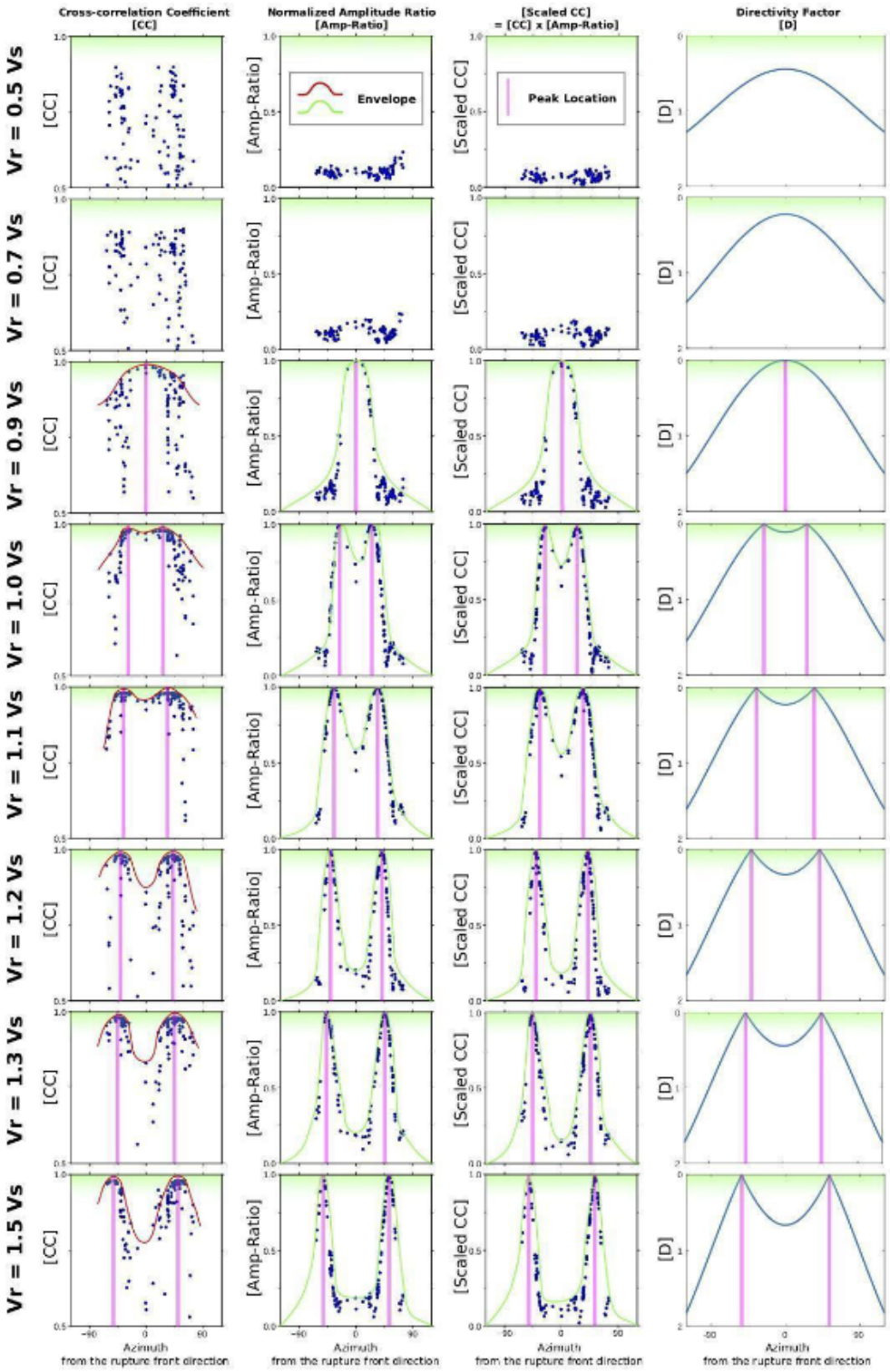
Cross-correlation Coefficient
[CC]
Normalized Amplitude Ratio
[Amp-Ratio]
[Scaled CC]
= [CC] x [Amp-Ratio]
Directivity Factor
[D]
Envelope
Peak Location
Vr = 0.5 Vs
Vr = 0.7 Vs
Vr = 0.9 Vs
Vr = 1.0 Vs
Vr = 1.1 Vs
Vr = 1.2 Vs
Vr = 1.3 Vs
Vr = 1.5 Vs
[CC]
[Amp-Ratio]
[Scaled CC]
[D]
Azimuth
from the rupture front direction

Figure 3.7: (First three columns) Cross-correlation Coefficient (CC), Amplitude Ratio (AR) and the production of CC and AR of the synthetic tests as functions of azimuth from the rupture front direction. The AR is expressed as $AR = [\mathrm{std}(U)/M_0] \,/\, [\mathrm{std}(u)/M_{EGF}]$), where std is the standard deviation of surface waves, and M_0 and M_{EGF} are the moment of the mainshock and EGF event, respectively. (Fourth columns) The directivity factor ($D(\Phi) = 1 - \cos(\Phi)V_r/V_{\mathrm{Rayleigh}}$) as a function of azimuth from the rupture front direction.

CHAPTER 4

Validation of BP Inferred Rupture Speeds Using Synthetic Tests

Abstract

The back projection (BP) has been widely applied to understand the rupture kinematics of large earthquakes. BP's high resolution is linked to its ability of resolving high-frequency (>1 Hz) seismic radiation. At these frequencies, the waveforms are characterized by stochastic scattering of short-wavelength velocity heterogeneities, which leads to strong incoherent coda waves between receiver stations. Previous studies attempted to conduct synthetic tests to understand the resolution and uncertainty of teleseismic BP based on synthetic Green's functions derived from either 1D or smooth 3D velocity models. However, since these GFs does not include incoherent coda waves at high-frequencies, the effect of realistic GF on BP imaging is not well understood. Here, we generated synthetic Green Functions with coda waves using multiple Empirical Green's Functions (EGFs). Traditionally, incoherent signals are thought to degrades the quality of BP imaging. Based on our synthetic tests, we find that the incoherency of EGFs counter-intuitively improves the BP imaging by separating consecutive sub-sources with temporarily decaying coherence and enabling the fluctuation of BP powers in the middle of a smooth rupture with spatially decaying coherence. We further conduct comprehensive synthetic tests of BP considering (1) different scenarios of rupture kinematics (different rupture speeds, segmentations with rupture speeds changes, e.g., supershear transition from subshear speeds to supershear speeds), (2) realistic slip distribution

constrained by various finite source models, and most importantly, (3) realistic waveform complexities, which is one of the main causes of BP artifacts and uncertainties. We found that rupture speeds estimated using Back-projection are systematically underestimated due to the averaging effect of direct and coda waves.

4.1 Introduction

Back-projections (BPs) are routinely applied to investigating the rupture kinematics of large earthquakes (Mw $\sim$ 6.5+) and their seismic hazard assessment. BP locates strong high-frequency (0.1-10 Hz) seismic radiations in the source region using coherent seismic phases recorded by large-aperture teleseismic arrays (see review by Kiser and Ishii, 2017). In contrast to finite source inversions, BP does not require any prior assumptions of fault parameterization or restrictive regularization. BP resolves the fine details of the kinematic rupture processes and geometrical complexities that are often missed by kinematic source inversions, which typically utilize seismic data in relative long-periods (10 - 40 s). For example, BP has been proven to be effective in revealing ruptures with multiple branches (Meng et al. 2012a), instantaneous dynamic triggering of local aftershocks (Fan and Shearer, 2016), frequency-dependent ruptures in subduction-zone megathrust earthquakes (Kiser and Ishii, 2011; Meng et al., 2011; Yao et al., 2013), and high-frequency bursts at the edge of a large-slip area or geometric barriers (Meng et al., 2012; Okuwaki and Yagi, 2018; Uchide et al., 2013; Vallée and Satriano, 2014). In addition, BP provides more direct measurements of rupture sizes and speeds than finite fault inversions as the imagery of high-frequency radiations are often viewed as proxies of the rupture fronts (Meng et al., 2018). The effectiveness of BP imaging was proved by synthetic tests using deterministic synthetic waveform data sets (Okuwaki et al., 2019; Yin and Denolle, 2019). However, these deterministic synthetic tests with simple Green's functions cannot reproduce realistic waveform complexities thus cannot fully extract the relations between BP radiators and rupture kinematics or estimate the uncertainty of

BPs. The above advantage of BP imaging is attributed to its capability of resolving coherent high-frequency seismic signals. Conventionally, high waveform coherence is required for a high-quality BP image and enables the resolvability of rupture processes Rost and Thomas, 2002). The artifacts in BP images are often considered to be generated by the waveform complexities of the Green's functions (GFs), such as the P coda waves, due to scatterings and media heterogeneities. Counterintitutively, the waveform complexities, especially incoherent components in the P-coda waves, also play an important part in the success of BP imaging.

The waveform complexities of the Green's functions come from both the station side (Figure 4.1a) and the source side (Figure 4.1b). The station-side complexities lead to coherence decay of the teleseismic array recordings over time and inter-station separations, and the source-side complexities are attributed to the variations of Green's functions between different segments of the fault zone.

A Green's function without station-side incoherency (Figure 4.1c) shows a slowly decaying stacked power of the P-coda waves (Figure 4.1e), which makes the possible P-arrival of the second sub-source buried in the strong P-coda waves of the first sub-source. A realistic Green's function with station-side incoherency (Figure 4.1d) shows the coherent first P arrival and subsequent incoherent coda waves. The incoherent P-coda cancels with each other thus produce a fast-decaying power (Figure 4.1f). The coherent first arrivals warrant that the corresponding source location is properly imaged by BP, while the fast-decaying power stacked by incoherent coda waves from station-side ensure that an early subsource does not mask or interfere with the subsequent ruptures (see section 4.1).

On the other hand, the source-side incoherency of GFs ensure that the teleseismic waveform recordings for each sub-source is independent even though the source-time functions for each sub-source are the same. For a homogeneous rupture, uniform GFs without source-side incoherency leads to destructive interference between each sub-sources (Figure 4.1e), thus only starting and stopping phases can be imaged by BP. The independency of each sub-source lead to fluctuations to the teleseismic recordings, which breaks up the destructive

interference of the same sub-sources at teleseismic distances, resulting in waveform fluctuations in addition to the starting and stopping phases (Figure 4.1f) and enables the imaging of the details of a homogeneous rupture (see section 4.2).

In this paper, we first demonstrate the coherence pattern of the teleseismic array using selected EGF events from the 2020 Mw 7.7 Cayman Trough earthquakes, one of the largest strike-slip events in the Caribbean Sea region (Figure 4.2a). Then we propose a synthetic method that applies multiple EGFs along the rupture to mimic realistic incoheren signals. We then conduct three synthetic tests of (1) separating two competing sources, (2) homogeneous rupture to demonstrate the importance of incoherency, and address the significance of using incoherent Green's functions in future BP synthetic tests, and (3) inhomogeneous ruptures with various rupture speeds to evaluate the effectiveness of using BP to estimate rupture speeds.

4.2 Coherence and Incoherence Pattern of EGFs

In this section, we conduct two synthetic BP tests using EGFs to demonstrate the significance of incoherency of Green's functions to BPs. The first test is the Back-projection of two competing sub-sources which shows the importance of coherence decay with time. The second test is the back-projection of a homogeneous rupture to show the ability that incoherency enables the imaging of the middle part of the homogeneous rupture.

We first measure the incoherence components of realistic GFs which serves the target of the waveform modeling. The coherence can be measured by the cross-correlation coefficient (CC). To further analyze the coherence pattern of empirical functions of a teleseismic fault zone, we select the source region of the 2020 Mw 7.7 Cayman Trough earthquake recorded by the USArray in Alaska (AK) (Figure 4.2a). The hypocenter is at 78.756°W, 19.419°N (NEIC). Three aftershocks with magnitudes of M 5.4, M 5.1 and M 6.1 along the fault zone are selected as the EGFs (Figure 4.2b-d). The waveforms of the three EGFs recorded by

AK are first aligned by the first P arrival according to the waveform coherence and then stacked (Figure 4.2e). The waveforms are filtered to 0.5-2 Hz. We found that the three EGFs deviates with are different from each other. EGF1 and EGF2 are similar in terms of the initial P arrival and the following depth phase. From the stacked waveform (Figure 4.2e), the P-coda's amplitude peaks at 10 sec after the P arrival with around 50% power of the direct P-wave for all three EGFs. Yet EGF3 with the magnitude of M 6.1 has a relatively complex waveforms before the P-wave arrival.

4.2.1 Two Competing Sources

Here, the synthetic source region of the synthetic test is the same as the fault zone of the 2020 Cayman Trough earthquake (Figure 4.2a) and the seismic array is the USArray in Alaska. We put two competing point sources as the top panels in Figure 4.3. The first source is set at the hypocenter of the Cayman Trough earthquake (78.756°W, 19.419°N, NEIC) and the second 'competing' source is set at 30 km west of the first source with a 10 seconds delay in time, mimicking a westward propagation with a rupture speed of 3 km/s. Since we are especially interested in how the P-codas of the first source and the direct P-wave of the second source compete in a BP imaging, we set the power of the first source to be twice more powerful than the second one. To compare the impacts of different GFs, we adopt the synthetic GFs using the time delay computed by the 1D PREM earth model (1D SGF) and the waveforms of a M5.4 aftershock (Figure. 4.2a) as the empirical Green's function (EGF). We found that its P-coda's amplitude peaks at 10 sec after the P arrival with a 50% power of the direct P-wave.

As a result, the P-coda's peak power of the first source and the P-wave of the second source arrive simultaneously with similar amplitudes, thus competing with each other in BP imaging. Figure 4.3a-c show the BPs of the competing-source tests using the 1D SGFs and EGFs, respectively. 1D SGFs lack coherence decay over time or station separation, while EGFs contain incoherent components thus the EGF BP result resolves the second source with

uncertainties smaller than 7 km (Figure 4.3b). The 1D SGF BP result manifests a larger systematic location bias (more than 15 km) toward the first source (Figure 4.3a) and cannot resolve any radiators at the location of the second source. This experiment demonstrates when two competing signals arrive with comparable powers, coda waves of 1D SGFs can mask or distort later arrivals. Furthermore, it shows that the realistic coherence decays of GFs over time are crucial in ensuring that an early subsource does not mask the subsequent rupture.

4.2.2 Homogeneous Rupture

A uniform-slip model is informational to show how incoherent GFs from the source side influence the BP result. Figure 4.4a is a conceptual demonstration of issues associated with perfectly coherent GFs (on the source side) in a uniform-slip model. Each sinusoidal function represents a wave packet sent from an individual sub-source filtered in a narrow frequency band. The identical signal produced by each sub-source leads to destructive interference except at the beginning and the end, resulting in the deficiency of high-frequency signals in the middle part of the rupture. We conduct BP tests of a uniform-slip rupture using the 1D synthetic GF (Figure 4.4b) and an uniform EGF based on the waveforms of a M5.4 aftershock for all sub-sources (Figure 4.4c). Similar to the conceptual model, BP is only able to recover the starting and stopping phase in the case of uniform EGFs (Figure 4.4c). In reality, the spatial variability of the GFs on the source side breaks the destructive interference and ensures the generation of high-frequency signals in the middle part of the rupture. In addition to GFs incoherency, abrupt fluctuation in fault kinematics (including rupture speed, slip velocity, spatial distribution of slip vector in sub-fault-patches and sub-fault geometry) can also break the destructive interference and produce prominent signals in BP images. However, the incoherent GFs allow that BP resolves rupture front motions even with smoothly varying source kinematics, which explains why BP usually resolves the entirety of the rupture propagation in most previous case studies.

4.2.3 Shadowing and Tailing Artifacts

The incoherent GFs can simulate realistic incoherency thus provide us a unique opportunity for assessing artifacts in BP imaging in a realistic sense. Here, we study two types of frequently observed artifacts in BP imaging: tailing and shaowing artifacts. The shadowing artifacts are usually observed at the abrupt changes in rupture speeds, which generate bursts of high-frequency energy. The abrupt changes in rupture speeds cause local maximas in BP powers (Figure 4.7a) and are followed by complex BP radiators (artifact of apparent stagnation). Such a powerful source can shadow succeeding subsequent sources, observed as a clustered radiators at the point where the rupture speed changes and a gap at the beginning of the other segment of rupture which has the different rupture speed (Figure 4.5b, purple circle). The tailing artifacts are observed as the appearance of BP radiators that continues after the end of a rupture (Figure 4.5b, pink circle), which is also due to the abrupt change of rupture speed at the stopping point of rupture. Remarkably, BP result of real observations contain these two artifacts, as marked in Figure 9. Therefore, the identification of the shadowing and tailing artifacts are essential to evaluate the rupture kinematics: for example, when did rupture end, when did rupture speed change from one regime to another, and what segments may consist of artifacts and thus should not be over-interpreted.

4.3 Estimating Rupture Speed with Back-projection

The high-frequency signals from the rupture can be contaminated by other signals generated by scattering on heterogeneities both near the source region and along ray paths, and thus involve complexities in the Green's functions. Such contaminations may degrade the array recordings' coherence, which may decrease the stability of BP, produce artifacts, and limit the resolution, resolvability, and accuracy.

To evaluate BP's resolution, many synthetic test efforts have been made recently and

shed light on the connections between BP images and fault kinematics. The logic is to set up sequences of synthetic sources, generate synthetic seismograms, and then perform BP to see how the synthetic sources are resolved. However, two critical problems prevent general applications of previous studies of that type: (1) overly coarse discretizations of finite sources by point sources hardly represent slip distributions of realistic earthquakes (Meng et al., 2011; Wang et al., 2016; Yao et al., 2013); and (2) deterministic Green's functions calculated assuming a homogeneous full space (Yin et al., 2019) or a 1D layered Earth model (Koper et al., 2012; Okuwaki et al., 2019) do not involve coda waves induced by heterogeneities and thus fail to reproduce realistic waveform complexities that are a key cause of BP's artifacts.

To understand the robustness of our back-projection results as well as to address the above two problems, we take into account both a uniform slip model and nine finite fault slip models (FFM) of previous large strike-slip earthquakes as the input source models. The selected FFM models are the 1992 Landers (Y. Zeng, 2001), 1999 Izmit (Barka, 1999), 2001 Kunlun (Hayes, 2017), Denali 2002 (Oglesby, 2004), 2009 Caribbean (Hayes, 2017), 2008 Wenchuan (Hayes, 2017), 2017 Komandorski (Lay et al., 2017), 2018 Palu (Socquet et al., 2019), and the 2013 South Sandwich Island earthquake (Hayes, 2017). We also discretize the fault surface in much denser meshes than all previous studies. Such a setup introduces interference between waveforms that originated from different subsources and thus is much more realistic than over-discretized point sources. On the other hand, we apply an interpolation/extrapolation method to generate Green's functions along the synthetic rupture from several empirical Green's function events (EGFs). Such variation of Green's functions along the fault introduces the key to realistic synthetics, the coherence fluctuation of array recordings. This approach makes it possible to generate (1) high frequency (¿ 1 Hz) waves with realistic 3D path effects, (2) coherence fluctuation of array measurements, and (3) all seismic phases that are critical to BP imaging, such as pP, water waves and topography effects.

We apply multiple EGF events and assume each one is only in charge of a certain dis-

tance. Many measurements have been performed to characterize the crust and upper mantle structure as a random media and found the correlation length is about 10-20 km (Capon and Berteussen, 1974). We assume the earthquake source region has similar random features and alternate the Green's function of assumed EGF events at an interval of 20 km along the strike. We assume a logic that is commonly used in empirical Green's function analysis: because all EGF events share similar raypaths and similar focal mechanisms, waveform incoherence between different EGF events are attributed to differences in the near-source path effect (e.g., coda scatterers). One potential problem of M 5 6 events is that although their finite source effects are weak, it still cannot be totally ignored because their source durations are not significantly shorter than the period BP utilizes (1 sec). To mitigate their finite source effect, we normalize all EGFs P wave amplitudes in the frequency band 0.5 2 Hz. As a result, the alternation of EGFs along the strike introduces heterogeneity that mimics the changes of the near-source path effect of Green's functions.

We set our synthetic rupture at the source region of the 2020 Caribbean earthquake (Figure 4.2a). We assume the same hypocenter (19.419°N 78.756°W, NEIC) and same strike angle (255°) of the mainshock, propagating westward along the plate boundary between the North America and Caribbean tectonic plates. The fault surface dimension is set to be rectangular with 300 km length and 15 km depth, which is discretized into elements with size [200 m x 200 m]. Considering the limited signal-noise-ratio (SNR) of small earthquakes in the teleseismic distance, the best candidates are three M 5 6 events (Figure 4.2a). The synthetic waveforms are then calculated based on the discretized representation relation with empirical Green's functions (EGFs):

$$\dot{u}_n(X,t) = \sum_{i=1}^{N} \frac{\mu_i A_i \dot{S}_i\left(t'\right)}{M_0^{e_i}} * \dot{e}_{i_n}\left(\xi, t'; X, t\right)$$

Where $\dot{u}_n$ is the ground velocity in the direction $\hat{x}_n$, at location X and time $t.\mu_i, A_i$, and $\dot{S}_i\left(t'\right)$ are the shear modulus (3GPa everywhere), area, and the desired slip-rate function of the subfault element i, respectively. $M_0^{e_i}$ is the seismic moment of the EGF assigned to

the subfault element i. $\dot{e}_{i_n}$ is the ground velocity of the EGF, which is time-shifted based on the predicted travel time from the location of element i to the receiver location X, such that the origin time of each subfault element is the arrival of the rupture front (i.e., rupture time). * is the convolution operator. The summation in the right hand side is over the entire fault surface A such that $\sum A_i = A$. We use the Yoffe analytic function (Tinti, 2005; Yoffe, 1951) as the slip-rate function, an alternative to Kostrov's crack solution (i.e., a square root singularity function; Kostrov, 1964). The Yoffe function is consistent with the self-similar solution of the elastodynamic equation and with spontaneous dynamic models governed by slip weakening (Nielsen and Madariaga, 2003). It also incorporates the cohesive zone near the rupture front with the traction drop, and it correlates the local healing process with rise-times, consistent with laboratory experiments on fault friction (Ohnaka and Yamashita, 1989). In each synthetic source model, rise times are set proportionally to slip (Melgar and Hayes, 2017).

We performed synthetic tests of different scenarios of rupture kinematics: (1) a uniform slip distribution with constant rupture speeds (2, 3, 4, 5, and 6 km/s), (2) a uniform slip distribution with segmentations of different rupture speeds (e.g., supershear transition), and (3) realistic slip distributions with constant rupture speed.

Results of the synthetic BP tests provide invaluable insights to understand BP imaging. Figure 4.5 to 4.11 and their captions provide step by step illustrations and explanations of the results from detailed showcases to statistical analysis in general.

First, we identified two essential artifacts of BP: the shadowing artifact and the tailing artifact. Figure 4.7 and Figure 4.9 showcase that a BP radiator with significant power is followed by a group of stagnant or back-propagating radiators, even though the actual (input) rupture is still moving forward. The shadowing artifact is such that a powerful source hampers imaging of the succeeding sources. Figure 4.9 displays that a group of radiators is imaged by BP even after the actual (input) rupture ends. These artificial radiators either remain in the vicinity of the rupture end or apparently propagate backward. The tailing

artifact is one that induces an apparent long tail of radiation in time. To understand the physical causes of these two artifacts, we measured the coherence function of the array recordings of the three EGF events. Figure S18 shows that the coherence function decays in time yet takes about 5 to 8 seconds to drop to a low level (CC¡0.5), possibly due to the existence of depth phases and near-source scatters. Note that BP utilizes coherent signals and captures the point in the source region with the highest coherence. Therefore, the tailing artifact is due to the fact that the coherence function of the source takes some time to drop to values that are too low to produce a significant image. The shadowing artifact, on the other hand, involves the competition between different sources. For instance, when the rupture triggers a powerful high-frequency source (say source A), if the coherence and power of A are still dominant when the next source (say source B) is activated, then BP will artificially image the location of A at this time, leading to an apparent source stagnation. When the rupture moves forward and source C fails, if array recordings' coherence and power are no longer dominated by A but by C, then C will be imaged.

Remarkably, most of our BP results of real observations contain these two artifacts. Therefore, the identification of the shadowing and tailing artifacts are essential to evaluate the rupture kinematics: for example, when did rupture end, when did rupture speed change from one regime to another, and what segments may consist of artifacts and thus should not be over-interpreted.

In terms of quantitatively guiding the interpretation of BP results, we found that for elongated ruptures, least-squares linear regression between the timing and the along-strike distance of the leading high-frequency radiators (proxies of the rupture front) is always a conservative yet robust estimate of rupture speed. We found that due to BP's artifacts, rupture speeds are always underestimated (Figure 4.11). The faster the true rupture speed, the more significant the artifact, and the greater the underestimation. Moreover, we found that abrupt changes in rupture speeds (e.g., supershear transitions) and abrupt changes in slip distribution along the fault that correlate with peak values in spatial gradients of slip

can trigger powerful shadowing artifacts in BP (Figure 4.7 and 4.9). The fitting for a fast segment after the supershear transition should be performed after the peak value in BP power (Figure 4.8). Moreover, we statistically analyzed the relation between the estimated rupture speed and the input rupture speed, taking into account all tested cases, and determined an empirical expression of the 'true rupture speed' as a function of the 'estimated rupture speed' with uncertainties (see Figure 4.11).

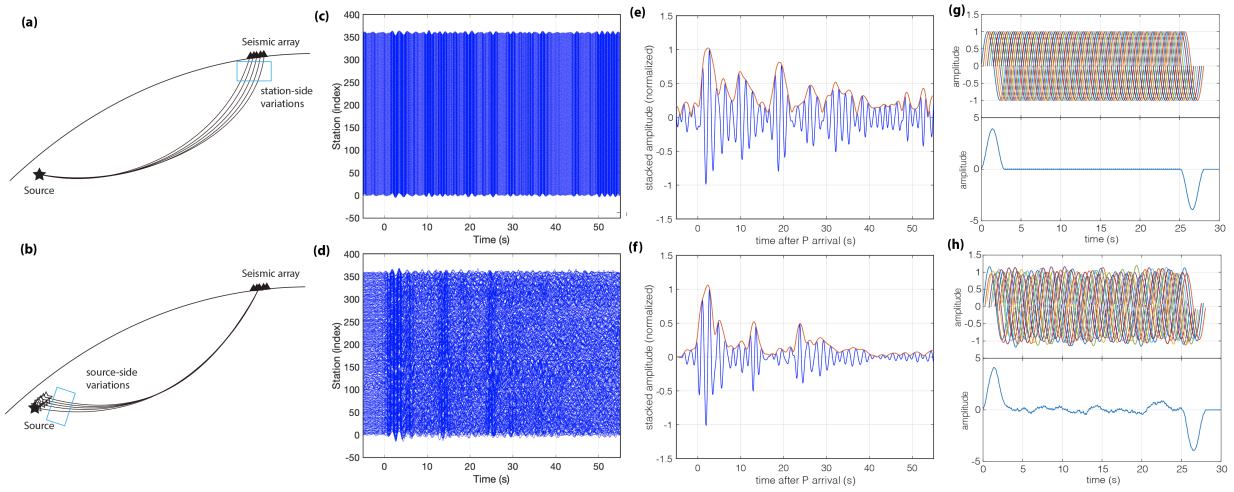

Figure 4.1: **Conceptual figure of the source of incoherency of the Green's functions.** (a) Conceptual figure showing the station-side path variations and scatterings; (b) Conceptual figure showing the source-side path variations and scatterings. (c) Example of a coherent Green's function; (d) Example of a realistic Green's function with incoherent components; (e) stacked power of the coherent Green's function; (f) stacked power of the realistic Green's function with incoherent components. (c-f): Examples taken from the US-Array (Alaska) recordings of the 2020 Cayman Trough earthquake in the Caribbean Sea Plate (see figure 3a). (g) Conceptual figure of the coherent Green's function of each sub--source and the teleseismic recording of a homogeneous rupture. (h) Conceptual figure of the Green's function with source-side incoherency and the teleseismic recording of a homogeneous rupture.

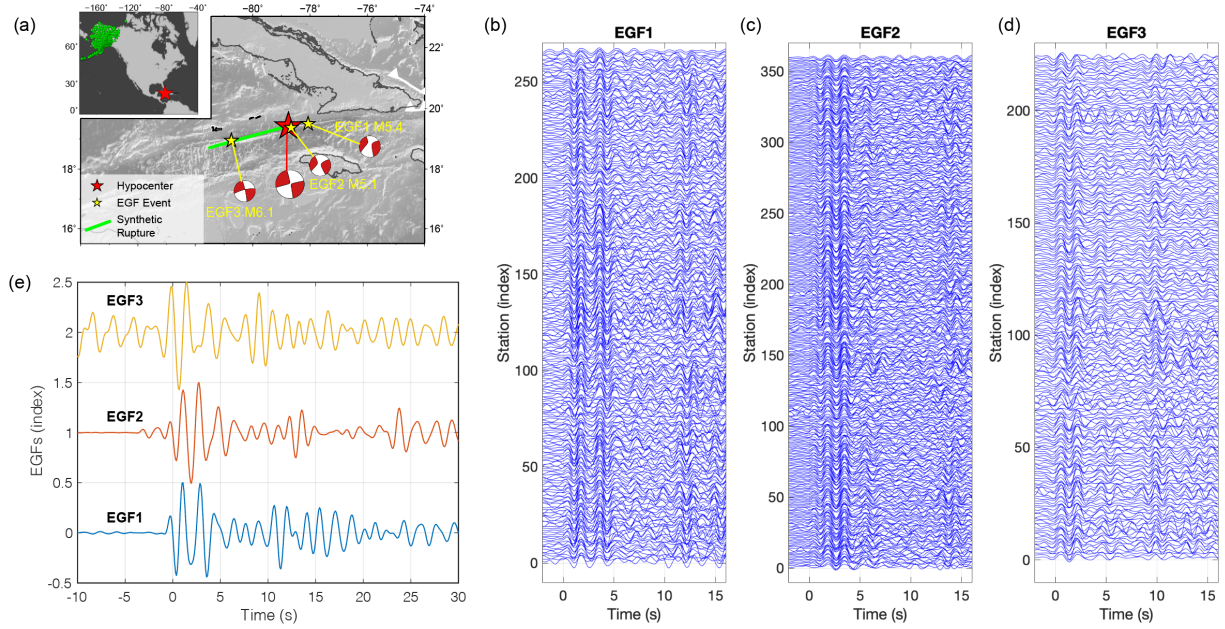

Figure 4.2: **Three EGFs in the Cayman Trough fault zone.** (a) Tectonic settings. Outer panel shows the Cayman Trough fault plane (green line), mainshock (red star), and three aftershocks (yellow stars) with moment tensor solutions from global centroid moment tensor (gCMT) catalog. The fault plane is assumed to along the strike direction of the mainshock. Inner panel shows the relatively location of the fault zone (red star) and the USArray in Alaska (green triangles). (b-d) Aligned waveforms of the three EGFs. (e) Stacked waveform (power) of the aligned waveforms of the three EGFs (normalized according to the maximum amplitude of each stacked EGF).

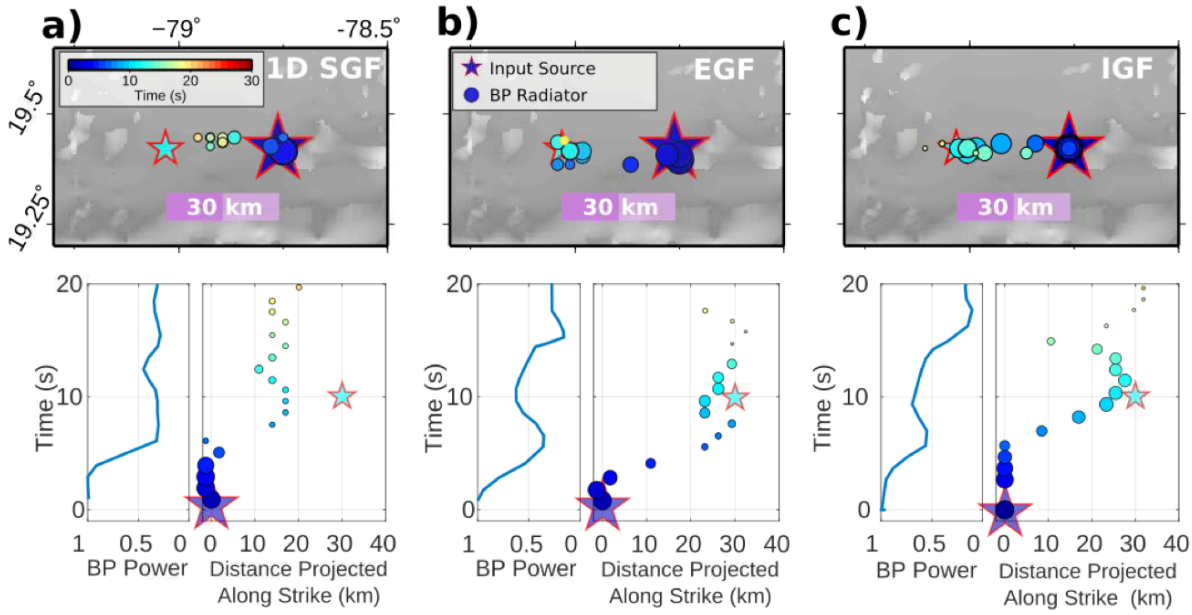

Figure 4.3: **Experiment of two competing sources.** (a) and (b) are BP results of the two competing sources when 1D synthetic GF (1D SGF) and Empirical GF (EGF) are applied, respectively. Stars with red edges are the two input sources, and circles are the location of peak source radiation identified by BP. All symbols are color coded by time and scaled by relative powers.

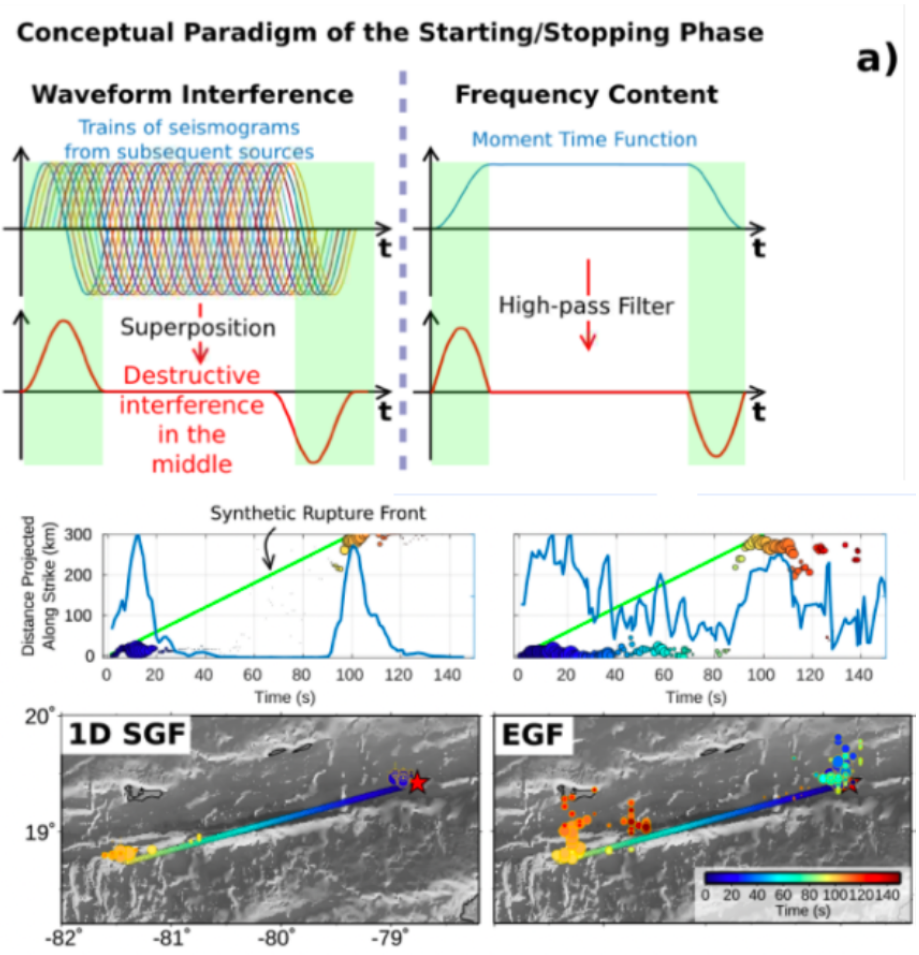

Figure 4.4: **Homogeneous rupture experiment.** (a) Conceptual paradigms of the physical origins of starting/stopping phases. We present two different perspectives: (left) seismograms originated from different subsequent sources result constructively interfere in the beginning and the end but destructively interfere in the middle; (right) a high-pass filter applied over the moment-time function shows that high-frequency signals are generated by variations of energy release, not the absolute moment. (b) BP images and powers for synthetic GFs using 1D seismic model (1D SGF), (c) uniform empirical Green's function (EGF). For the synthetic test, the fault plane is set to be 300 km long and 15 km wide with a uniform slip of 5 m. The rupture is set to propagate unilaterally westward at the speed of 5 km/s in the source region of the Cayman Trough earthquake.

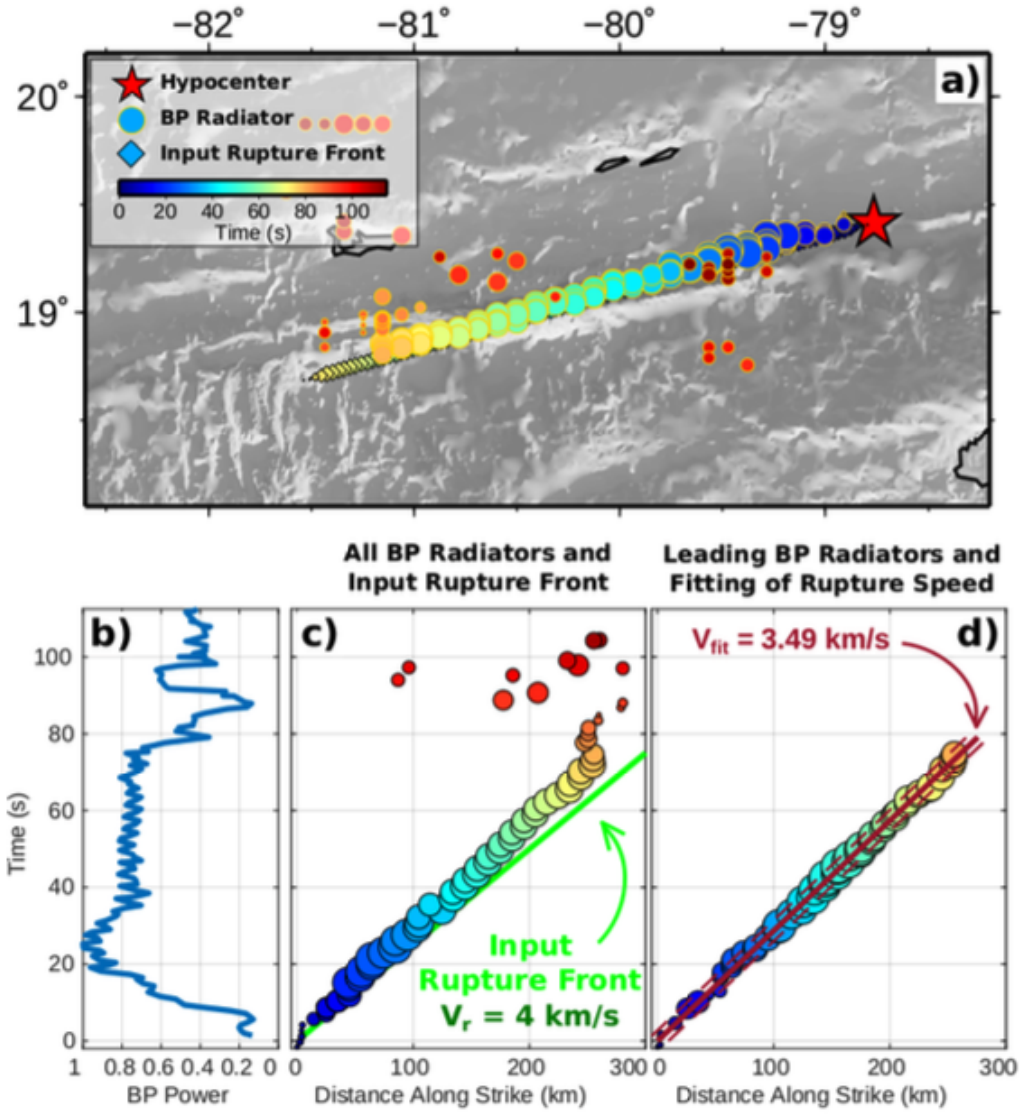
−82°
−81°
−80°
−79°
20°
19°
a)
Hypocenter
BP Radiator
Input Rupture Front
0 20 40 60 80 100
Time (s)
All BP Radiators and
Input Rupture Front
Leading BP Radiators and
Fitting of Rupture Speed
b)
c)
d)
V_{fit} = 3.49 km/s
Time (s)
BP Power
Distance Along Strike (km)
Distance Along Strike (km)
Input
Rupture Front
V_r = 4 km/s

Figure 4.5: **Synthetic BP of uniform rupture with constant rupture speed.** (a) The spatial-temporal evolution of BP (circles) plotted over the input rupture front (diamonds). BP radiators are color-coded by time, and the symbol size represents the normalized power. Synthetic Green's functions are generated assuming a correlation length of source-side heterogeneity of 20 km. Note that the input rupture front (diamonds) is plotted with a much longer interval than the actual discretization for better visual clarity. (b) BP power as a function of time. (c) Along-strike location and timing of BP radiators. Time is relative to the origin time. Location is the horizontal position relative to the hypocentre, projected along the strike direction. The green line indicates the speed of the input rupture front. The tailing artifact, the appearance of BP radiators that continues after the end of a rupture, is highlighted by a pink circle. (d) Least-squares linear regression between the timing and the along-strike distance of the leading BP radiators, defined as the furthest BP radiator at any given time. The dashed lines represent the 95% confidence interval (CI) of the fitting. This case illustrates that fitting a rupture speed with only the leading BP radiators can slightly underestimate the true (input) rupture speed.

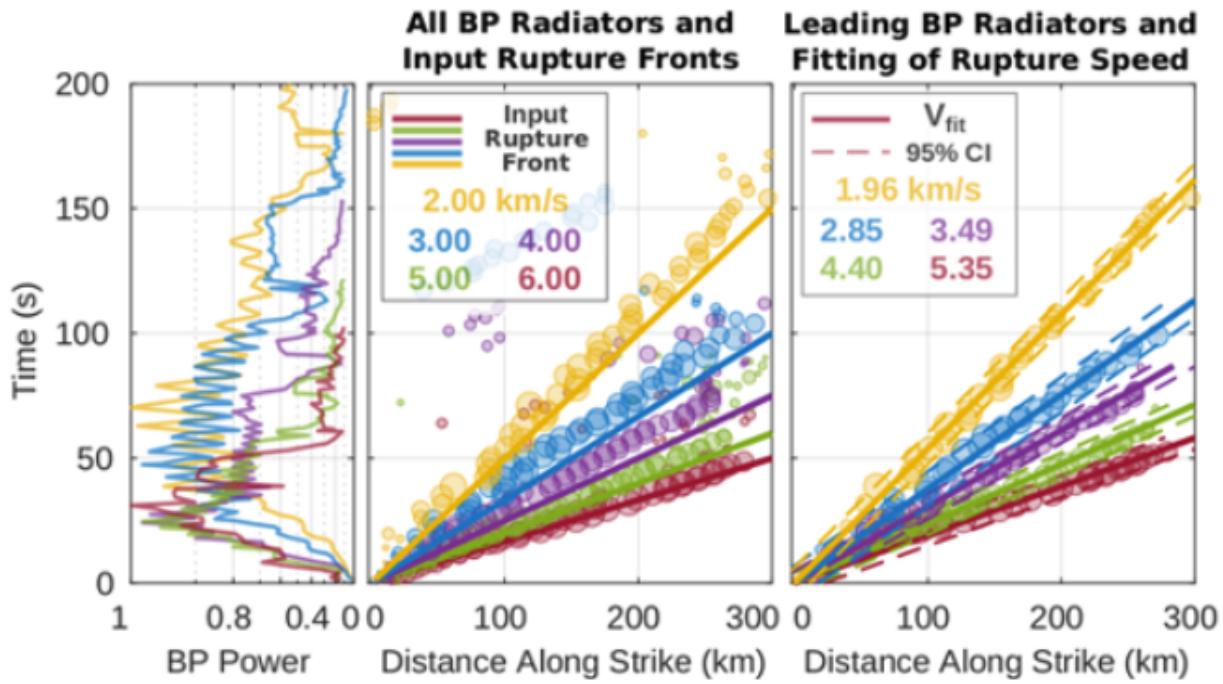

Figure 4.6: **Synthetic BPs of uniform rupture with different rupture speeds.** (Left) BP power as a function of time for different input rupture speeds. (Middle) Along-strike location and timing of BP radiators. Time is relative to the origin time. Location is the horizontal position relative to the hypocentre, projected along the strike direction. The straight lines indicate the speeds of the input rupture fronts (see the inset legend). (Right) Least-squares linear regressions between the timings and the along-strike distances of the leading BP radiators, defined as the furthest BP radiator at any given time. The fitted rupture speeds are shown in the inset legend. The dashed lines represent the 95% confidence interval (CI) of the fittings. This group of cases illustrate that fitting rupture speeds with only leading BP radiators is a conservative yet robust estimate. The faster a rupture speed, the greater the underestimate.

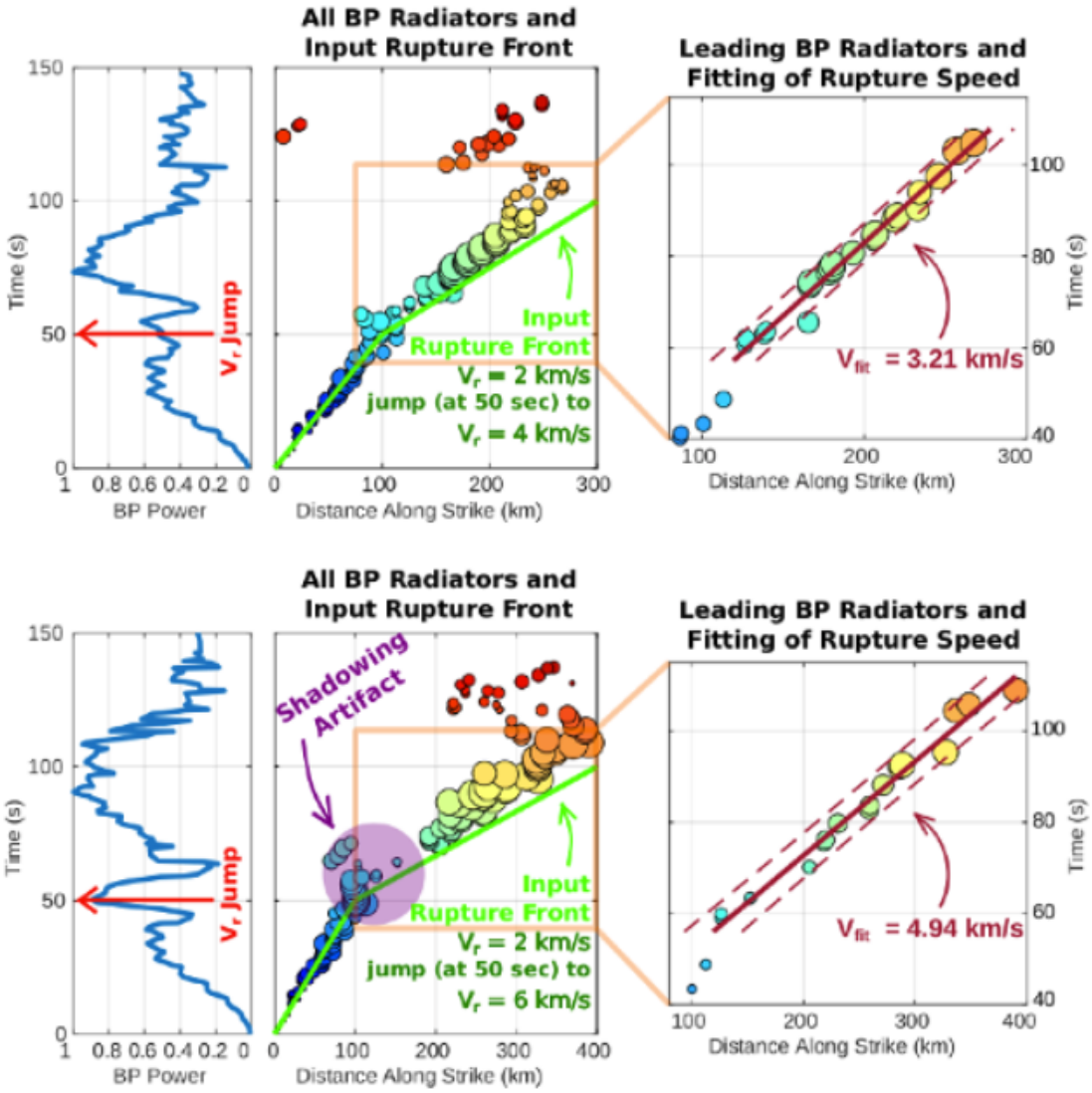
All BP Radiators and
Input Rupture Front
Leading BP Radiators and
Fitting of Rupture Speed
Time (s)
BP Power
Distance Along Strike (km)
V_r Jump
Input
Rupture Front
V_r = 2 km/s
jump (at 50 sec) to
V_r = 4 km/s
V_fit = 3.21 km/s
All BP Radiators and
Input Rupture Front
Leading BP Radiators and
Fitting of Rupture Speed
Shadowing
Artifact
Input
Rupture Front
V_r = 2 km/s
jump (at 50 sec) to
V_r = 6 km/s
V_fit = 4.94 km/s

Figure 4.7: **Synthetic BPs of uniform rupture with abrupt changes in rupture speeds.** (top) The rupture propagates with Vr = 2 km/s for the first 50 sec then accelerates to Vr = 4 km/s for another 50 sec. (bottom) The rupture propagates with Vr = 2 km/s for the first 50 sec then accelerates to Vr = 6 km/s for another 50 sec. The left and middle panels are the same as Figure S11 and S12, while the right panels are the least-squares linear regressions after the velocity change between the timings and the along-strike distances of the leading BP radiators, defined as the furthest BP radiator at any given time. These two cases again show that fitting rupture speeds with the leading BP radiators is a robust and conservative estimate. Moreover, the abrupt changes in rupture speeds cause local maximas in BP powers and are followed by complex BP radiators (artifact of apparent stagnation). This is due to the fact that abrupt changes in rupture speeds generate bursts of high-frequency energy. Such a powerful source can shadow succeeding subsequent sources, and thus this scenario is named "shadowing artifact", as highlighted by a purple circle. The comparison of these two cases demonstrate that greater changes in rupture speed result in more significant BP artifacts.

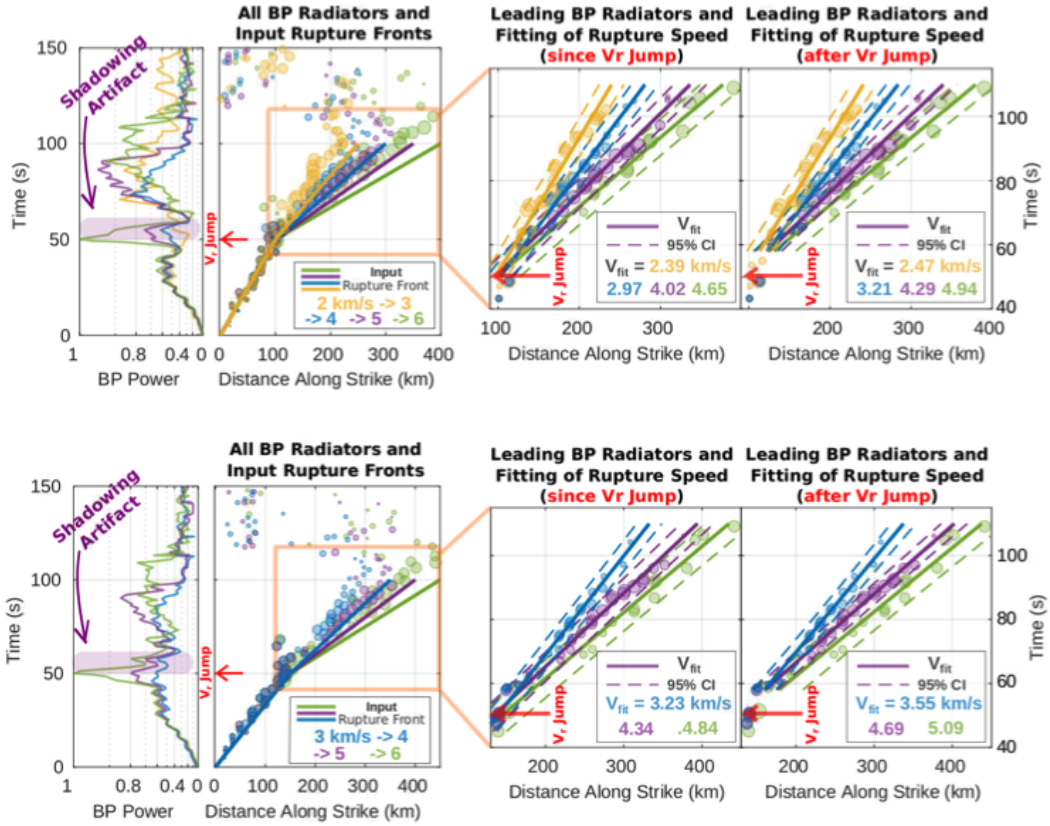

Figure 4.8: **Synthetic BPs of uniform rupture with abrupt changes in rupture speeds.** The left, middle, and right panels are similar to Figure S12. Two groups of cases with different initial rupture speeds, 2 km/s (top) and 3 km/s (bottom), are shown. Differences in BP powers (left) demonstrate that the larger the velocity contrast between two neighboring segments, the stronger the high-frequency burst, and thus more significant the shadowing artifacts. The right panels display that fitting of rupture speeds both since or after the velocity change lead to underestimations, but the fittings since the velocity change result in greater underestimation, due to the shadowing artifact.

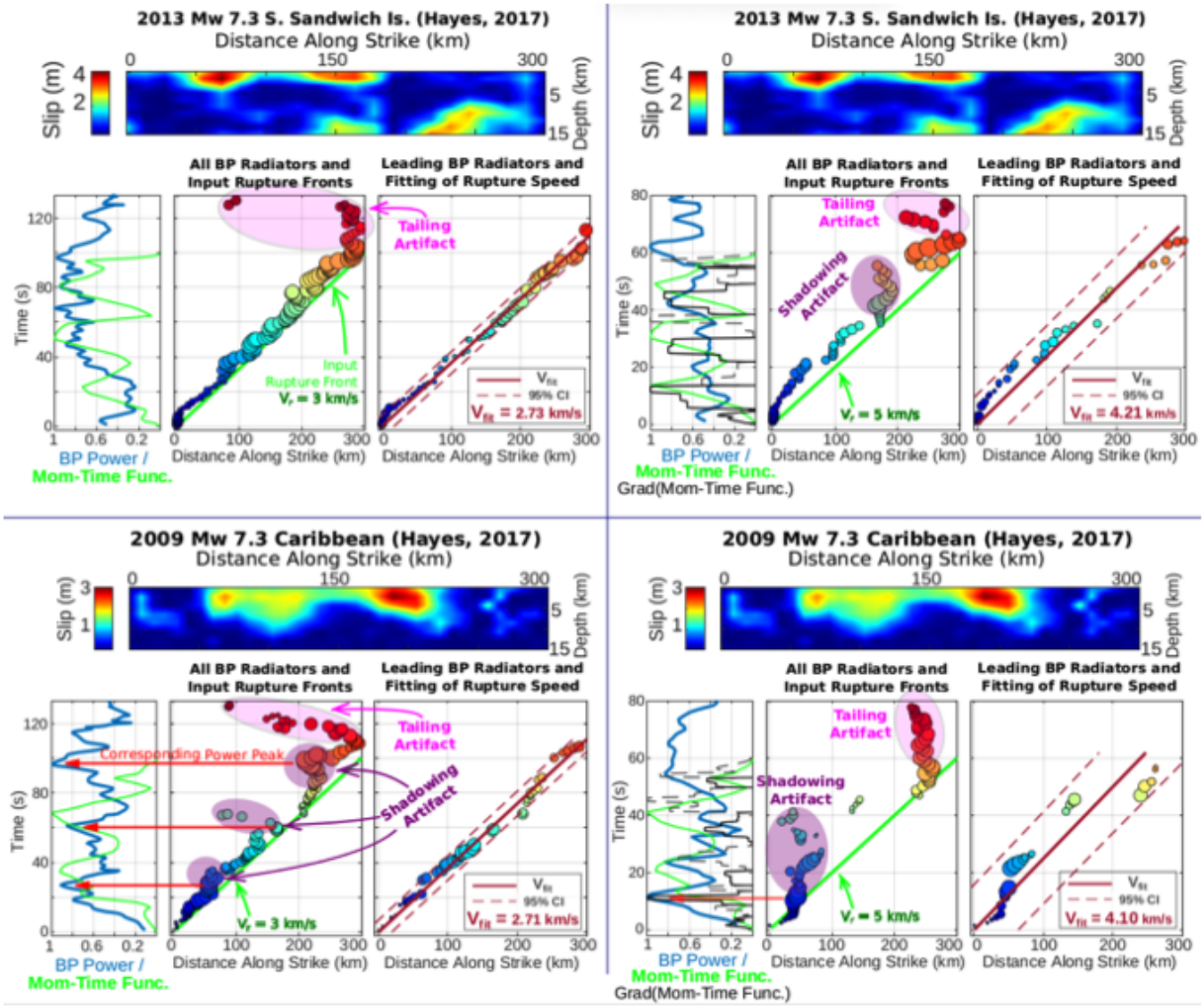
2013 Mw 7.3 S. Sandwich Is. (Hayes, 2017)
Distance Along Strike (km)
Slip (m)
Depth (km)
All BP Radiators and Input Rupture Fronts
Leading BP Radiators and Fitting of Rupture Speed
Tailing Artifact
Shadowing Artifact
Input Rupture Front
V_r = 3 km/s
V_r = 5 km/s
V_{fit} = 2.73 km/s
V_{fit} = 4.21 km/s
95% CI
Time (s)
BP Power / Mom-Time Func.
Grad(Mom-Time Func.)
2009 Mw 7.3 Caribbean (Hayes, 2017)
Corresponding Power Peak
V_{fit} = 2.71 km/s
V_{fit} = 4.10 km/s

Figure 4.9: **Synthetic BPs of rupture with realistic slip distribution and constant rupture speeds.** The figure setup is the same as Figure S11 but with the assumed slip model displayed on the top of each case. Four cases are shown: ruptures with the slip model of the 2013 Mw 7.3 South Sandwich Island earthquake (Hayes, 2017) and constant rupture speed of 3km/s (top left) and 5 km/s (top right); ruptures with the slip model of the 2009 Mw 7.3 Caribbean earthquake (Hayes, 2017) and constant rupture speed of 3km/s (bottom left) and 5 km/s (bottom right). Both the shadowing artifact and the tailing artifact are highlighted. The tailing artifact describes the appearance of BP radiators that continue after the end of a rupture, which either remains in the vicinity of the rupture end or apparently propagates backward. The comparison between the left two cases or the comparison between the right two cases shows that when the rupture speeds are the same, different slip distribution can lead to different levels of BP artifacts. Comparing the top two cases or the bottom two cases shows that a fast rupture speed results in more significant BP artifacts when the slip distribution is held. To analyze the shadowing artifact, we plot the moment-time function (green curve) and the gradient of the moment-time function (black curve; dashed lines are the absolute value of the negative gradients of the moment-time function). We found that the slip model of the 2009 Caribbean earthquake has a more considerable variance in the gradient of the moment-time function, and thus its BP artifacts are more significant. We found that the strongest shadowing artifact in the bottom right panel is attributed to the most substantial peak in the gradient of its moment-time function. In addition, fitting the rupture speed with leading BP radiators is still the most conservative and robust approach.

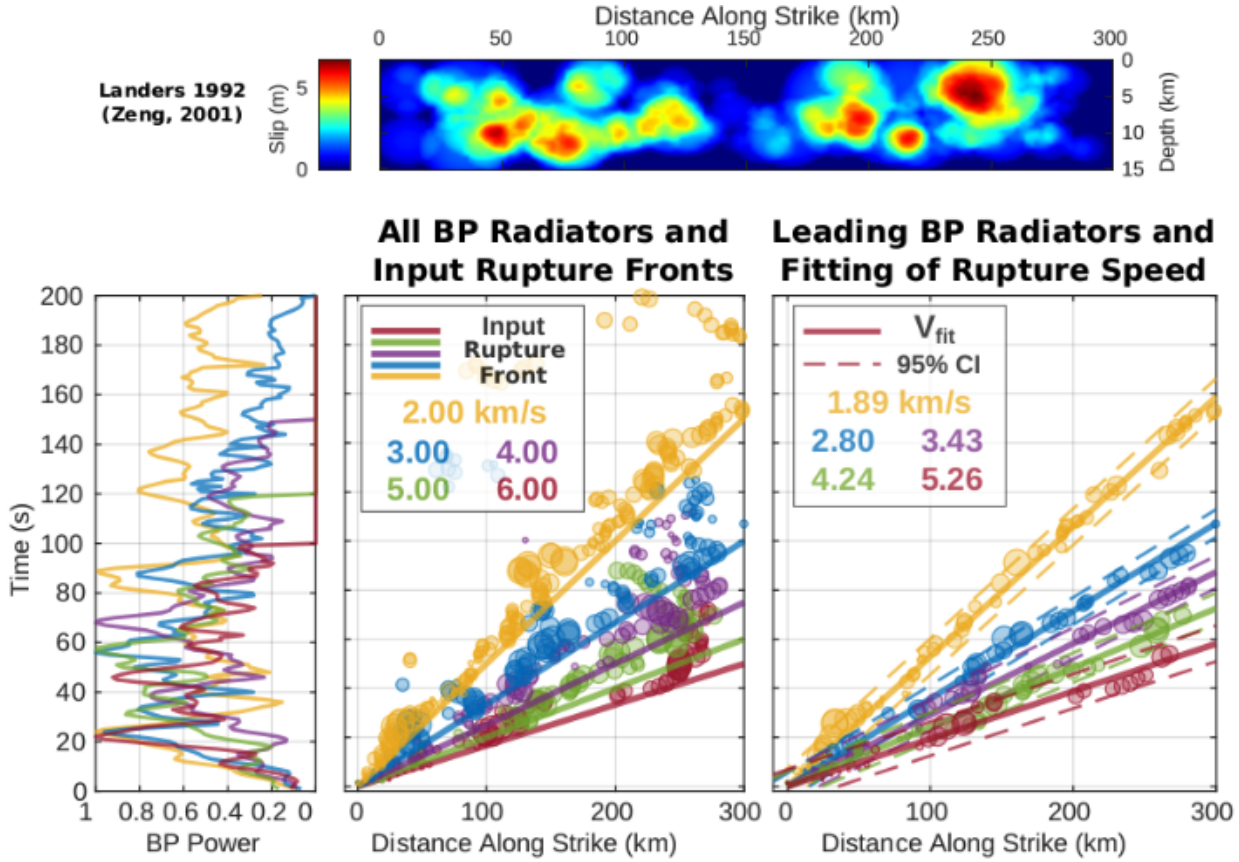

Figure 4.10: **Synthetic BPs of rupture with realistic slip distribution and constant rupture speeds (1992 Landers earthquake; the slip model is from Zeng and Andersen, 2000).** (Left) BP power as a function of time for different input rupture speeds. (Middle) Along-strike location and timing of BP radiators. Time is relative to the origin time. Location is the horizontal position relative to the hypocentre, projected along the strike direction. The straight lines indicate the speeds of the input rupture fronts (see the inset legend). (Right) Least-squares linear regressions between the timings and the along-strike distances of the leading BP radiators, defined as the furthest BP radiator at any given time. The fitted rupture speeds are shown in the inset legend. The dashed lines represent the 95% confidence interval (CI) of the fittings. This group of cases illustrate that fitting rupture speeds with only leading BP radiators is a conservative yet robust estimate. The faster a rupture speed, the greater the underestimate.

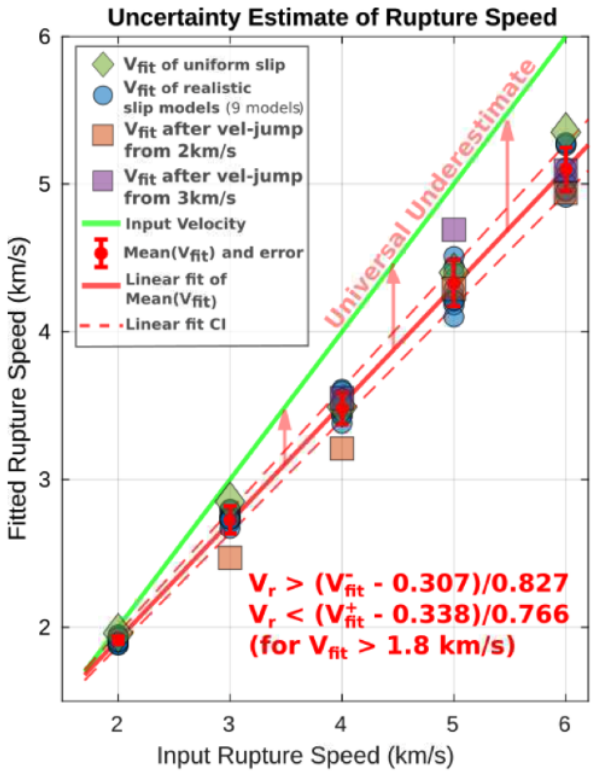

Figure 4.11: **Statistical relation between the fitted rupture speed and the true rupture speed.** The sample points are from all cases shown above: uniform slip with constant rupture speeds (green diamond; 5 cases, Fig. S12), realistic slip with constant rupture speeds (blue circles; 45 cases, Fig. S16.1 Fig. S16.9), and abrupt changes in rupture speeds from 2 km/s (orange box; 4 cases, Fig. S14) and from 3 km/s (purple box; 3 cases, Fig. S14). For each input rupture speed, the mean value and the root-mean-square (RMS) error are shown as a red circle and a red errorbar. The red solid line represents the least-squares linear regression of the mean values. The two dashed lines represent the least-squares linear regression of the mean values plus and minors the RMS errors, V_fit^+ and V_fit^-, respectively. Therefore, we propose an empirical relation between the fitted rupture speed and the true (input) rupture speed with uncertainties based on the linear regression of the two dashed lines, as shown in the red font at the bottom of the figure.

CHAPTER 5

Early and Persistent Supershear Rupture of the 2018 Magnitude 7.5 Palu Earthquake

Abstract

The speed at which an earthquake rupture propagates affects its energy balance and ground shaking impact. Dynamic models of supershear earthquakes (faster than shearwave speed Vs) often start at sub-shear speed and later run faster than Eshelby's speed ($\sqrt{2}Vs$). Here we present robust evidence of early and persistent supershear rupture at subEshelby speed of the 2018 Mw 7.5 Palu, Indonesia earthquake. Slowness-enhanced backprojection of teleseismic data provides a sharp image of the rupture process, along a path consistent with the surface rupture trace inferred by sub-pixel correlation of syntheticaperture radar and satellite optical images. The rupture propagated at a sustained velocity of 4.1 km/s from its initiation to its end, despite large fault bends. The persistent supershear speed is further validated by seismological evidence of far-field Rayleigh Mach waves. The unusual features of this earthquake probe the connections between rupture dynamics and fault structure. Early supershear transition could be promoted by fault roughness near the hypocenter. Steady rupture propagation at a speed unexpected in homogeneous media could result from the presence of a low-velocity damaged fault zone.

5.1 Introduction

While most earthquakes rupture at speeds lower than shear wave velocity, faster, socalled supershear earthquakes have been predicted by theory and simulations (Andrews, 1976; Burridge, 1973) and observed in laboratory experiments (Xia et al., 2004) and large strike-slip earthquakes (Das, 2015). Whether observable fault properties control the occurrence of supershear rupture in nature is not completely understood. Supershear ruptures have been proposed to occur on smooth and straight faults (Bouchon et al., 2010), and to be promoted on fault segments with well-developed damage zones (Huang et al., 2016; Perrin et al., 2016) and on geometrically rough faults (Bruhat et al., 2016).

On 28 September 2018 , an earthquake with moment magnitude Mw 7.5 occurred in Sulawesi, Indonesia (Figure 5.1). Its epicentre was located about 80 km north of the city of Palu. The earthquake ruptured along the Palu-Koro fault, a strike-slip left-lateral fault with a geodetic slip rate of 42 mm/ year (Socquet et al., 2019), a record of large earthquakes with magnitudes from 7 to 8 (Cummins, 2017) and previously identified seismic hazard (Cummins, 2017). This event triggered a tsunami and landslides causing more than 2,000 casualties.

Here we focus on a feature of this earthquake that is important for our fundamental understanding of earthquake mechanics. We present robust seismological evidence of an early and persistent supershear rupture, propagating steadily at a speed that is thought to be unstable. We further exploit remote sensing observations of the rupture trace geometry to discuss possible relations between rupture speeds and fault structure.

5.2 Remote Sensing Observations of the Surface Rupture

Analysis of synthetic aperture radar (SAR) and optical images provides key constraints on the rupture geometry and the distribution of fault slip of the Palu earthquake. We measure the horizontal surface deformation due to the earthquake from sub-pixel correlation of the

interferometric synthetic-aperture radar and optical images. The SAR satellite tracks are very close to anti-parallel to the strike of the rupture, so the along-track displacements are almost parallel to the fault strike and show the location of the surface rupture on land where the east side moved north (positive in Figure 5.1) and the west side moved south. Pixel tracking of optical images provides a complementary dataset that resolves the 2D horizontal deformation pattern, where the north-south correlation maps shows a similar result to the SAR pixel offset. Both datasets indicate the inferred surface rupture has major geometrical complexities and differences between northern and southern portions (Figure 5.1a). No surface rupture is discerned north of the epicenter. The southern end of the surface rupture is at 119.99°E, 1.47°S (label E on Figure 5.1a). The northern part of the rupture, from the epicenter to its intersection with the Palu Bay coast at 119.83°E, 0.69°S (label B), is less straight than the rupture from Palu city to the south. There is a substantial right-bend on the rupture at 119.83°E, 0.34°S (label A), over which the fault trace is offset by about 4 km in the direction perpendicular to the main rupture strike. The rupture from Palu city (label C) to the south is very straight until it makes a large leftbend at 119.885°E, 1.185°S (label D). The left-bend is about 8.5 km along the diagonal and 6.5 km perpendicular to the main fault strike. The northern left-bend and southern right-bend are restraining and releasing, respectively, for the left-lateral Palu earthquake. The slip distribution measured from the optical image correlation maps (see Methods) reveals the variation of fault slip along the surface rupture. The slip profile shows a maximum slip of 6 ± 0.5 m located within the city of Palu, and a clear difference in slip magnitude between the northern and southern segments, with an average slip of 1.9 m and 4.7 m, respectively (Figure 5.1b).

5.3 Teleseismic Back-projection Supershear Rupture Imaging

A fast rupture during the Palu earthquake was first suggested by a large ratio between rupture length (estimated from the distribution of aftershocks and from satellite images)

and the rupture duration inferred from teleseismic source time functions. Teleseismic source inversion properly constrains rupture duration but suffers from a strong tradeoff between rupture size and rupture speed. Owing to the advent of regional dense seismic arrays, teleseismic back-projection (BP) rupture imaging has become one of the essential techniques to constrain the kinematic rupture properties of large earthquakes, including rupture lengths, directions, speeds and segmentation (Kiser and Ishii, 2017). Without prior knowledge of the fault geometry or the rupture speed, BP determines the location, timing and relative power of coherent high-frequency sources by exploiting the coherency of seismic waveforms across dense arrays. Here we apply the Slowness-Enhanced Back-Projection (SEBP) introduced by Meng et al. (Meng et al., 2016), a combination of the high-resolution MUSIC-multitaper back-projection method (Meng et al., 2012; Meng et al., 2011) and aftershock-based calibration of the slowness bias to mitigate effects of near-source heterogeneity of the velocity structure.

The spatio-temporal characteristics of the kinematic rupture process are well imaged by SEBP of the recordings of the Australian seismic network (Figure 5.1e). The slowness calibration systematically shifts the BP locations towards the South-South-East direction and reveals a longer, and thus faster, rupture than what would be imaged without calibration (Figure 5.2). The accuracy of the calibration is supported by the agreement between the rupture lengths determined by SEBP and by remote sensing. Coherent sources with significant beampower occur until approximately 45 s after rupture initiation (Figure 5.1c). This source duration is consistent with the half-duration of 22.5 s reported by the routine USGS W-phase analysis (see data availability). The HF sources follow an overall linear rupture path towards South-South-East, consistent with the surface fault traces identified by our SAR analysis (Figure 5.1a). In two separate occasions, at around 10 s and 25 s, we observe more dispersed radiators, suggesting higher rupture complexities (Figure 5.1a). The first episode of rupture perturbation coincides with the fault bend identified in the northern part of the rupture. The second episode roughly corresponds to the location of the Palu

Bay, where the surface fault geometry is offshore and not visible on satellite images. The southernmost part of the rupture, south of the large left bend, has much smaller amplitude radiators (Figure 5.1a).

Our SEBP reveals the Palu earthquake rupture was supershear. We estimate the rupture velocity based on least-square linear regression between the timing and the along-strike distance from the hypocenter of BP radiators in the first 45 s. We ignore the radiators that are not part of the leading rupture front (Figure 5.1d). The radiators behind the leading front are likely the result of interference with the coda waves of earlier sources.

The average rupture speed estimate and its standard deviation are 4.10 ± 0.15 km/s(see supplementary section on uncertainty estimation). The local shear-wave velocity in the Crust 1.0 model (Laske et al., 2013) ranges from 3.4 to 3.8 km/s at depths between 3 and 20 km, which cover the centroid depth of 13.5 km reported in the USGS W-phase solution and the typical depth range of large slip in continental strike-slip earthquakes (Fialko et al., 2005; Xu et al., 2016). The rupture speed falls in between the local shear wave speed and the so-called Eshelby speed ($\sqrt{2}$Vs $= 4.8 \sim 5.3$ km/s). The supershear speed is sustained throughout the whole rupture, from the rupture onset to the end, as evidenced by the notable alignment of the radiators at the leading front in Figure 5.1d. Remarkably, supershear rupture persists despite the major bends of the surface rupture. Our BP analysis does not resolve an initial sub-shear rupture phase observed in other supershear earthquakes (Huang et al., 2016; Vallée et al., 2008; Wang et al., 2016).

5.4 Validation of Supershear Rupture

The supershear rupture speed indicated by our SEBP analysis is further validated by regional surface wave observations, given the absence of local strong motion data to search for a near-field signature of an S-Mach wave. The method was introduced by Vallée and Dunham (Vallée and Dunham, 2012) based on theoretical results by Dunham and Bhat (Dunham and

Bhat, 2008) and exploits the rupture directivity effect (see also Methods). For regular, sub-Rayleigh earthquakes, waves from different parts of the rupture arrive at a far-field receiver at different times. For supershear earthquakes this is also the case outside the Mach cone, but on the Mach cone waves from different parts of the rupture arrive simultaneously. Along the Rayleigh wave Mach cone, but not elsewhere, the waveforms of a large supershear rupture should be identical to those of a smaller co-located event with similar focal mechanism, at periods shorter than the rupture duration of the supershear event and longer than its rise time. Their amplitude ratio should equal their seismic moment ratio. Such waveform similarities were first observed for the 2001 Kokoxili earthquake by Vallée and Dunham (Vallée and Dunham, 2012).

We inspect the Rayleigh wave resemblance between the Palu mainshock and a smaller Mw 6.1 foreshock recorded by regional broadband stations near Indonesia and Australia. The smaller event is located 30 km south of the mainshock hypocenter and has a similar focal mechanism (Figure 5.1a). We filter the Rayleigh waves in a narrow frequency band between 15 s and 25 s to minimize the dispersion effect. We consider stations at epicentral distances up to 45° (Figure 5.3). In such a large region, the Rayleigh wave phase velocity c is heterogeneous. Taking into account the space- and frequency-dependent variability of the phase velocity computed from the GDM52 model (Ekström et al., 2012), we estimate $\bar{c} = 3.30 \pm 0.1$ km/s for the southwest side of the Palu earthquake and $\bar{c} = 3.75 \pm 0.1$ km/s for the southeast side. Based on the rupture velocity v_r resolved by SEBP, the angle between the far-field Rayleigh Mach cone and the rupture propagation direction is predicted as $\phi_M = \arccos\left(\bar{c}/v_r\right)$[20] (Figure 5.3). Nine stations are located on the eastern Rayleigh Mach cone, while only one is on the western cone due to the poor station coverage over the Indian Ocean. Waveforms from the mainshock and the foreshock are highly similar (correlation coefficients higher than 0.9) at the stations on the predicted Rayleigh Mach cone, but not at other azimuths (Figure 5.3, Figure 5.4). The amplitude ratios on the Mach cone are equal to the theoretically expected value given by the moment ratio between the two events,

which is equal to 125. Stations located inside the Mach cone, including those located in the rupture direction, have smaller but still considerable similarities due to the directivity effect, whereas stations located outside the Mach cone are the least similar. These results are consistent with theoretical expectations (see Methods) and provide immediate evidence that the supershear speed was persistent from the beginning to the end of the mainshock rupture, with a rupture velocity close to 4.1 km/s, which confirms our SEBP inferences.

5.5 Structural Controls on Earthquake Rupture Speed

The Palu earthquake rupture is supershear from very early on. In theoretical models and laboratory experiments, the transition to supershear triggered by the daughter-crack mechanism occurs at a certain rupture propagation distance (Andrews, 1976; Dunham, 2007). In that context, a short transition distance implies high initial shear stress on the fault or short critical slip-weakening distance. Early supershear can also be triggered by initial stress concentrations, which here could be due to the M6.1 foreshock or to fault roughness. Bouchon et al. (Bouchon et al., 2010) noted that supershear ruptures happen on smooth faults, but in the Palu earthquake only the southern part of the surface rupture has a relatively simple geometry. A non-unique interpretation is that the smaller slip in the north would also be consistent with stronger fault roughness there. Fault roughness in the epicentral area could have promoted the occurrence of a short-lived supershear episode, as found in dynamic rupture models, which then persisted over longer distances as the rupture continued on smoother sections of the fault, despite large-scale fault bends. Alternatively, the fault could be smoother at depth than at the surface.

Yet the supershear Palu earthquake rupture is not as fast as P waves. It is even slower than the Eshelby speed, which is at the lower end of stable supershear speeds in dynamic rupture models. Steady rupture at a nominally unstable supershear speed can result from interactions between dynamic rupture and head waves in a low-velocity damaged fault zone.

In that context, the Palu earthquake could be a stable supershear rupture running at the P wave speed of a fault damage zone with 30% reduction of wave speed relative to the host rock. Such level of rock damage is not uncommon in mature fault zones. The Palu-Koro fault has an accumulated slip larger than 100 km, large enough to have developed a mature damage zone. Pre-existing damaged fault zones also tend to shorten the supershear transition distance, which could also explain the early onset of supershear rupture in the Palu earthquake, but co-seismic off-fault damage and dissipation may either accelerate or delay the supershear transition.

Supershear ruptures have the potential to generate strong ground shaking carried by Mach wave fronts, but the severity of this effect depends on rupture speed. In particular, a rupture running at the Eshelby speed does not produce a near-field S-wave Mach cone. Establishing relations between earthquake rupture speed and structural fault properties that can be mapped in advance is thus important to anticipate the impact of future earthquakes. Further scrutiny is also warranted to determine if supershear rupture aggravated the damage and the triggering of landslides caused by the Palu earthquake.

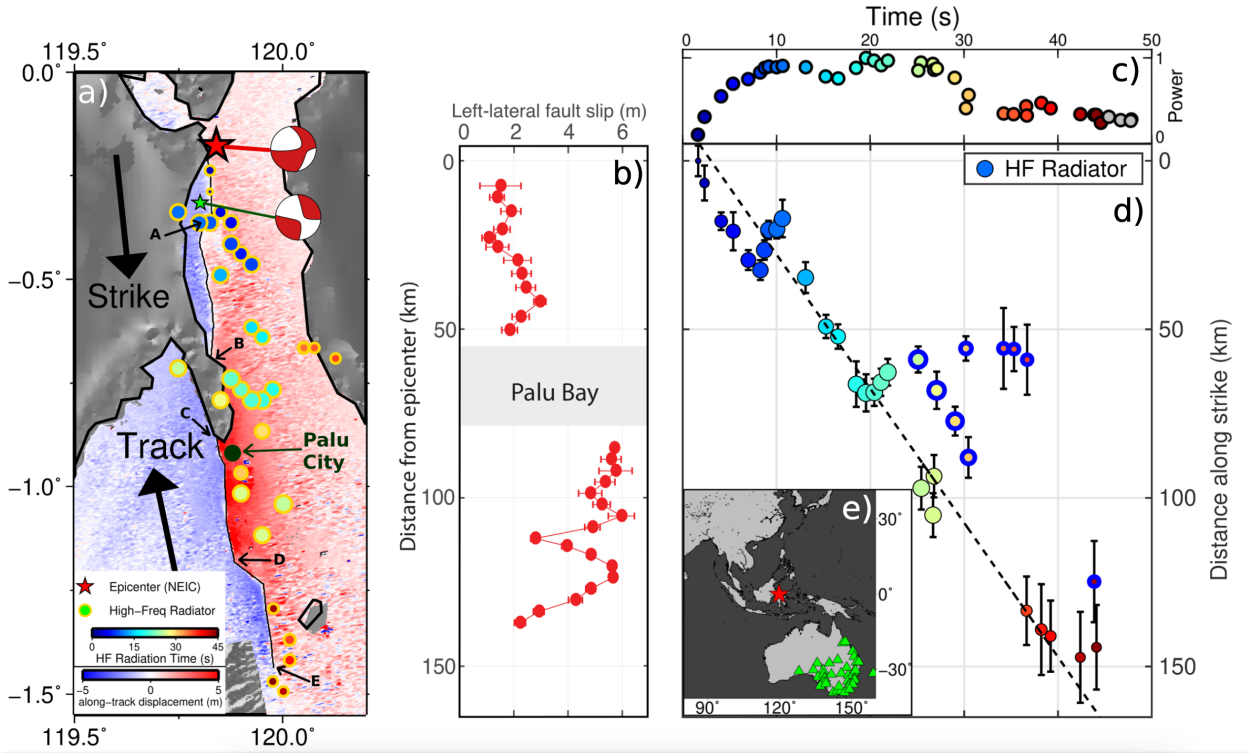
a)
119.5˚
120.0˚
0.0˚
−0.5˚
−1.0˚
−1.5˚
Strike
Track
A
B
C
D
E
Palu City
Epicenter (NEIC)
High−Freq Radiator
HF Radiation Time (s)
along−track displacement (m)
b)
Left-lateral fault slip (m)
Distance from epicenter (km)
Palu Bay
c)
Time (s)
Power
HF Radiator
d)
Distance along strike (km)
e)

Figure 5.1: **Surface rupture trace and supershear speed of the Palu earthquake.** a) Along-track displacements from ALOS-2 SAR offsets (colored image on land) and bathymetry (gray background offshore). The arrow labeled as "track" indicates the direction of measurement, 11.7°. The red star denotes the NEIC epicenter of the Palu earthquake. The green star is the relocated epicenter of the 2018/09/28 M6.1 foreshock. Mainshock and foreshock focal mechanisms are also shown. The inferred surface rupture trace is indicated by a thin black line. Circles are the high-frequency ($0.5 \sim 2$ Hz) radiators imaged by the Slowness-Enhanced BackProjection (SEBP) on data recorded by the Australia array, with size proportional to relative energy and color representing rupture time with respect to the mainshock origin time. b) Leftlateral slip distribution along the surface rupture measured from optical image correlation of Sentinel-2 and Planet Labs data. Fault slip is almost a factor of two larger on the southern segment through Palu city than north of the bay. c) Beam power as a function of time. Low-amplitude radiators after 45 seconds (gray) are not used in further analysis. d) Along-strike location and timing of radiators imaged by SEBP. Time is relative to rupture origin time. Location is the horizontal position relative to the hypocenter, projected along the average strike direction (174°). The dashed line is a linear regression of the radiators close to the leading rupture front (circles with blue rim are ignored). Error bars are location uncertainties derived from the slowness correction. e) Map showing the mainshock epicenter (red star) and stations of the Australia array used for SEBP (green triangles)

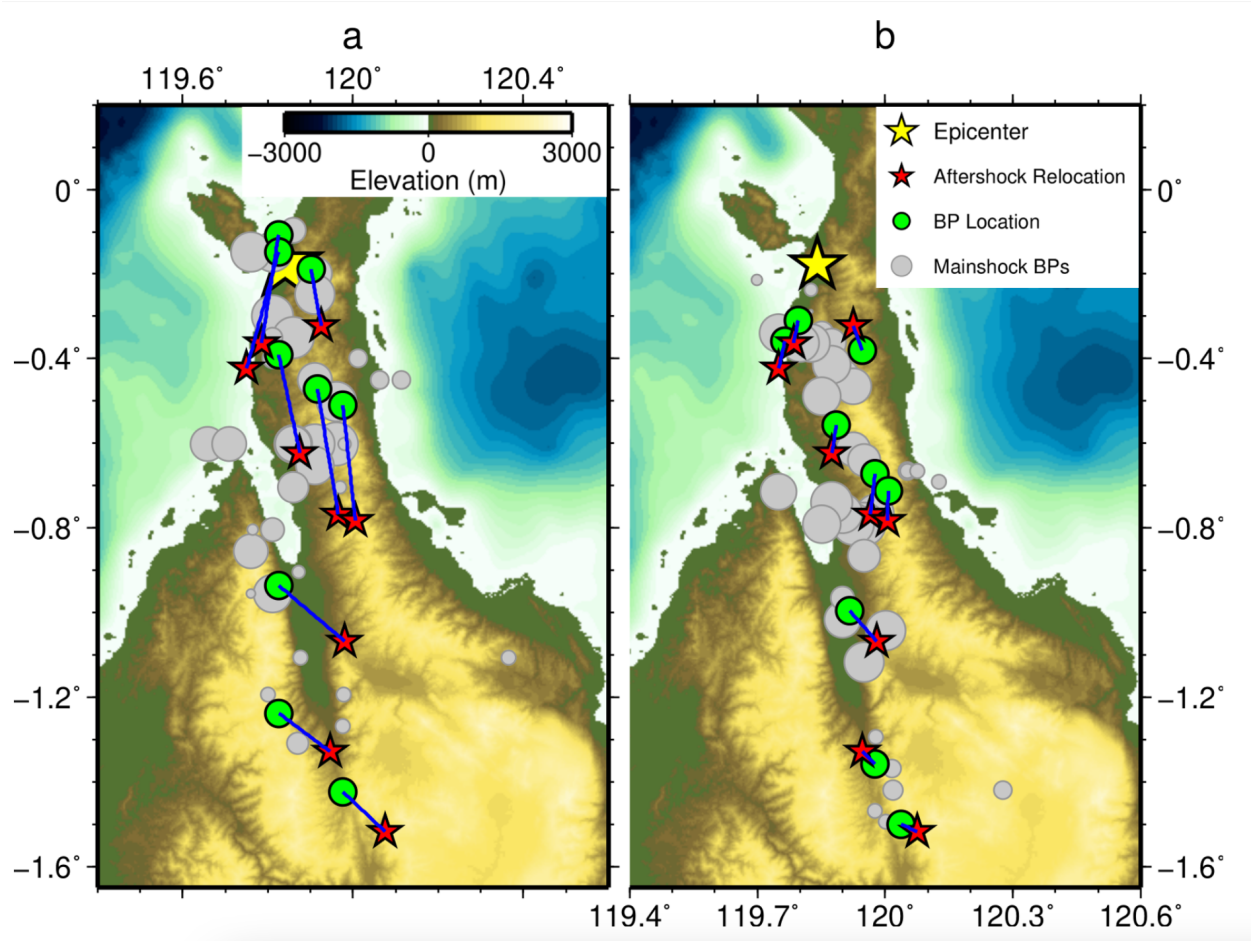

Figure 5.2: **Calibration of back-projection based on aftershock data.** BP-inferred (green circles) and relocated (red stars) locations of 9M5.0+ aftershocks spanning the rupture region, and BP radiators (gray circles) before (a) and after (b) the slowness calibration. Results shown are for Australia array.

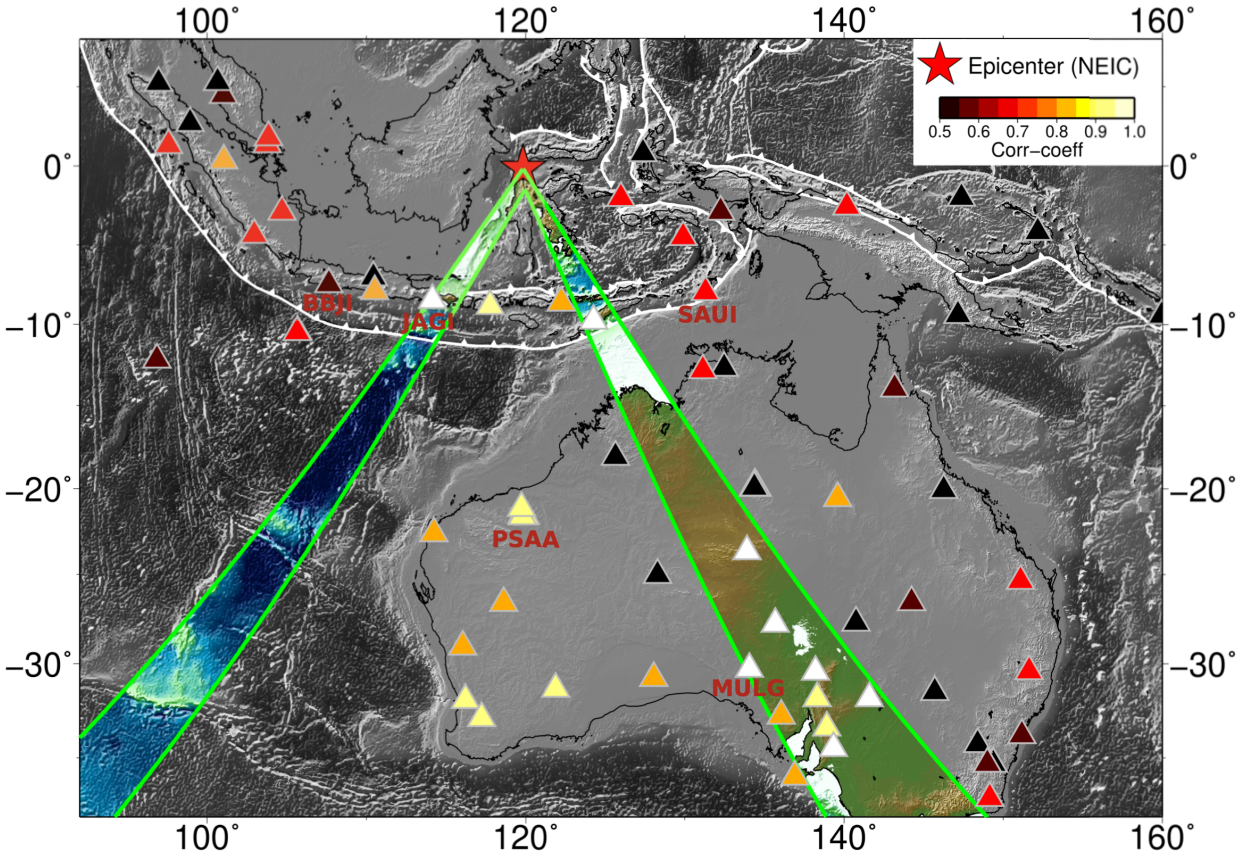

Figure 5.3: **Evidence of a far-field Rayleigh-wave Mach cone.** The colored area inside the green lines is the predicted area scanned by the Mach cone with maximum possible mach angle, based on the observed rupture velocity (4.1 km/s) and considering the uncertainty of Rayleigh wave phase velocity. The location of broadband stations are indicated by triangles. Their color indicates correlation coefficients between 15-25 s Rayleigh wave displacement seismograms of the Palu earthquake and its M6.1 foreshock. Rayleigh Mach waves recorded by five stations with names (BBJI, JAGI, PSSA, MULG, SAUI) are shown in Figure 5.4.

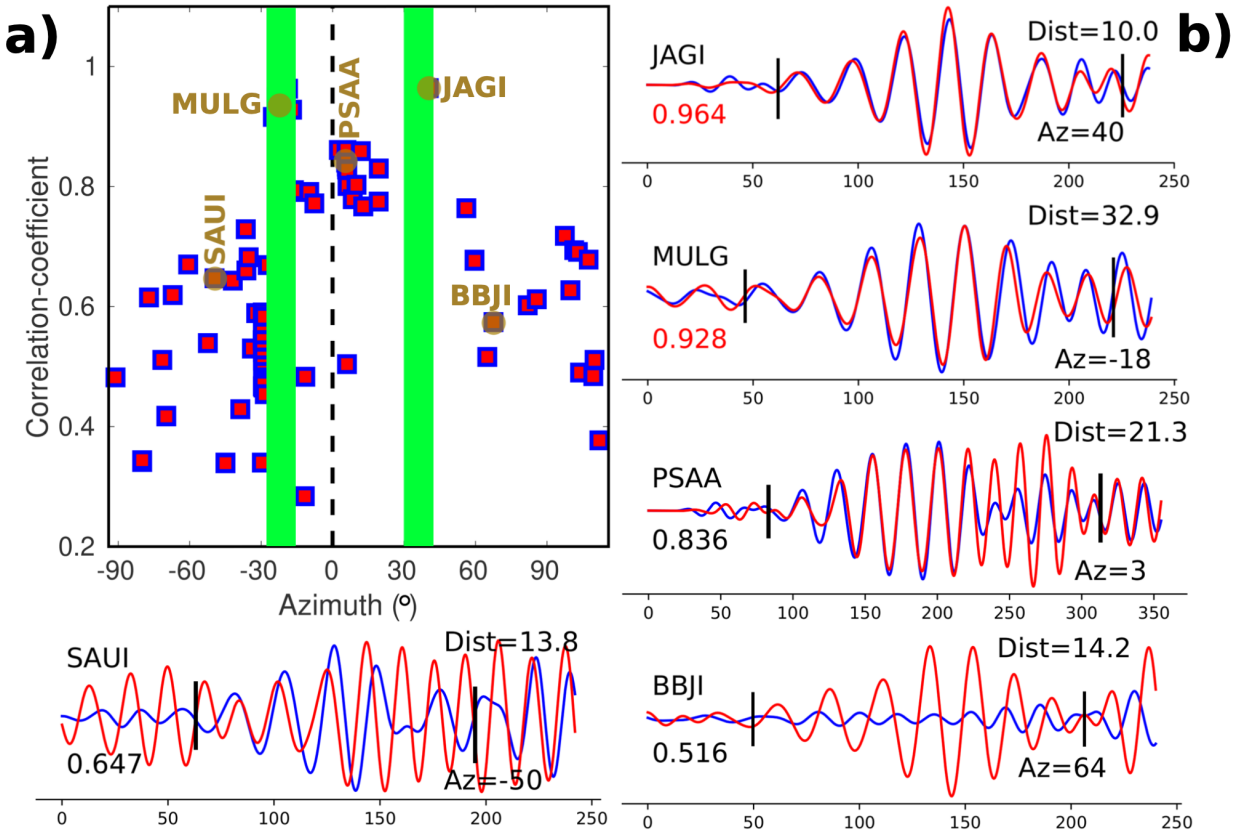

Figure 5.4: **Evidence of Rayleigh Mach waves.** a) Correlation coefficients (red squares) between 15 $\sim$ 25 s Rayleigh waves of the mainshock and its M6.1 foreshock (see Fig. 1a) as a function of stations azimuth relative to the rupture strike. The dashed line indicates the fault strike direction. The two green-colored bands indicate the estimated azimuth ranges of the two Mach cones, considering uncertainties in Rayleigh wave phase velocity and rupture velocity. The correlation coefficients reach the highest values at stations on the predicted Mach cone. b) Rayleigh wave vertical displacement seismograms of mainshock (blue) and foreshock (red) in the 15-25 s period range. Station name, azimuth (Az) relative to the rupture direction, and hypocentral distance (Dist) are shown for each station. Values of the normalized cross-correlation coefficient, based on the signal windows between the two vertical ticks, are shown in red for stations on Mach cones. Foreshock signals are scaled by the mainshock/foreshock moment ratio, 125. Names of the five chosen stations are marked in both Figure 3 and Figure 4a.

CHAPTER 6

The Global Frequency of Supershear Earthquakes

Abstract

Supershear earthquakes, whose ruptures are faster than seismic S-waves, are rare but of broad interest because they could produce destructive ground shaking and their occurrence could hold important clues about fault mechanics. Previously, only a few cases of supershear earthquakes have been reported, most of which are continental events. Here we perform a systematic global search for supershear earthquakes and report four previously undocumented oceanic supershear earthquakes, based on rupture speeds determined by Slowness-Enhanced Back-Projection and far-field Rayleigh Mach wave identification. Among all large earthquake ruptures since 2000 , we find that oceanic supershear earthquakes are as frequent as continental ones, and that at least 14.0% of Mw $\geq$ 6.7 shallow strike-slip earthquakes are supershear. We observe a wider range of stable supershear rupture speeds than predicted by 2D fracture mechanics theory, possibly explained by the presence of fault damage zones or by slip obliqueness. We attribute our findings to larger seismogenic width, bimaterial effect of oceaniccontinental boundaries, and dynamic weakening mechanisms that promote both supershear transitions and propagation.

6.1 Introduction

Supershear earthquakes, i.e. earthquakes with rupture speeds exceeding the shear wave speed, first predicted by theory and simulations (Andrews, 1976; Burridge, 1973), have been

convincingly reported for only eleven shallow strikeslip earthquakes, including the 2001Mw7.8 Kunlun and the 2018Mw7.5 Palu earthquake (Bao et al., 2019; Bouchon and Vallée, 2003) (Figure 6.1). In addition to these shallow events, only one deep supershear earthquake has been reported (Zhan et al., 2014). Rupture speed is one of the main source properties that control the impact of an earthquake: faster ruptures can generate stronger ground motions (Bernard and Baumont, 2005; Dunham and Bhat, 2008), if the effect is not diminished by source complexities and path effects (Bizzarri et al., 2010; Vyas et al., 2018). The scarcity of observed supershear ruptures hinders systematic analysis of their mechanisms, while leaving the appearance that they are rare in nature and even rarer beneath the ocean (Bouchon et al., 2010; Das, 2015; Passelègue et al., 2013). More specifically, the lack of statistical analysis makes it difficult to validate theoretical findings and to address questions such as: Do structural features control the occurrence of supershear ruptures? For instance, do they happen more often on faults with wider seismogenic widths? Do they have a preferred propagation direction due to bimaterial effects? Can they propagate at sub-Eshelby speeds (slower than $\sqrt{2}$ times S-wave speed)? To investigate these questions, here we performed a systematic global search for supershear earthquakes.

A comprehensive survey of supershear earthquakes requires robust estimates of rupture speed, enabled here by combining recent advances in seismological analysis methods. Studies based on directivity effects (Ben-Menahem and Toksöz, 1963) and teleseismic source inversions (Kikuchi and Kanamori, 1991) are challenged by the trade-off between source size and rupture speed (Beresnev, 2003), the usage of relative low-frequency (< 0.1 Hz) contents and smoothing constraints (Okuwaki et al., 2020). Those based on near-field recordings, such as array techniques (Spudich and Cranswick, 1984) and early S-arrival identification (Bouchon et al., 2001; Wang et al., 2012), are limited by the scarcity of such data. On the other hand, teleseismic or regional back-projection (BP) rupture imaging (Ishii et al., 2005) has the potential to constrain the rupture speed of large earthquakes globally, especially if travel time errors due to 3D path effects (Meng et al., 2016) are mitigated by the recently developed

Slowness-Enhanced BackProjection (SEBP) (Bao et al., 2019). This method reduces spatial biases by calibrating the path effect using recordings of nearby events (M 4-6) that have been accurately located. Because the location uncertainties of regular catalogs of oceanic earthquakes tend to be large, here we performed teleseismic double-difference relocations (Pesicek et al., 2010) to calibrate SEBP. Moreover, to properly identify imaging artifacts and quantify the uncertainties of rupture speed estimates, we conducted a comprehensive series of BP synthetic tests considering various rupture scenarios, realistic source-receiver geometry, slip distributions, waveform complexities, fault geometries, and BP parameterizations (see Method and Section 3 in Supplementary Material for details). We found that tracking the leading BP radiators significantly reduces the "shadowing" and "tailing" artifacts that distort the rupture speed estimates and that SEBP consistently underestimates rupture speed by $5\% \sim 15\%$, due to the averaging effect of direct and coda waves. Therefore, the rupture speed inferred from SEBP is a conservative indicator of supershear ruptures. We independently validated supershear rupture speeds by identifying Rayleigh Mach waves (Vallée and Dunham, 2012), a unique feature of supershear earthquakes (see Methods). Using SEBP, enhanced with relocated catalogs and comprehensive uncertainty analyses, and Mach wave identification, we searched for supershear earthquakes globally by analyzing all shallow strike-slip earthquakes (depth $\leq$ 50 km, dip angles $\geq 70^\circ$ for both nodal planes) with magnitude (Mw) $\geq$ 6.7 that occurred from Jan 1st, 2000 to Feb 1st, 2020, selected based on the International Seismological Center (ISC) focal mechanism bulletin (see Table S2 for selected events, see Text S1 for detailed event selection criteria). The magnitude threshold is based on the minimum resolvable rupture length for which rupture speeds can be reliably estimated. To be eligible for the BP analysis, we require a candidate event to be recorded by at least 50% of the stations in one of the four regional arrays in continental United States (US), Alaska (AK), pan-Europe (EU), and Australia (AU).

6.2 Results

Our analysis identifies new cases of supershear earthquakes, while confirming previously reported ones. We identified 12 large-scale supershear earthquakes (rupture length $\geq$ 50 km) including four previously unreported earthquakes (the 2009/2018 Caribbean, 2010 Papua, and 2013 South Sandwich Island events) and confirming three recently reported supershear earthquakes (2016 Romanche (Hicks et al., 2020), 2017 Komandorski (Kehoe and Kiser, 2020), and 2020 Caribbean events (Tadapansawut et al., 2021)) (Figure 6.2). Compared to these three cited studies, estimates of rupture speeds presented here should be more accurate owing to our earthquake relocations and slowness calibrations, and more objective thanks to our systematic uncertainty analysis. An additional event is labeled here as an uncertain supershear earthquake: SEBP detects supershear speeds in the 2004 Queen Charlotte earthquake, but its supershear speed can not be validated by the Mach-wave, since the pattern of highest CC values at the two sides of the frontal direction is not observed, likely due to its insufficiently long supershear rupture propagation (Vallée and Dunham, 2012) ($\sim$ 40 km). Five events show clearly an initial subshear rupture segment followed by a supershear segment. The rupture speeds of the newly detected supershear events range from moderately faster (1.1Vs $\sim$ 1.4Vs), to significantly faster (1.4Vs $\sim$ 1.7Vs) than the local shear wave speed (Vs). All of the newly identified supershear ruptures are beneath the ocean (Figure 6.3).

One set of supershear earthquakes studied here highlights that some fault systems are particularly prone to host supershear earthquakes. Three supershear earthquakes (including two previously unreported) occurred beneath the Caribbean Sea within 11 years, on the transform boundary between the North America and Caribbean plates (Figure 6.2). The 28 May 2009Mw7.3 and the 10 Jan 2018Mw7.5 events, ruptured two segments of the submarine Swan Island Fault, west of the Mid-Cayman spreading center. The 28 Jan 2020 Mw 7.7 earthquake ruptured a segment of the Oriente Fault, east of the Mid-Cayman spreading

center. The plate motion at the boundary between the North America and Caribbean plates is estimated to be $\sim$ 19 mm/yr along this segment (DeMets et al., 2010). As revealed by SEBP and Rayleigh Mach waves, all three events are supershear ruptures propagating predominantly towards southwest-west (Figure 6.2 - 6.4). We identified two episodes of supershear ruptures in the 2009 earthquake. The first episode propagated for 100 km at 5.5 $\sim$ 6.3 km/s. The speed uncertainty of the second 130-km-long segment is large (3.8 $\sim$ 5.4 km/s) due to strong shadowing artifacts around 25 $\sim$ 50 s (Figure 6.3) likely caused by abrupt changes in rupture speed and/or slip distribution. The overall rupture speed is 3.2 $\sim$ 3.8 km/s, which is similar to that reported by Graham et al. (Graham et al., 2012), 2.8 $\sim$ 4.0 km/s, based on teleseismic finite fault inversion (FFI). For the 2018 earthquake, mutually consistent BPs of multiple arrays show a 150 -km-long supershear propagation at 4.5 $\sim$ 5.5 km/s. The 2020 event is bilateral, though the eastward branch was significantly shorter than the westward one. The westward branch initially propagated for $\sim$ 80 km at a sub-Rayleigh speed of 2.2 $\sim$ 2.6 km/s and then for $\sim$ 170 km at a supershear speed of 4.6 $\sim$ 5.6 km/s. This is resolved by both Alaska and European arrays. Moreover, ground motion data of two near-fault stations, FSCY and LCCY, shows that the fault-normal particle velocity dominates that of the fault-parallel component, which is a distinctive signature of supershear ruptures (Dunham, 2005). Our result differs from the first report of the 2020 event based on teleseismic FFI, which shows supershear rupture speed $>$ 5 km/s both from 0 to 20 s and from 25 to 40 s after the rupture initiation (Tadapansawut et al., 2021). Geodetic and historical records suggest that similar-sized earthquakes in this region have a short recurrence interval of 40 $\sim$ 50yr (DeMets et al., 2010). This supershear sequence underlines that for large-scale mature transform faults along plate boundaries, potential hazards of repeating supershear earthquakes and their associated strong shaking should be of great concern. A similar situation with multiple supershear events on one transform plate boundary is the Queen Charlotte Island supershear sequence: the 2013 Craig earthquake (Yue et al., 2013) and the 28 June 2004Mw6.8 event located just 50 km in the south (Figure

6.3).

The two other newly-identified supershear earthquakes also occurred in oceanic transform faults. The 2010 Mw 7.0 Papua earthquake occurred on an unidentified fault west of the boundary between the Birds Head and Maoke microplates, which accommodates $\sim$ 80 mm/yr of left-lateral motions (Hayes, 2017). The rupture broke a 100-km-long segment with an overall rupture speed of 5.0 $\sim$ 6.1 km/s (Figure 6.2 - 6.4). The 2013Mw7.3 South Sandwich Island earthquake occurred on an east-striking fault, as a result of the fast motion of 14 mm/yr between the South America and Antarctica plates where two large events (M 7.4 in 2006 and M 7.5 in 1973) occurred in the past 50 years (Hayes, 2017). The rupture rapidly accelerated to a supershear speed of 4.9 $\sim$ 6.2 km/s after 20 seconds and propagated for $\sim$ 100 km (Figure 6.2 - 6.4).

For previously reported supershear events, our analyses bring either confirmation or further insights on their rupture pattern. In the 2016Mw7.1 earthquake that struck the eastern end of the Romanche oceanic transform fault, we identified a westward back-propagating supershear rupture after an initial sub-Rayleigh eastward rupture (Figure 6.2 - 6.4). This complex rupture pattern is consistent with the one reported in the first study of this event (Hicks et al., 2020). The 17 July 2017Mw7.7 Komandorski earthquake occurred inside the back-arc basin of the westernmost Aleutian Islands, along a 400-km-long segment of the Bering Fracture Zone (BFZ). The BFZ accommodates approximately two thirds (5.1 cm/yr) of the relative shearing motion between the Pacific and North American plates (7.8 cm/yr), creating a prime tectonic environment for large strike-slip events (Kogan et al., 2017). The spatiotemporal characteristics of the rupture process are well imaged by SEBP (Figure 6.2 - 6.4). The coherent high-frequency sources follow an overall linear rupture path towards Southeast in two episodes: initial sub-Rayleigh propagation along 50 km in the first 25 s, followed by fast supershear propagation at 4.5 $\sim$ 4.9 km/s over 200 km (Figure 6.3 - 6.4). Our result differs from the first report of this event (Kehoe and Kiser, 2020), which showed a later and much shorter supershear segment only 50 km long.

6.3 Discussion

Our results indicate that supershear earthquakes are more common than previously thought, especially owing to newly found cases in oceanic environments. Previous studies have argued that supershear earthquakes are rare (Bouchon et al., 2010; Das, 2015; Passelègue et al., 2013). Indeed, before the year 2020, only five earthquakes that occurred after 2000 had been identified as shallow supershear events, rendering a rate of 5.8% among large (M $\geq$ 6.7) strikeslip earthquakes (Table S2). Such paucity has been attributed to insufficient prestress (Passelègue et al., 2013) or complex fault geometry (Bouchon et al., 2010), and could also be favored by off-fault dissipation mechanisms (Gabriel et al., 2013). Our analysis results in a rate of supershear events at least twice as high as the previous estimate: we find that between 2000 and 2020,12 out of 86 large ($M \geq 6.7$) shallow strike-slip earthquakes were supershear, yielding a rate of 14.0%. This is a conservative estimate not accounting for uncertain supershear events (see Table S3 for full statistics). All newly reported events are oceanic supershear earthquakes (OSEs), which were previously missed possibly due to (1) lack of near-field seismic data, (2) lack of effective approaches to detect supershear rupture with teleseismic data, and (3) less public and scientific attention because of their large distance to population centers and low casualties. The newly detected OSEs demonstrate the effectiveness of SEBP and Mach wave methods in identifying supershear ruptures at teleseismic distances. Previous observations suggested that OSEs are even rarer than their continental counterparts (Das, 2015). However, we show that the probability of OSE is 14.3%, almost the same as that of continental supershear earthquakes (CSE), 13.5%. Because the identification by BP of a transition from subshear to supershear rupture requires a sustained supershear propagation longer than 50 km, as suggested by synthetic tests, the real supershear rate might be higher than our conservative estimates.

Our observations motivate the question of what controls the rate of supershear. A number of physical mechanisms might be responsible for initiating supershear ruptures. For

instance, in the Burridge-Andrews model (Andrews, 1976; Burridge, 1973; Dunham, 2007), a daughter-crack emerges ahead of the sub-Rayleigh front when the dynamic fault shear stresses between P and S waves exceed the fault strength. Other processes can facilitate supershear transition without necessarily forming daughter-cracks, including dynamic stress perturbation due to stress and strength heterogeneity (Dunham, 2005; Liu and Lapusta, 2008), non-planar fault geometry (roughness/curvature/bending) (Bruhat et al., 2016), fault step-over (Ryan and Oglesby, 2014), slip obliqueness on long strike-slip faults (Weng and Ampuero, 2019), interactions of rupture fronts with the free surface (Kaneko and Lapusta, 2010) and fault damage zones (Huang et al., 2016). Our newly estimated supershear rate of 14.0% can be compared with the supershear rate predicted in future studies by one or a combination of these mechanisms.

For some supershear mechanisms, we can identify which observable factors could in principle explain why the supershear rate is low in nature. Both in Burridge-Andrews (Andrews, 1976; Burridge, 1973; Gabriel et al., 2013) and Weng-Ampuero (Weng and Ampuero, 2019; Weng and Ampuero, 2020) theories, supershear rupture requires sufficiently high fault stress, manifested by low ratios of strength excess to stress drop and low ratios of fracture energy Gc to strain energy release rate G0, respectively. During the interseismic period, as fault stress builds up, the possibility of supershear rupture increases with time. But if nucleation happens often, large earthquakes are likely to start before the fault reaches a stress allowing supershear rupture. The rate of supershear events thus depends on a trade-off between stressing rate and nucleation rate. The former is controlled by the ratio between the long-term fault slip rate and the seismogenic width, the latter by the background seismicity rate of the fault. Studies based on observed seismicity rates and fault loading rate may provide further insights.

Our observations show evidence of bimaterial fault effects on the prevalence and rupture direction of supershear earthquakes. Slip along bimaterial faults (separating rocks with different elastic properties) produces normal stress changes, which favors rupture propaga-

tion in a certain direction (Andrews and Ben-Zion, 1997), such that supershear ruptures tend to propagate in the direction of the displacement of the stiffer side of the fault (the 'negative direction') (Shi and Ben-Zion, 2006; Weertman, 2002). Recent bimaterial-interface experiments resolving the real contact area found that, at supershear rupture speeds, the dynamic reduction of contact area due to the coupling effect of slip and normal stress was a dominant source of weakening (Shlomai and Fineberg, 2016). To investigate bimaterial effects in supershear ruptures, we classified shallow strike-slip events into three groups: continental-continental boundary (CCB), oceanic-oceanic boundary (OOB) and oceanic-continental boundary (OCB) events. Material contrasts are expected more systematically across OCB faults, with the continental side being more compliant than the oceanic side. The supershear rates (Table S3) are much larger for OCB events (83.3%) than for CCB (13.5%) and OOB events (4.7%). Thus, the dynamic weakening due to bimaterial contrast may contribute to the sustainability of OCB supershear ruptures. In addition, our result is consistent with the preferred supershear rupture direction along bimaterial interfaces: five out of the six OCB supershear earthquakes ruptured in the 'negative' direction, the exception being the 2020 Caribbean event.

We also find evidence that larger seismogenic widths and greater fault maturity promote the sustainability of supershear ruptures. Recent theoretical studies of elongated ruptures show that the energy ratio Gc/Go on vertically-bounded faults, which controls their rupture speed, is inversely proportional to the seismogenic width (Weng and Ampuero, 2019; Weng and Ampuero, 2020). For shallow strike-slip events the seismogenic depth is limited by the crustal thickness, which is correlated with the plate thicknesses above Moho and above the lithosphereasthenosphere boundary (LAB) (Table S4). According to the World's Ocean Crust Model, the average thickness above LAB of the OSE source regions is 91 km, substantially thicker than that of the nonsupershear events (65 km). The average thickness above Moho of the supershear-rich regions (the Caribbean Sea and the Queen Charlotte islands) is 17.6 km, thicker than that of the non-supershear regions (11.2 km). These statistics indicate

the seismogenic zones of all identified supershear earthquakes are wider, which is consistent with lower energy ratios and faster ruptures (Weng and Ampuero, 2020). Moreover, the supershear-rich faults tend to have tectonic slip rates larger than 1.9 cm/yr, lengths exceeding 800 km and relatively straight geometries (DeMets et al., 2010; Kogan et al., 2017; Yue et al., 2013), which suggests that these conditions are favorable for supershear propagation (Perrin et al., 2016; Weng and Ampuero, 2019). Faults without these conditions, such as the slow and poorly developed fault hosting the 2010 Papua event and the geometrically complex fault hosting the 2018 Palu event (Bao et al., 2019), still produce supershear ruptures, although globally more rarely.

Our observations also provide robust evidence of supershear ruptures with rather unexpected speeds. Theories of fracture mechanics in 2D predict the stable range of supershear rupture speed is between the Eshelby speed ($\sim \sqrt{2}$Vs = 1.41Vs) and Vp(Burridge, 1973; Freund, 1979). However, our results indicate supershear rupture speeds as slow as 1.15Vs compared to a reference Vs at 10 km depth, or 1.11Vs compared to a reference Vs at GCMT centroid depths, according to the CRUST1.0 model (Table S5). In particular, the 2017 Komandorski event ruptured along 200 km at a speed of 1.11Vs $\sim$ 1.21Vs, significantly below the Eshelby speed (even after accounting for BP uncertainties, and confirmed by the Rayleigh-Mach-wave approach; see Methods). Such "slow" stable supershear ruptures may result from reduced wave speeds at shallow depth (Kaneko and Lapusta, 2010) (slip was concentrated in the upper 15 km Lay et al., 2017) or in the fault damage zone (Bao et al., 2019; Huang et al., 2016; Oral et al., 2020), or from slip obliqueness (Weng and Ampuero, 2020) (rake of 18° reported for the Komandorski event).

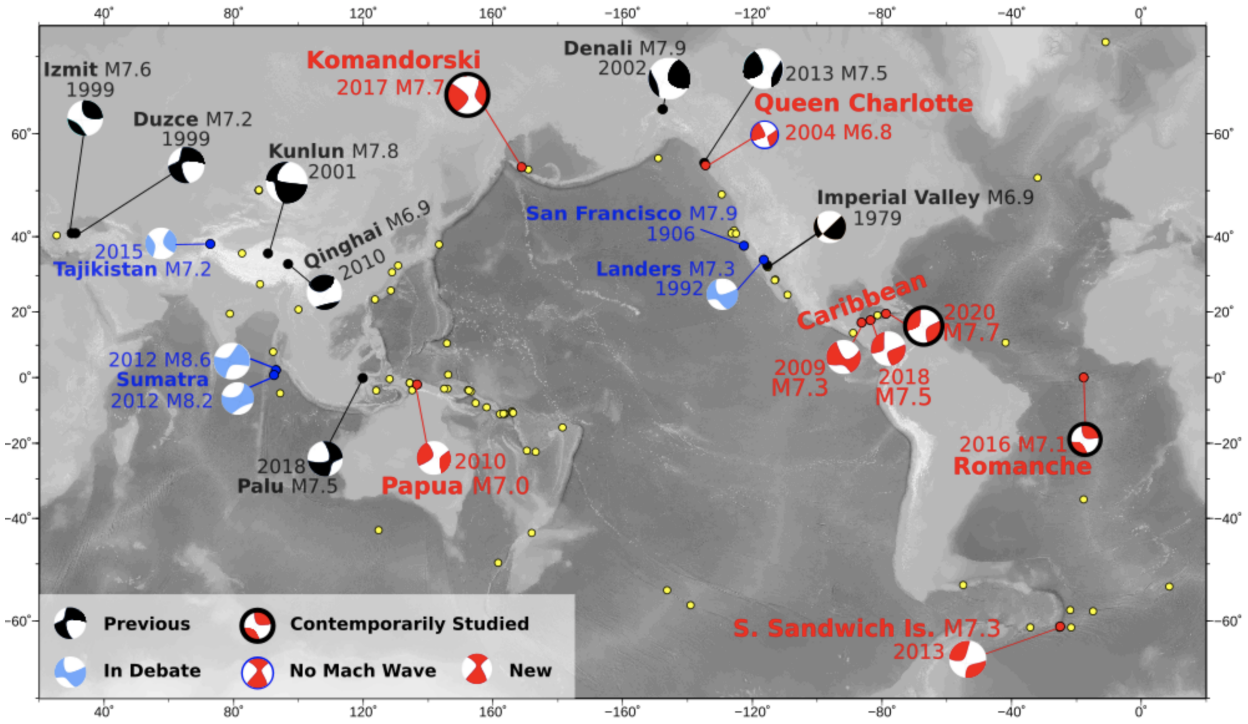

Figure 6.1: **Global supershear earthquakes.** Eight previously reported shallow strike-slip supershear earthquakes (black circles); five previously reported supershear earthquakes with debated evidence (light blue circles); four newly identified supershear earthquakes based on SEBP with evidence of Mach cones (red circles without edges); three supershear earthquakes recently studied by other groups (red circles with black edge); and one earthquake with a supershear rupture speed estimated from SEPB but without identified Mach waves (red circles with blue edge). All other examined large ($M \geq 6.7$) shallow strike-slip events without resolvable supershear ruptures are marked by yellow dots.

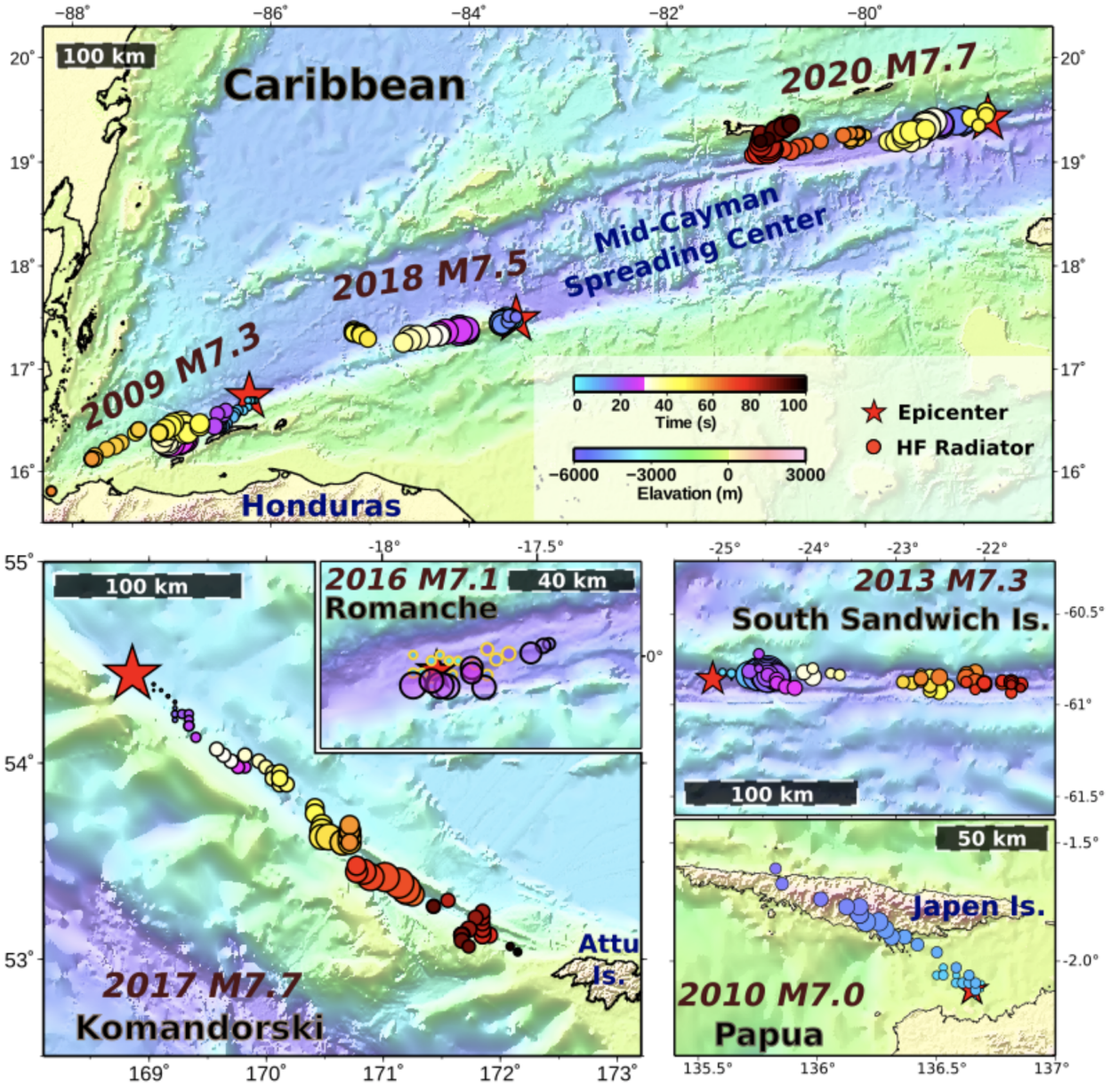
Caribbean
100 km
2020 M7.7
Mid-Cayman
Spreading Center
2018 M7.5
2009 M7.3
Honduras
0 20 40 60 80 100
Time (s)
−6000 −3000 0 3000
Elavation (m)
Epicenter
HF Radiator
2016 M7.1
Romanche
40 km
100 km
2017 M7.7
Komandorski
Attu
Is.
2013 M7.3
South Sandwich Is.
100 km
50 km
Japen Is.
2010 M7.0
Papua

Figure 6.2: **Spatiotemporal distribution of high-frequency (HF)** ($0.5 - 2$ Hz) **radiations imaged by SEBP.** The circles denote the HF radiators color-coded by rupture time with their sizes proportional to the normalized BP power. The red stars denote the National Earthquake Information Center (NEIC) epicenters for each of the seven supershear earthquakes. The transparent circles of the 2016 Romanche earthquake highlight the back-propagation (southeast-eastward) rupture. The substantial contrast of the color palette near 30sec is to emphasize the rupture evolutions of shorter and smaller earthquakes like the 2010M7.0 Papua earthquake.

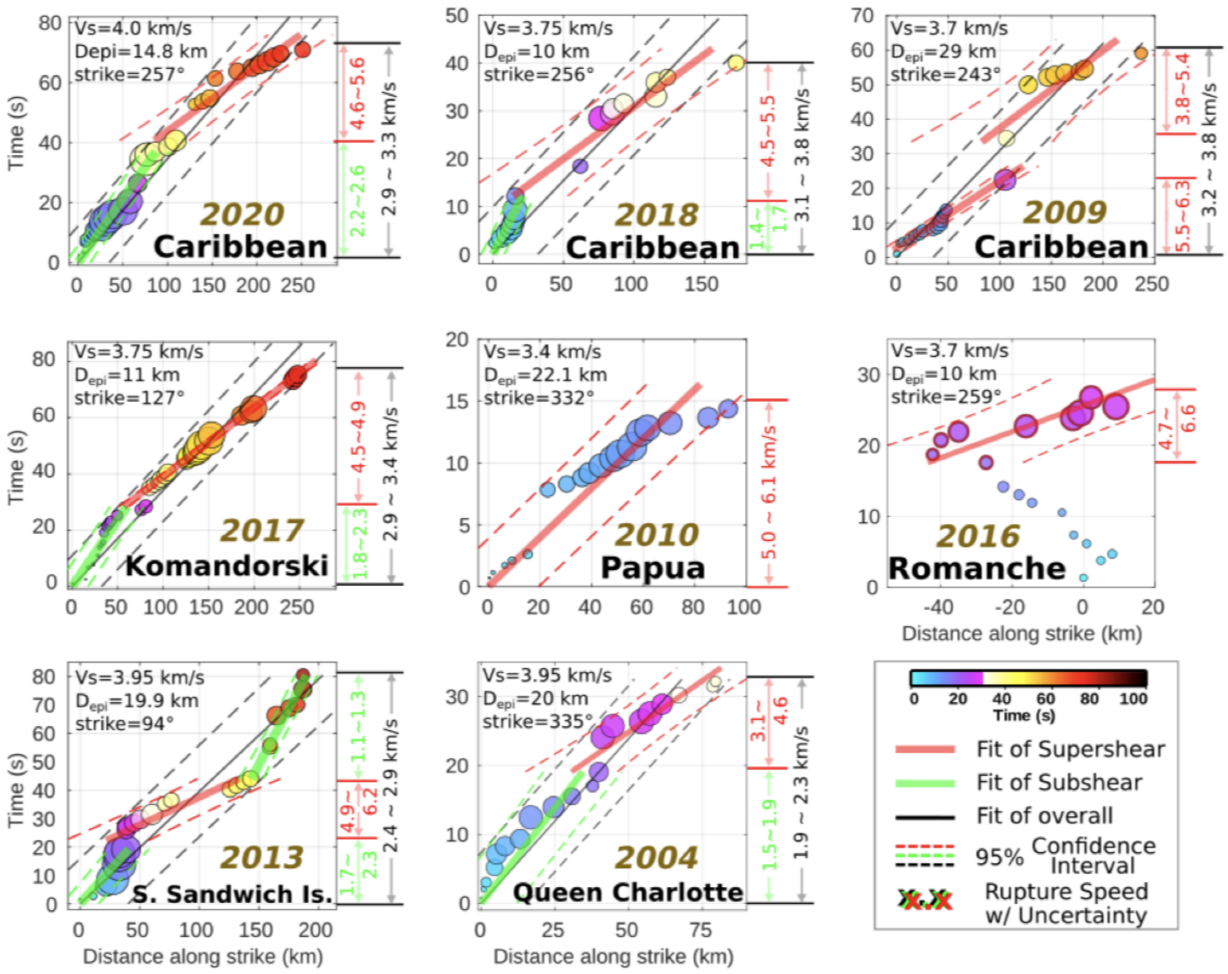

Figure 6.3: **Estimated rupture speeds of the supershear earthquakes.** The along-strike distances (relative to the hypocenter) of the leading HF radiators imaged by SEBP are plotted against the rupture times (with respect to the origin time). Black (red/green) solid lines and dashed lines are overall (supershear/subshear) rupture speeds and uncertainties estimated based on linear regressions of the radiators, respectively. Through synthetic tests, we found that tracking the leading BP radiators avoids the "shadowing" and "tailing" artifacts that distort the rupture speed estimates (Fig. S15). We also found that the estimated rupture speed is consistently underestimated by 5% $\sim$ 15% (Fig. S17). Therefore, the rupture speed inferred from SEBP is a conservative indicator of supershear ruptures.

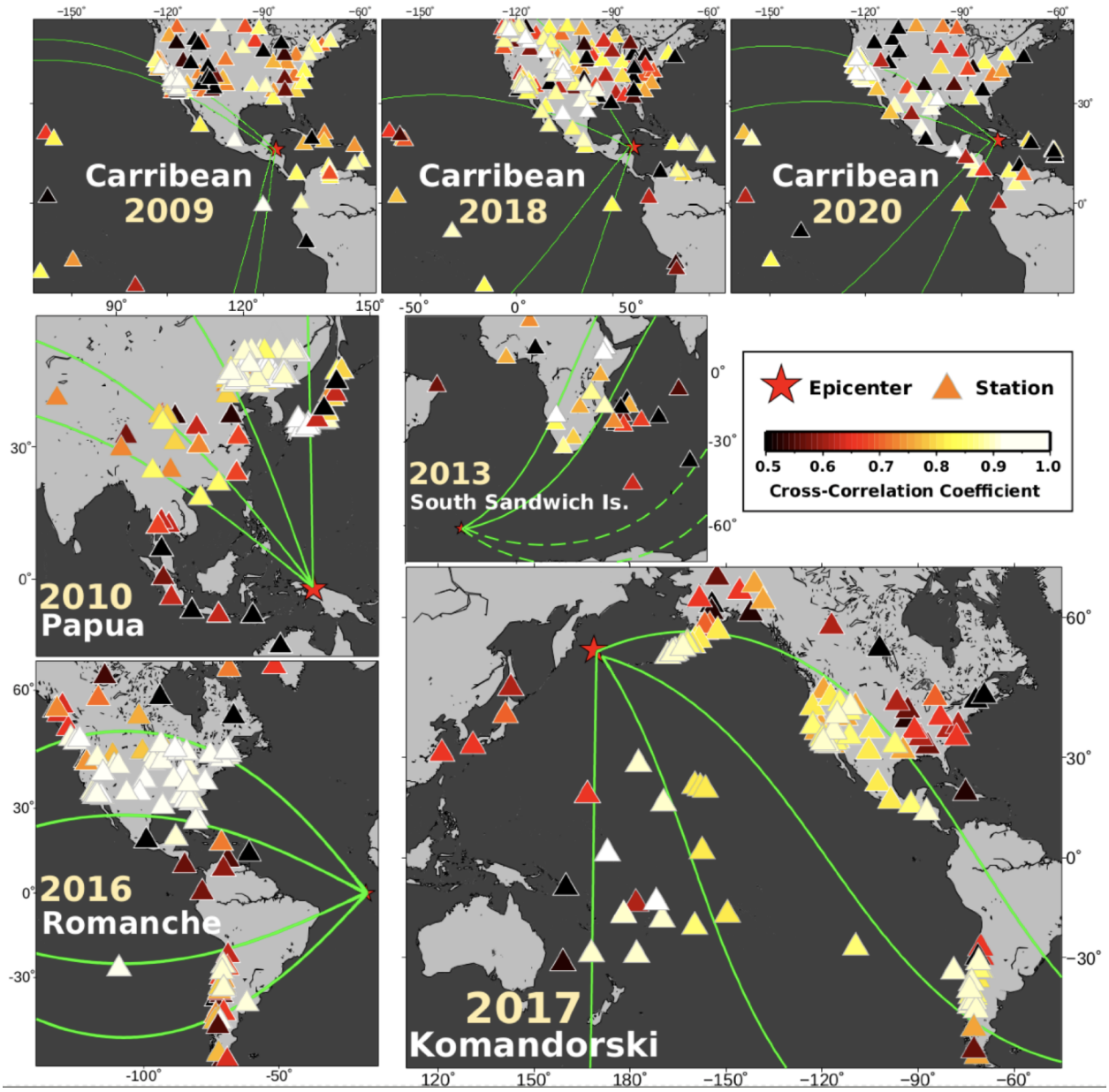
Carribean
2009
Carribean
2018
Carribean
2020
2010
Papua
2013
South Sandwich Is.
2016
Romanche
2017
Komandorski
Epicenter
Station
0.5 0.6 0.7 0.8 0.9 1.0
Cross-Correlation Coefficient

Figure 6.4: **Evidence of far-field Rayleigh-wave Mach cones.** The area within any two closed green lines is the maximum area predicted by all possible Mach angles, based on the observed rupture speed and the lateral variation of the Rayleigh wave phase velocity (Table S14). The locations of the broadband stations are denoted by triangles. Their color indicates the correlation coefficients of Rayleigh-wave displacement seismograms of the supershear earthquakes and their EGF events (Table S14). The waveform comparisons are shown in Fig. S26.1 to S26.7. The dashed green lines in the figure of the 2013 South Sandwich Island event denote the right-hand side of the predicted Mach cone without any data coverage.

CHAPTER 7

Constrain the Rupture Downdip Limit in the 2011 Mw 9.1 Tohoku Earthquake

Abstract

Besides supershear earthquakes, we can also apply back-projection on other kinds of rupture kinematics. Here we investigate the spatial bias in the Tohoku region, a larger and complex source area, by analyzing 109 M4-M7 earthquakes in the source region of the 2011 Mw 9.1 Tohoku earthquake. We find a similar reduction as previous SEBP studies in spatial biases, from ∼20 km to ∼10 km, when applying regional SEBP. This indicates that half of the spatial biases are aleatory uncertainties that are caused by regional structural complexity and can be calibrated with SEBP, while the residue errors are epistemic uncertainties that are random and caused by local velocity heterogeneities. By applying the regional SEBP to the 2011 Tohoku earthquake, we find that high-frequency radiators did not reach beyond the down-dip limit of interplate seismicity, indicating that it is likely that the coseismic slip did not penetrate into the brittle-ductile transition zone. Such observations suggest that the enhanced dynamic weakening mechanism due to thermal pressurization effects may not be activated during the Tohoku earthquake as is proposed for other large earthquakes that penetrated the roots of seismogenic zones.

7.1 Introduction

In this study, we applied regional SEBP to the source region of the 2011 Mw 9.1 Tohoku earthquake, one of the largest and most complicated earthquakes ever recorded in history. We investigated spatial biases of over a hundred M4-M7 events and used the K-means clustering algorithm (MacQueen, 1966) to automatically divide the source regions. We found a similar 50% reduction in De after adopting regional slowness corrections. By applying regional SEBP to the Tohoku mainshock, we found that its coseismic slip did not penetrate the down-dip limit of interplate seismicity. This finding is consistent in the BPs of both the United States (US) array and the European (EU) array. In summary, our studies quantify and reduce the spatial biases of BP, which gives rise to more accurate interpretations of earthquake source physics.

7.2 Spatial Biases in the Tohoku Region

We further applied the regional SEBP to the source region of the 2011 Mw 9.1 Tohoku earthquake, one of the largest and most complicated earthquakes ever recorded. Seismic velocity structure in subduction zones contains strong contrast: high P-wave velocities inside the cold slab and low P-wave velocity in the mantle wedge. Therefore, the velocity structures surrounding interplate and intraplate events may be significantly different even if they are close by. For our analysis, we choose only the interplate events (Figure 7.1b), not intraplate events in the hanging-wall or footwall, to make sure that ray paths go through similar velocity structures. This procedure also ensures that the derived slowness corrections are applicable to the mainshock which occurs primarily along the plate interface. The selection criteria of interplate events follows that of Asano et al., (Asano et al., 2011): (1) rake angle $\lambda \geq 0°$, (2) Kagan's angle (Kagan, 1991) $\theta \leq 35°$, (3) The difference between the centroid depth and the plate boundary $\delta d \leq 20$ km. The Kagan's angle is the minimum rotation angle of the focal mechanisms relative to a reference mechanism, which is used to select events with similar

focal mechanisms as the megathrust mainshock. The reference mechanism of the 2011 Mw 9.1 Tohoku earthquake is set as: strike $\phi = 195°$, dip $\theta = 13°$, rake $\lambda = 90°$ (USGS). The Slab 2.0 model is used to constrain depths of the slab interface.

A total number of 109 M4-M7 interplate events in the Tohoku region are investigated (Figure 7.1). The extensive spatial coverage of earthquakes in this region provides us with an unprecedented number of samples to study the De of BP. We used both the USarray (US, 267 stations) and European array (EU, 369 stations), so that the results can be cross-examined. Waveform data are downloaded from the Data Management Center (DMC) of the Incorporated Research Institutions for Seismology (IRIS) (https://ds.iris.edu/wilber3) and Observatories & Research Facilities for European Seismology (ORFEUS, 1987).

Figures 7.1d show the spatial biases De of the 109 investigated events with the Tohoku mainshock as the reference event. Clear patterns of De are found in some regions, for example, in the northwest (offsetting westward) and southwest (offsetting northwestward), while the patterns in other regions are less systematic. We again attempt to reduce De using regional SEBP. To properly group the investigated events into regional clusters, we adopt K-means clustering based on the event locations (MacQueen, 1966). It aims to partition N observations into K clusters in which each observation belongs to the cluster with the nearest mean. We are aware that the choice of the value of K (number of clusters) can be subjective so we tried four different values (K = 4, 5, 6, and 7). Since K=6 gives the most visually consistent clusters, we consider it optimal and show its results in Figure 7.1d. The results show that a regional SEBP strategy effectively reduces De in the Tohoku region. Figure 7.1c shows the modeled GEV distribution of De before and after calibration, and Figure 7.1e shows the residue De after calibration. SEBP reduced the mean value of De from 24.2 km to 13.6 km, a 44% reduction. The effectiveness of regional SEBP is also demonstrated with the European array. Similar to Figure 7.1, Figure 7.2 shows the spatial biases of the Tohoku region before and after calibration. The mean value of De reduced by 43% from 20.8 km to 11.9 km.

7.3 Application of SEBP to the 2011 M9.1 Tohoku Earthquake

By further applying the SEBP to the mainshock of the 2011 M9.1 Tohoku earthquake, we found that the sources of high-frequency radiations of the 2011 Mw 9.1 Tohoku earthquake likely did not expand beyond the down-dip limit of the seismogenic zone. Figure 7.3 shows the US and EU BP results of the 2011 Tohoku mainshock before and after the slowness calibration. The results are overall consistent with previous BP studies (Kiser and Ishii, 2011; Koper et al., 2012; Meng et al., 2011; Wang and Mori, 2011; Yao et al., 2013), where high-frequency radiations initiated with a slow down-dip expansion and then propagated towards southwest (see Lay, 2018, for a comprehensive review of the 2011 Tohoku earthquake). However, what we found differently is that in the uncalibrated BPs, high-frequency radiators went beyond the seismogenic down-dip limit, while those of the calibrated SEBP stopped right above the boundary. The down-dip limit shown in Figure 7.3 is based on the bottom boundary of the interplate seismicity that occurred from April 1992 to August 1998 and the depth of the down-dip limit ranges from 40 to 50 km estimated from the upper boundary of the subducting Pacific slab. The interplate events are defined using the same criteria as mentioned above (rake angle, Kagan angle and the relative distance to the slab interface).

7.4 Discussion and Conclusion

We systematically investigated the characteristics of De in the Tohoku region as well as the effectiveness and limitation of the Slowness Enhanced Back-projection (SEBP). We found the average De in the region is $\sim$ 20 km, and the amplitude of De has a positive correlation with the hypocenter distance. We also found that the regional SEBP reduced De by $\sim$ 50%, to an average value of $\sim$ 10 km. We argue that the requirement of the regional SEBP is likely due to the fact that the investigated source regions are large (400 $\sim$ 500 km) and the velocity structures beneath the source region can not be considered uniform. It also suggests that the previous applications of the uniform SEBP (e.g., the 2015 Mw 7.8 Gorkha (Meng

et al., 2016), the 2015 Mw 7.2 Tajikistan (Sangha et al., 2017), the 2015 Mw 8.3 Illapel (Meng et al., 2018), and the 2018 Mw 7.5 Palu earthquakes (Bao et al., 2019)) are likely due to their relatively small rupture length ($\leq$ 150 km) and hence smaller lateral velocity variation. We also note that the K-means clustering based on event locations is effective in partitioning zones in a regional SEBP study. Other location-based clustering methods like PAM clustering and OPTICS clustering may also be effective. In the future work, we will explore partitioning regions based on velocity structures depicted by tomographic models or fault segments divided by incoming seamounts shown in high resolution bathymetry. Our case study of the large and complex Tohoku region can serve as a benchmark that shows the effectiveness of the regional SEBP.

Down-dip Penetration of the 2011 Tohoku Earthquake

Our SEBP result of the 2011 Tohoku earthquake shows that its coseismic slip likely did not penetrate the seismogenic down-dip limit, which may provide unique insights into rupture dynamics of megathrust earthquakes. Results of previous observational studies indicate that the 2011 Tohoku earthquake may have a down-dip penetration. For example, previous BP studies show that sources of high-frequency radiations extended below the down-dip limit which is shown in Fig.S10 (Koper et al., 2012; Meng et al., 2011; Yao et al., 2013), and many finite-fault models indicate significant coseismic slip below the down-dip limit: 10–20 m (Ide et al., 2011), 5–10 m (Ammon et al., 2011; Yue & Lay, 2013; Melgar and Bock, 2015), 4–8 m (Hayes, 2011). Most of these studies did not focus on this feature and did not provide any discussion. However, if such a down-dip penetration is true, it should be of great interest because it challenges the traditional view that ruptures stop at the brittle-ductile transition. In a standard conceptual model for active faults (Figure 7.4), seismogenic (brittle) zones are mainly controlled by velocity-weakening (VW) frictions which host large earthquakes with fast seismic slips, while the ductile regions, located beyond and below the seismogenic zone, are often associated with velocity-strengthening (VS) frictions which only hosts aseismic

creeping and slow earthquakes (Burgmann et al., Science 2000; Chlieh et al., JGR 2008; Perfettini et al., Nature 2010). Therefore, it would be surprising if the coseismic slip of the 2011 Tohoku earthquake penetrated into the ductile zone. We elaborate this matter further here given the remarkable agreement between the SEBPs of both the US and EU arrays: the sources of high-frequency radiations did not expand beyond the down-dip seismogenic limit. Moreover, Figure S11 provides another example showing the high-frequency radiators of the 2015 Mw 8.3 Illapel earthquake stopped right at the down-dip limit of interplate seismicity (Meng et al., 2018). Jiang and Lapusta (2016) investigated the possible mechanisms of down-dip penetrations on strike-slip faults using dynamic rupture simulations. They found that an activation of dramatic weakening (DW) due to thermal pressurization of pore fluid enables rupture into the otherwise aseismic velocity strengthening region (Figure 7.4). Such an enhanced dynamic weakening of fault frictional resistance occurs at slip rates $\leq$ 0.1 m/s (Di Toro et al., 2017; Rice 2006), which has critical impacts on earthquake rupture propagation and effectively turns the creeping fault regions into seismic ones (Platt et al., 2014; Noda & Lapusta, 2013). However, the absence of deep penetration beyond the down-dip seismic limit in the Tohoku and Illapel earthquake suggests that the coseismic slip rate at the bottom of the seismogenic zone was not fast enough to trigger the dramatic weakening (DW) at the ductile region of the megathrust. An alternative scenario is that the down-dip penetration did occur but the BP is incapable of resolving it. This is possible if the rheology in the ductile region is too smooth and lack material heterogeneity to efficiently generate strong high-frequency radiations. We consider this as a less plausible scenario. If such deep penetration did exist, the stress shadow caused by the deep coseismic slip would shut off aftershocks near pre-seismic down dip limit. However, this is not the case based on the distribution of interplate aftershocks in Tohoku (Asano et al., 2011). We note that further numerical scrutiny and a systematic review of down-dip rupture extension of subduction zone earthquakes should be warranted.

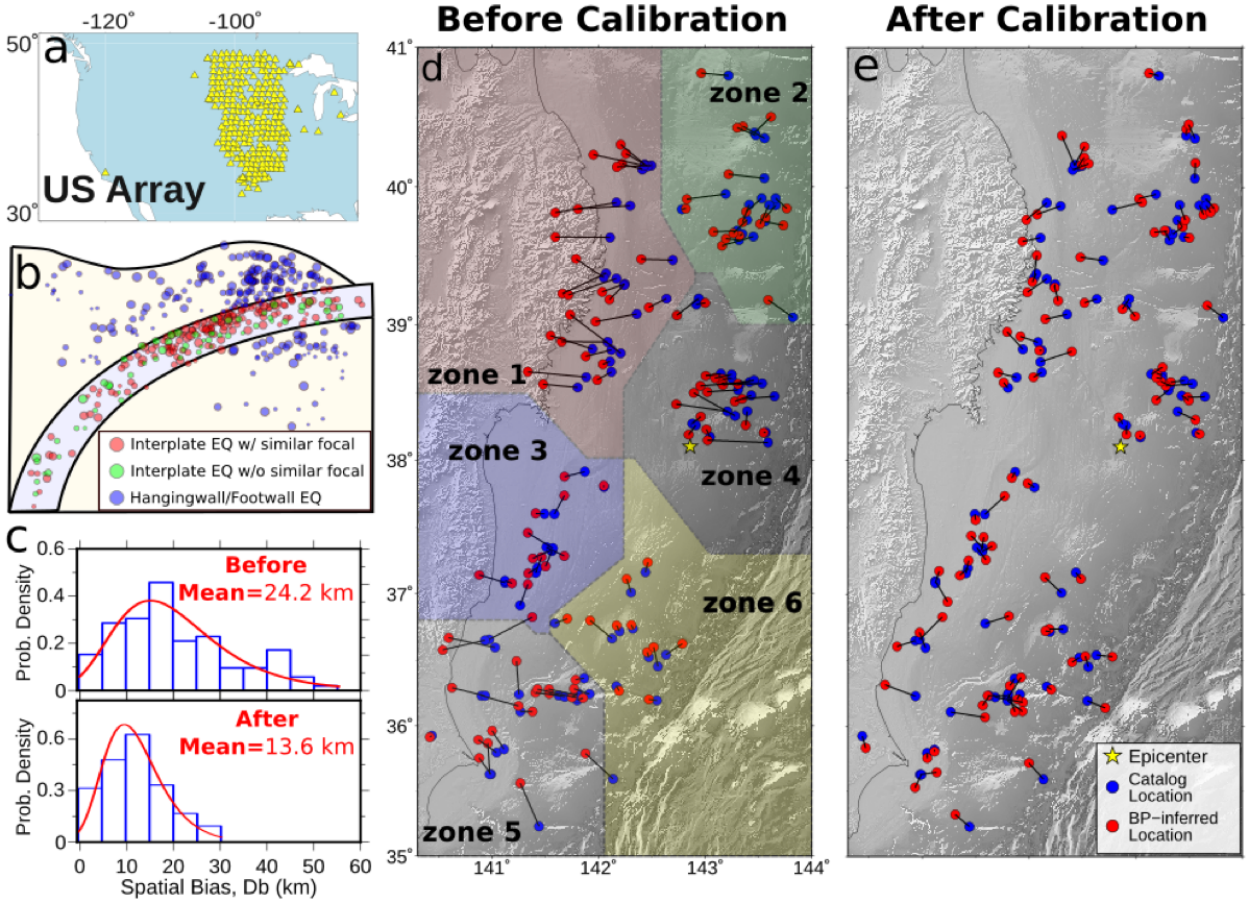
a
-120°
-100°
50°
30°
US Array
b
Interplate EQ w/ similar focal
Interplate EQ w/o similar focal
Hangingwall/Footwall EQ
c
Before
Mean=24.2 km
After
Mean=13.6 km
Prob. Density
Spatial Bias, Db (km)
Before Calibration
After Calibration
d
e
zone 1
zone 2
zone 3
zone 4
zone 5
zone 6
41°
40°
39°
38°
37°
36°
35°
141°
142°
143°
144°
Epicenter
Catalog Location
BP−inferred Location

Figure 7.1: **(US array) The effectiveness of the slowness calibration of Back-projection.** (a) The US array (267 stations) that is used in this study. (b) Illustration of the classification of seismic events in the subduction zone based on their relative distance to the slab interface and focal mechanisms. The group of interplate earthquakes with similar focal mechanisms (red circles) as that of the 2011 Mw 9.1 Tohoku earthquake are investigated here. The classification follows Asano et al., (2011). (c) Distribution of De of the 109 M4 M7 investigated interplate events with similar focal mechanisms as that of the 2011 Mw 9.1 Tohoku earthquake. The fitted probability density function (PDF) follows a generalized extreme value (GEV) distribution. (d) The spatial biases (black line) of the 109 events, as measured by De, the distance of the image peak (BPI location, red circle) from the epicenter (JMA location, blue circle), which is defined in the same way as Fan & Shearer (2017). Colored regions are segmented automatically by K-means clustering based on distribution of events' horizontal locations. (e) Same as (d) but after regional SEBP.

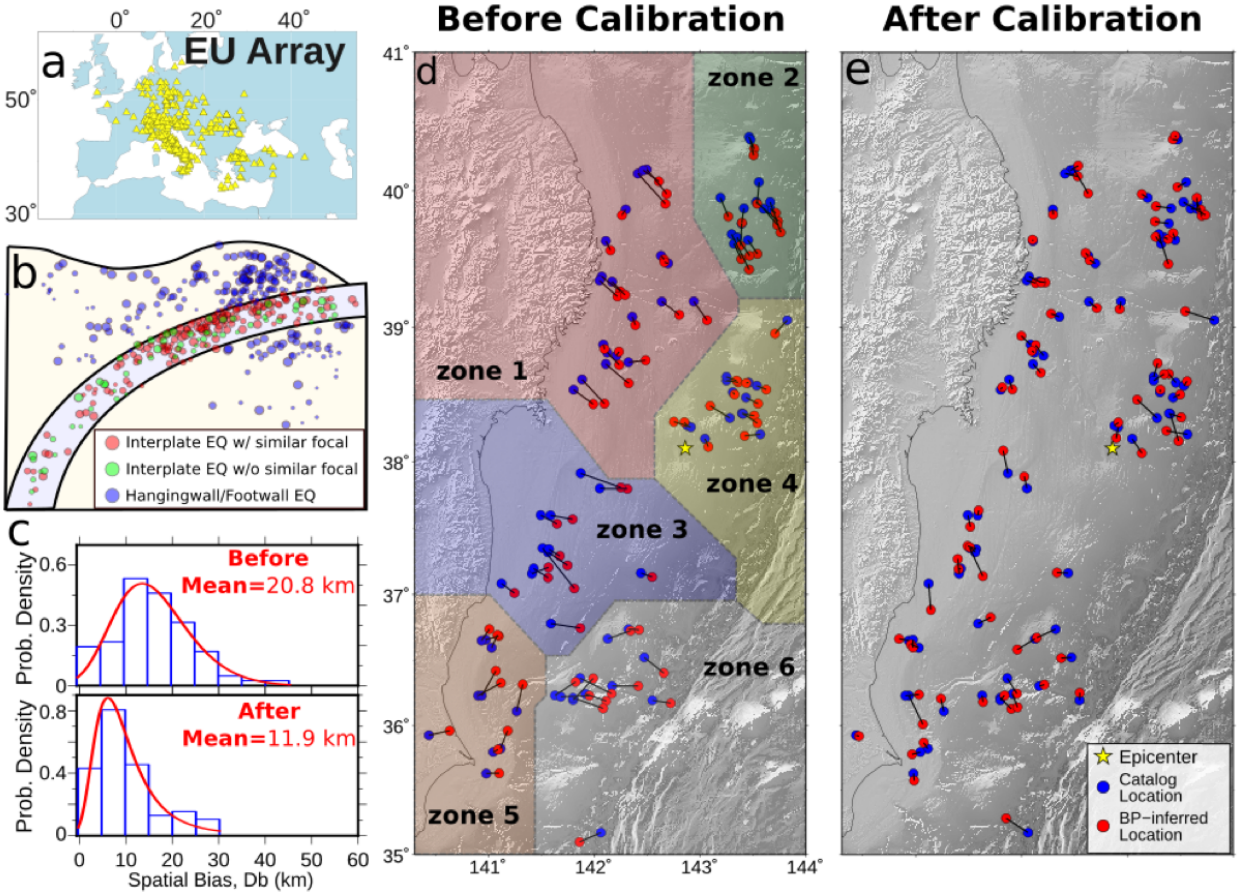
a
EU Array
0°
20°
40°
50°
30°
b
Interplate EQ w/ similar focal
Interplate EQ w/o similar focal
Hangingwall/Footwall EQ
c
Before
Mean=20.8 km
After
Mean=11.9 km
Prob. Density
Spatial Bias, Db (km)
Before Calibration
After Calibration
d
e
zone 1
zone 2
zone 3
zone 4
zone 5
zone 6
41°
40°
39°
38°
37°
36°
35°
141°
142°
143°
144°
Epicenter
Catalog Location
BP−inferred Location

Figure 7.2: **(EU array) The effectiveness of the slowness calibration of Back-projection.** (a) The EU array (369 stations) that is used in this study. (b) Illustration of the classification of seismic events in the subduction zone based on their relative distance to the slab interface and focal mechanisms. The group of interplate earthquakes with similar focal mechanisms (red circles) as that of the 2011 Mw 9.1 Tohoku earthquake are investigated here. The classification follows Asano et al., (2011). (c) Distribution of De of the 82 M4 M7 investigated interplate events with similar focal mechanisms as that of the 2011 Mw 9.1 Tohoku earthquake. The fitted probability density function (PDF) follows a generalized extreme value (GEV) distribution. (d) The spatial biases (black line) of the 82 events, as measured by De, the distance of the image peak (BPI location, red circle) from the epicenter (JMA location, blue circle). Colored regions are segmented automatically by K-means clustering based distribution of events' horizontal locations. (e) Same as (d) but after slowness calibration.

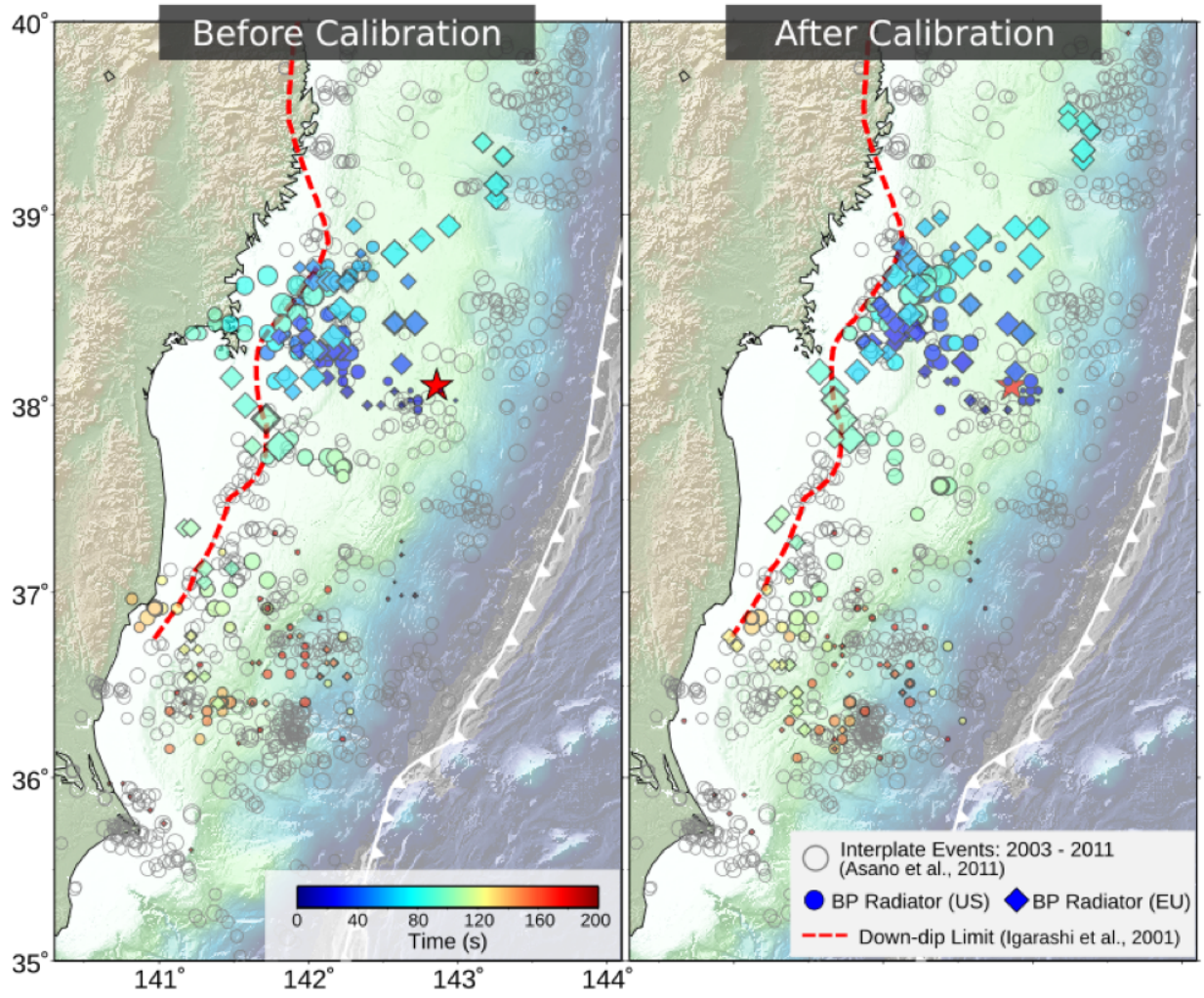

Figure 7.3: Coseismic rupture evolution of high-frequency (0.5–2 Hz) radiations before (left) and after (right) slowness calibration. BPs are imaged by US array (circle) and EU array (diamond), with sizes proportional to the relative energy and color that represents the rupture time. The red dashed line shows the down-dip limit of interplate seismicity (Igarashi et al., 2001).

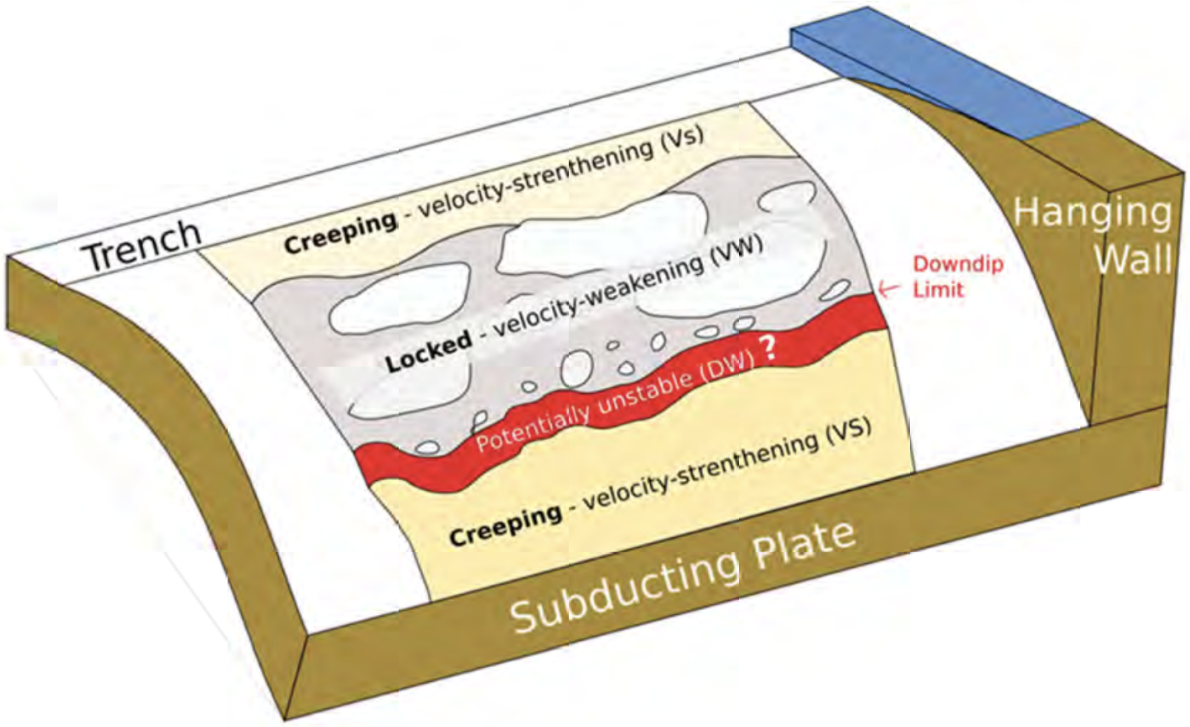

Figure 7.4: A conceptual model for the interplate megathrust fault. The seismic locked zones are controlled by velocity-weakening (VW) frictions while the creeping ductile zones are associated with velocity-strengthening (VS) frictions. Dramatic weakening (DW) activated at high slip rate is one candidate mechanism to explain deep penetration beyond the down-dip limit of interplate seismicity.

CHAPTER 8

Conclusions and Future Perspectives

8.1 Summary

We have shown that supershear earthquakes are less rare than people thought before, and that oceanic supershear earthquakes occur as frequently as continental ones. We have developed and optimized tools, and applied them to investigate supershear ruptures in a more consistent and more systematic way. In particular, motivated to better estimate rupture speed, we have developed and optimized the Slowness-Enhanced Back-projection method. The method mitigates spatial uncertainties of Back-projection from 20 km to 10 km, significantly increasing the accuracy of the method. On the other hand, by conducting synthetic test, we found a systematic underestimation of rupture speed using Back-projection. Eventually, we applied these enhanced methods on a total of 86 earthquakes from the last two decades and discovered four supershear earthquakes that had not been identified as such, while confirming the other eight previously reported ones. This is around 14% of all the examined earthquakes; more than twice as many as previously confirmed. While most previously reported supershear earthquakes were generated within continents, the newly discovered supershear earthquakes all occurred beneath the ocean.

This significant increase in the number of observed supershear earthquakes provides a much greater basis for evaluating the conditions favourable for driving supershear rupture. We observe that supershear rupture is more common along faults that separate oceanic and continental plates. As oceanic and continental crust have distinct compositions, this is con-

sistent with laboratory experiments that suggest supershear rupture is more sustainable on faults separating contrasting materials. These oceanic–continental supershear earthquakes also generally rupture in the same relative direction due to the contrasting interface, as the rupture prefers to propagate in the same direction that the stiffer fault block is moving in. Other factors that might affect the likelihood of supershear earthquakes occurring include the depth to which large earthquakes occur on the fault and fault zone maturity. We find that fault zone width is thicker in regions where supershear earthquakes occur, and that supershear ruptures occur relatively frequently in mature oceanic transform faults, as manifested by their wide fault zones.

Our work has increased the number of known supershear earthquakes by half, showing that while these events may still be rare, they appear to be much more prevalent among large, strike-slip earthquakes than previously thought. The additional information provided by these earthquakes confirms observations made from experiments and will be able to guide future research into these destructive earthquakes.

8.2 Future Perspectives

While these observations are important for understanding what influences whether a fault can sustain supershear rupture or not, the physical mechanism for driving supershear earthquakes is yet to be fully resolved. While the back-projection technique we used by can tell us about how the fault rupture migrates, it is still difficult to provide information regarding the fine-scale fault structure that slips. These details are important because their rupture speed estimates are made based on the assumption of the fault being straight. It remains unclear as to whether supershear earthquakes can occur on straight faults or whether non-planar faults are needed, and how fast rupture can occur in mature fault zones that are likely to have multiple slip surfaces. The additional supershear observations we identified will be able to guide further detailed analysis of earthquake seismic data, as well as numerical simulations

and laboratory experiments that should include representation of mature faults with realistic geometries and wide fault damage zones.

8.2.1 Identifying New Supershear Earthquakes

Our studies set up a benchmark of identifying supershear earthquakes, which applies teleseismic back-projection imaging and the Mach wave method. We show that such a combination is very effective in resolving rupture speeds of supershear earthquakes. Therefore, for future earthquakes, seismologists can use these methods to quickly screen earthquakes' rupture speed. One can also exhaust earthquakes that occurred before 2000. Although seismic networks before 2000 are not as widely distributed as that after 2000, identifying supershear earthquakes with sparser networks are still worth trying. Moreover, we demonstrate that investigating supershear earthquakes in a consistent, systematic way, more like a global survey help drawing conclusion from a more fundamental perspective, for instance, the bimateral effect we studied in Bao et al., 2022. Future studies can apply other methods to do similar type of studies, for example, using near fault S-wave to confirm a supershear rupture speed (Ellsworth et al., 2004). One can also use datasets of source time functions of earthquakes (e.g., SCARDEC) to study rupture speed, for example, Chounet et al., 2018 developed a new catalog of rupture velocities and directions for 96 shallow earthquakes based on SCARDEC dataset of earthquake sources.

8.2.2 Application of the Supershear Earthquakes Dataset

With the newly developed and newly confirmed set of supershear earthquakes, seismologist can conduct more numerical studies to better understand physics of rupture speeds. First, a systematic revisit of slip models of all the confirmed supershear events can help better understand factors that control supershear transition and propagation. In particular, most finite fault inversions have over-simplified assumptions of fault geometry as a single or

multiple-fault-plane model. However, there are several newly developed inversion method (e.g., Shimizu et al., 2019) that allows more freedom like fault geometries. One can use these more advanced inversion method to investigate controlling factors of supershear transition and propagation, for example, fault geometry, rake angle, and fracture energy ratio. On the other hand, one may argue that finite fault models are affected by inherent non-uniqueness so dynamic rupture modelling may also be applied to reproduce the physical process that govern the way the fault yields and slides, for events from the established supershear earthquake dataset.

Bibliography

Andrews, D. J. (1976). Rupture Velocity of Plane Strain Shear Cracks. *Journal of Geophysical Research*, *81*(32).

Andrews, D. J., & Ben-Zion, Y. (1997). Wrinkle-like slip pulse on a fault between different materials. *Journal of Geophysical Research: Solid Earth*, *102*(B1), 553–571.

Antolik, M., Abercrombie, R. E., & Ekström, G. (2004). The 14 November 2001 Kokoxili (Kunlunshan), Tibet, Earthquake: Rupture transfer through a large extensional step-over. *Bulletin of the Seismological Society of America*, *94*(4), 1173–1194.

Archuleta, R. J. (1984). 1. A faulting model for the 1979 Imperial Valley earthquake. *Journal of Geophysical Research*, *89*, 4559–4585.

Asano, Y., Saito, T., Ito, Y., Shiomi, K., Hirose, H., Matsumoto, T., Aoi, S., Hori, S., & Sekiguchi, S. (2011). Spatial distribution and focal mechanisms of aftershocks of the 2011 off the pacific coast of tohoku earthquake. *Earth, Planets and Space*, *63*(7), 669–673.

Bao, H., Ampuero, J.-P., Meng, L., Fielding, E. J., Liang, C., Milliner, C. W., Feng, T., & Huang, H. (2019). Early and persistent supershear rupture of the 2018 magnitude 7.5 palu earthquake. *Nature Geoscience*, *12*(3), 200–205.

Barka, A. (1999). The 17 august 1999 izmit earthquake. *Science*, *285*(5435), 1858–1859.

Benioff, H. (1955). Mechanism and strain characteristics of the White Wolf fault as indicated by the aftershock sequence. *Calif. Div. Mines and Geol. Bull.*, *171, 199-2*.

Benioff, H., Press, F., & Smith, S. (1961). Excitation of the Free Oscillations of the Earth by Earthquakes. *66*(2).

Ben-Menahem, A., & Toksoz, M. N. (1963). Source Mechanism from Spectrums of Long-Period Surface Waves 2. The Kamchatka Earthquake of November 4, 1952. *Journal of Geophysical Research*, *68*(18).

Ben-Menahem, A., & Toksöz, M. N. (1963). "source mechanism from spectrums of long-period surface waves: 2. the kamchatka earthquake of november 4,1952". *Journal of Geophysical Research*, *68*(18), 5207–5222.

Beresnev, I. A. (2003). Uncertainties in finite-fault slip inversions: To what extent to believe? (a critical review). *Bulletin of the Seismological Society of America*, *93*(6), 2445–2458.

Bernard, P., & Baumont, D. (2005). Shear mach wave characterization for kinematic fault rupture models with constant supershear rupture velocity. *Geophysical Journal International*, *162*(2), 431–447.

Bizzarri, A., Dunham, E. M., & Spudich, P. (2010). Coherence of mach fronts during heterogeneous supershear earthquake rupture propagation: Simulations and comparison with observations. *Journal of Geophysical Research*, *115*(B8).

Bouchon, M., Karabulut, H., Bouin, M. P., Schmittbuhl, J., Vallée, M., Archuleta, R., Das, S., Renard, F., & Marsan, D. (2010). Faulting characteristics of supershear earthquakes. *Tectonophysics*, *493*(3-4), 244–253.

Bouchon, M., Karabulut, H., Nail, M., & Dietrich, M. (2001). How Fast is Rupture during an Earthquake ? New Insights from the 1999 Turkey Earthquakes. *28*(14), 2723–2726.

Bouchon, M., Toksz, N., Dietrich, M., Aktar, M., & Edie, M. (2000). Seismic Imaging of the 1999 Izmit (Turkey) Rupture Inferred from the Near-Fault Recordings. *Geophysical Research Letters*, *27*(18), 3013–3016.

Bouchon, M., & Vallée, M. (2003). Observation of long supershear rupture during the magnitude 8.1 Kunlunshan earthquake. *Science*, *301*(5634), 824–826.

Bruhat, L., Fang, Z., & Dunham, E. M. (2016). Rupture complexity and the supershear transition on rough faults. *Journal of Geophysical Research: Solid Earth*, *121*(1), 210–224.

Burridge, R. (1973). Admissible speeds for plane-strain self-similar shear cracks with friction but lacking cohesion. *Geophysical Journal International*, *35*(4), 439–455.

Capon, J., & Berteussen, K. A. (1974). A random medium analysis of crust and upper mantle structure under norsar. *Geophysical Research Letters*, *1*(7), 327–328.

Chounet, A., Vallée, M., Causse, M., & Courboulex, F. (2018). Global catalog of earthquake rupture velocities shows anticorrelation between stress drop and rupture velocity. *Tectonophysics*, *733*, 148–158.

Cummins, P. R. (2017). Geohazards in indonesia: Earth science for disaster risk reduction – introduction. *Geological Society, London, Special Publications*, *441*(1), 1–7.

Das, S. (1976). A numerical study of rupture propagation and earthquake source mechanism dsc thesis. *Massachusetts Institute of Technology, Cambridge*.

Das, S. (2015). Supershear Earthquake Ruptures – Theory , Methods , Laboratory Experiments and Fault Superhighways : An Update. *Geotechnical, Geological and Earthquake Engineering*, *34*, 1–21.

Das, S., & Aki, K. (1977). A numerical study of two-dimensional spontaneous rupture propagation. *Geophysical Journal of the Royal Astronomical Society*, *50*(3), 643–668.

DeMets, C., Gordon, R. G., Argus, D. F., & Stein, S. (1990). Current plate motions. *Geophysical Journal International*, *101*(2), 425–478.

DeMets, C., Gordon, R. G., & Argus, D. F. (2010). Geologically current plate motions. *Geophysical Journal International*, *181*(1), 1–80.

Dunham, E. M. (2005). Near-source ground motion from steady state dynamic rupture pulses. *Geophysical Research Letters*, *32*(3).

Dunham, E. M. (2007). Conditions governing the occurrence of supershear ruptures under slip-weakening friction. *Journal of Geophysical Research: Solid Earth*, *112*(7), 1–24.

Dunham, E. M., & Archuleta, R. J. (2004). 4. Evidence for a supershear transient during the 2002 Denali fault earthquake. *Bulletin of the Seismological Society of America*, *94*, 256–268.

Dunham, E. M., & Bhat, H. S. (2008). Attenuation of radiated ground motion and stresses from three-dimensional supershear ruptures. *Journal of Geophysical Research: Solid Earth*, *113*(B8).

Duputel, Z., Kanamori, H., Tsai, V. C., Rivera, L., Meng, L., Ampuero, J.-P., & Stock, J. M. (2012). The 2012 sumatra great earthquake sequence. *Earth and Planetary Science Letters*, *351-352*, 247–257.

Ekström, G., Nettles, M., & Dziewoński, A. (2012). The global cmt project 2004–2010: Centroid-moment tensors for 13,017 earthquakes. *Physics of the Earth and Planetary Interiors*, *200-201*, 1–9.

Ellsworth, W. L., Celebi, M., Evans, J. R., Jensen, E. G., Kayen, R., Metz, M. C., Nyman, D. J., Roddick, J. W., Spudich, P., Stephens, C. D., & et al. (2004). Near-field ground motion of the 2002 denali fault, alaska, earthquake recorded at pump station 10. *Earthquake Spectra*, *20*(3), 597–615.

Fan, W., & Shearer, P. M. (2016). Local near instantaneously dynamically triggered aftershocks of large earthquakes. *Science*, *353*(6304), 1133–1136.

Fan, W., & Shearer, P. M. (2017). Investigation of Backprojection Uncertainties With M6 Earthquakes. *Journal of Geophysical Research: Solid Earth*, *122*(10), 7966–7986.

Feng, T., Meng, L., & Huang, H. (2020). Detecting offshore seismicity: Combining backprojection imaging and matched-filter detection. *Journal of Geophysical Research: Solid Earth*, *125*(8).

Fialko, Y., Sandwell, D., Simons, M., & Rosen, P. (2005). Three-dimensional deformation caused by the bam, iran, earthquake and the origin of shallow slip deficit. *Nature*, *435*(7040), 295–299.

Frankel, A. (2004). Rupture process of the M 7.9 Denali fault, Alaska, earthquake: Subevents, directivity, and scaling of high-frequency ground motions. *Bulletin of the Seismological Society of America*, *94*(6 SUPPL. B), 234–255.

Freund, L. B. (1979). The mechanics of dynamic shear crack propagation. *Journal of Geophysical Research*, *84*(B5), 2199.

Fukahata, Y., Yagi, Y., & Rivera, L. (2013). Theoretical relationship between back-projection imaging and classical linear inverse solutions. *Geophysical Journal International*, *196*(1), 552–559.

Gabriel, A.-A., Ampuero, J.-P., Dalguer, L. A., & Mai, P. M. (2013). Source properties of dynamic rupture pulses with off-fault plasticity. *Journal of Geophysical Research: Solid Earth*, *118*(8), 4117–4126.

Graham, S. E., DeMets, C., DeShon, H. R., Rogers, R., Maradiaga, M. R., Strauch, W., Wiese, K., & Hernandez, D. (2012). Gps and seismic constraints on the m = 7.3 2009 swan islands earthquake: Implications for stress changes along the motagua fault and other nearby faults. *Geophysical Journal International*, *190*(3), 1625–1639.

Gutenberg, B. (1955). Magnitude determination for larger kern county shocks, 1952; effects of station azimuth and calculation methods. *Calif. Div. Mines and Geol. Bull.*, *171*, 171–175.

Hartzell, S., & Helmberger, D. V. (1982). STRONG-MOTION MODELING OF THE IMPERIAL VALLEY EARTHQUAKE OF 1979. *Bulletin of the Seismological Society of America*, *72*(2), 571–596.

Hartzell, S. H., & Heaton, T. H. (1983). Inversion of strong ground motion and teleseismic waveform data for the fault rupture history of the 1979 imperial valley, california, earthquake. *Bulletin of the Seismological Society of America*, *73*(6A), 1553–1583.

Hayes, G. P. (2017). The finite, kinematic rupture properties of great-sized earthquakes since 1990. *Earth and Planetary Science Letters*, *468*, 94–100.

Hicks, S. P., Okuwaki, R., Steinberg, A., Rychert, C. A., Harmon, N., Abercrombie, R. E., Bogiatzis, P., Schlaphorst, D., Zahradnik, J., Kendall, J.-M., & et al. (2020). Back-propagating supershear rupture in the 2016 mw 7.1 romanche transform fault earthquake. *Nature Geoscience*, *13*(9), 647–653.

Huang, Y., Ampuero, J.-P., & Helmberger, D. V. (2016). The potential for supershear earthquakes in damaged fault zones – theory and observations. *Earth and Planetary Science Letters*, *433*, 109–115.

Ishii, M., Shearer, P. M., Houston, H., & Vidale, J. E. (2005). Extent, duration and speed of the 2004 sumatra–andaman earthquake imaged by the hi-net array. *Nature*, *435*(7044), 933–936.

Ishii, M., Shearer, P. M., Houston, H., & Vidale, J. E. (2007). Teleseismic P wave imaging of the 26 December 2004 Sumatra-Andaman and 28 March 2005 Sumatra earthquake ruptures using the Hi-net array. *Journal of Geophysical Research: Solid Earth*, *112*(11), 1–16.

Ito, A. (1985). High resolution relative hypocenters of similar earthquakes by cross-spectral analysis method. *Journal of Physics of the Earth*, *33*(4), 279–294.

Kagan, Y. Y. (1991). Likelihood analysis of earthquake catalogues. *Geophysical Journal International*, *106*(1), 135–148.

Kaneko, Y., & Lapusta, N. (2010). Supershear transition due to a free surface in 3-d simulations of spontaneous dynamic rupture on vertical strike-slip faults. *Tectonophysics*, *493*(3-4), 272–284.

Kehoe, H. L., & Kiser, E. D. (2020). Evidence of a supershear transition across a fault stepover. *Geophysical Research Letters*, *47*(10).

Kennet, B. L. (1991). Iaspei 1991 seismological tables. *Terra Nova*, *3*(2), 122–122.

Kikuchi, M., & Kanamori, H. (1991). Inversion of complex body waves—iii. *Bulletin of the Seismological Society of America*, *81*(6), 2335–2350.

Kiser, E., & Ishii, M. (2011). The 2010 Mw 8.8 Chile earthquake: Triggering on multiple segments and frequency-dependent rupture behavior. *Geophysical Research Letters*, *38*(7), 6–11.

Kiser, E., & Ishii, M. (2017). Back-Projection Imaging of Earthquakes. *Annual Review of Earth and Planetary Sciences*, *45*(1), 271–299.

Kogan, M. G., Frolov, D. I., Vasilenko, N. F., Freymueller, J. T., Steblov, G. M., Ekström, G., Titkov, N. N., & Prytkov, A. S. (2017). Plate coupling and strain in the far western aleutian arc modeled from gps data. *Geophysical Research Letters*, *44*(7), 3176–3183.

Koper, K. D., Hutko, A. R., Lay, T., & Sufri, O. (2012). Imaging short-period seismic radiation from the 27 February 2010 Chile (MW 8.8) earthquake by back-projection of P, PP, and PKIKP waves. *Journal of Geophysical Research: Solid Earth*, *117*(2), 1–16.

Kostrov, B. (1964). Selfsimilar problems of propagation of shear cracks. *Journal of Applied Mathematics and Mechanics*, *28*(5), 1077–1087.

Laske, G., Masters, G., Ma, Z., & Pasyanos, M. (2013). Update on CRUST1. 0—a 1-degree global model of Earth's crust. *Geophys. Res. Abstr.*, (15), 2658.

Lay, T., Ye, L., Bai, Y., Cheung, K. F., Kanamori, H., Freymueller, J., Steblov, G. M., & Kogan, M. G. (2017). Rupture Along 400 km of the Bering Fracture Zone in the Komandorsky Islands Earthquake (MW 7.8) of 17 July 2017. *Geophysical Research Letters*, *44*(24), 12, 161–12, 169.

Liu, Y., & Lapusta, N. (2008). Transition of mode ii cracks from sub-rayleigh to inter-sonic speeds in the presence of favorable heterogeneity. *Journal of the Mechanics and Physics of Solids*, *56*(1), 25–50.

Lutikov, A. I., Rogozhin, E. A., Dontsova, G. Y., & Zhukovets, V. N. (2019). The mw 7.8 earthquake of july 17, 2017 off the commander islands and other large earthquakes at the western segment of the aleutian island arc. *Journal of Volcanology and Seismology*, *13*(2), 112–123.

MacQueen, J. (1966). *Classification and analysis of multivariate observations*.

Madariaga, R. (1977). High-frequency radiation from crack (stress drop) models of earthquake faulting. *Geophysical Journal International*, *51*(3), 625–651.

Madariaga, R. (1983). High frequency radiation from dynamic earthquake. *Ann. Geophys*, *1*(17).

McFadden, D. (1978). Modeling the choice of residential location. *Transportation Research Record*, *673*, 72–77.

Melgar, D., & Hayes, G. P. (2017). Systematic observations of the slip pulse properties of large earthquake ruptures. *Geophysical Research Letters*, *44*(19), 9691–9698.

Meng, L., Ampuero, J.-P., Luo, Y., Wu, W., & Ni, S. (2012). Mitigating artifacts in back-projection source imaging with implications for frequency-dependent properties of the tohoku-oki earthquake. *Earth, Planets and Space*, *64*(12), 1101–1109.

Meng, L., Bao, H., Huang, H., Zhang, A., Bloore, A., & Liu, Z. (2018). Double pincer movement: Encircling rupture splitting during the 2015 Mw 8.3 Illapel earthquake. *Earth and Planetary Science Letters*, *495*, 164–173.

Meng, L., Huang, H., Xie, Y., Bao, H., & Dominguez, L. A. (2019). Nucleation and Kinematic Rupture of the 2017 Mw 8.2 Tehuantepec Earthquake. *Geophysical Research Letters*, *46*(7), 3745–3754.

Meng, L., Inbal, A., & Ampuero, J. P. (2011). A window into the complexity of the dynamic rupture of the 2011 Mw 9 Tohoku-Oki earthquake. *Geophysical Research Letters*, *38*(16), 1–6.

Meng, L., Zhang, A., & Yagi, Y. (2016). Improving back projection imaging with a novel physics-based aftershock calibration approach: A case study of the 2015 Gorkha earthquake. *Geophysical Research Letters*, *43*(2), 628–636.

Newberry, J. T., Laclair, D. L., & Fujita, K. (1986). Seismicity and tectonics of the far western aleutian islands. *Journal of Geodynamics*, *6*(1-4), 13–32.

Nielsen, S., & Madariaga, R. (2003). On the self-healing fracture mode. *Bulletin of the Seismological Society of America*, *93*(6), 2375–2388.

Oglesby, D. D. (2004). Inverse kinematic and forward dynamic models of the 2002 denali fault earthquake, alaska. *Bulletin of the Seismological Society of America*, *94*(6B).

Ohnaka, M., & Yamashita, T. (1989). A cohesive zone model for dynamic shear faulting based on experimentally inferred constitutive relation and strong motion source parameters. *Journal of Geophysical Research: Solid Earth*, *94*(B4), 4089–4104.

Okuwaki, R., Hirano, S., Yagi, Y., & Shimizu, K. (2020). Inchworm-like source evolution through a geometrically complex fault fueled persistent supershear rupture during the 2018 palu indonesia earthquake. *Earth and Planetary Science Letters*, *547*, 116449.

Okuwaki, R., Kasahara, A., Yagi, Y., Hirano, S., & Fukahata, Y. (2019). Backprojection to image slip. *Geophysical Journal International*, *216*(3), 1529–1537.

Okuwaki, R., & Yagi, Y. (2018). Role of geometric barriers in irregular-rupture evolution during the 2008 Wenchuan earthquake. *Geophysical Journal International*, *212*(3), 1657–1664.

Okuwaki, R., Yagi, Y., & Hirano, S. (2014). Relationship between high-frequency radiation and asperity ruptures, revealed by hybrid back-projection with a non-planar fault model. *Scientific Reports*, *4*, 1–6.

Olsen, K. B., Madariaga, R., & Archuleta, R. J. (1997). Three-dimensional dynamic simulation of the 1992 landers earthquake. *Science*, *278*(5339), 834–838.

Olson, A. H., & Apsel, R. J. (1982). FINITE FAULTS AND INVERSE THEORY WITH APPLICATIONS TO THE 1979 IMPERIAL VALLEY EARTHQUAKE. *Bulletin of the Seismological Society of America*, *72*(6), 1969–2001.

Oral, E., Weng, H., & Ampuero, J. P. (2020). Does a damaged-fault zone mitigate the near-field impact of supershear earthquakes?—application to the 2018 7.5 palu, indonesia, earthquake. *Geophysical Research Letters*, *47*(1).

Ozacar, A. A., & Beck, S. L. (2004). 4. The 2002 denali fault and 2001 kunlun fault earthquakes: Complex rupture processes of two large strike-slip events. *Bulletin of the Seismological Society of America*, *94*(6 SUPPL. B), 278–292.

Palo, M., Tilmann, F., Krüger, F., Ehlert, L., & Lange, D. (2014). High-frequency seismic radiation from Maule earthquake (Mw 8.8, 2010 February 27) inferred from high-

resolution backprojection analysis. *Geophysical Journal International*, *199*(2), 1058–1077.

Passelègue, F. X., Schubnel, A., Nielsen, S., Bhat, H. S., & Madariaga, R. (2013). From sub-Rayleigh to supershear ruptures during stick-slip experiments on crustal rocks. *Science*, *340*(6137), 1208–1211.

Perrin, C., Manighetti, I., Ampuero, J. P., Cappa, F., & Gaudemer, Y. (2016). Location of largest earthquake slip and fast rupture controlled by along-strike change in fault structural maturity due to fault growth. *Journal of Geophysical Research: Solid Earth*, *121*(5), 3666–3685.

Pesicek, J. D., Thurber, C. H., Zhang, H., Deshon, H. R., Engdahl, E. R., & Widiyantoro, S. (2010). Teleseismic double-difference relocation of earthquakes along the Sumatra-Andaman subduction zone using a 3-D model. *Journal of Geophysical Research: Solid Earth*, *115*(10), 1–20.

Reid, H. F. (1910). The machanism of the earthquake, in the california earthquake of april 18, 1906. *Report of the state earthquake investigation commission*, 16–28.

Robinson, D. P., Brough, C., & Das, S. (2006). Themw7.8, 2001 kunlunshan earthquake: Extreme rupture speed variability and effect of fault geometry. *Journal of Geophysical Research*, *111*(B8).

Rosakis, A. J., Samudrala, O., & Coker, D. (1999). Cracks faster than the shear wave speed. *Science*, *284*(5418), 1337–1340.

Rost, S., & Thomas, C. (2002). Array seismology: Methods and applications. *Reviews of Geophysics*, *40*(3).

Ruppert, N. A., Kozyreva, N. P., & Hansen, R. A. (2012). Review of crustal seismicity in the aleutian arc and implications for arc deformation. *Tectonophysics*, *522-523*, 150–157.

Ryan, K. J., & Oglesby, D. D. (2014). Dynamically modeling fault step overs using various friction laws. *Journal of Geophysical Research: Solid Earth*, *119*(7), 5814–5829.

Sangha, S., Peltzer, G., Zhang, A., Meng, L., Liang, C., Lundgren, P., & Fielding, E. (2017). Fault geometry of 2015, Mw7.2 Murghab, Tajikistan earthquake controls rupture propagation: Insights from InSAR and seismological data. *Earth and Planetary Science Letters*, *462*, 132–141.

Satriano, C., Kiraly, E., Bernard, P., & Vilotte, J.-P. (2012). The 2012 mw 8.6 sumatra earthquake: Evidence of westward sequential seismic ruptures associated to the reactivation of a n-s ocean fabric. *Geophysical Research Letters*, *39*(15).

Shi, Z., & Ben-Zion, Y. (2006). Dynamic rupture on a bimaterial interface governed by slip-weakening friction. *Geophysical Journal International*, *165*(2), 469–484.

Shimizu, K., Yagi, Y., Okuwaki, R., & Fukahata, Y. (2019). Development of an inversion method to extract information on fault geometry from teleseismic data. *Geophysical Journal International*, *220*(2), 1055–1065.

Shlomai, H., & Fineberg, J. (2016). The structure of slip-pulses and supershear ruptures driving slip in bimaterial friction. *Nature Communications*, *7*(1).

Socquet, A., Hollingsworth, J., Pathier, E., & Bouchon, M. (2019). Evidence of supershear during the 2018 magnitude 7.5 palu earthquake from space geodesy. *Nature Geoscience*, *12*(3), 192–199.

Song, S. G., Beroza, G. C., & Segall, P. (2008). A unified source model for the 1906 san francisco earthquake. *Bulletin of the Seismological Society of America*, *98*(2), 823–831.

Spudich, P., & Cranswick, E. (1984). 1979 Imperial Valley Earthquake Using a Short Baseline. *Bulletin of the Seismological Society of America*, *74*(6), 2083–2114.

Tadapansawut, T., Okuwaki, R., Yagi, Y., & Yamashita, S. (2021). Rupture process of the 2020 caribbean earthquake along the oriente transform fault, involving supershear rupture and geometric complexity of fault. *Geophysical Research Letters*, *48*(1).

Tinti, E. (2005). A kinematic source-time function compatible with earthquake dynamics. *Bulletin of the Seismological Society of America*, *95*(4), 1211–1223.

Uchide, T., Yao, H., & Shearer, P. M. (2013). Spatio-temporal distribution of fault slip and high-frequency radiation of the 2010 el mayor-cucapah, mexico earthquake. *Journal of Geophysical Research: Solid Earth*, *118*(4), 1546–1555.

Vallée, M., & Dunham, E. M. (2012). Observation of far-field Mach waves generated by the 2001 Kokoxili supershear earthquake. *Geophysical Research Letters*, *39*(5), 1–5.

Vallée, M., Landès, M., Shapiro, N. M., & Klinger, Y. (2008). The 14 November 2001 Kokoxili (Tibet) earthquake: High-frequency seismic radiation originating from the transitions between sub-Rayleigh and supershear rupture velocity regimes. *Journal of Geophysical Research: Solid Earth*, *113*(7), 1–14.

Vallée, M., & Satriano, C. (2014). Ten year recurrence time between two major earthquakes affecting the same fault segment. *Geophysical Research Letters*, *41*(7), 2312–2318.

Vyas, J. C., Mai, P. M., Galis, M., Dunham, E. M., & Imperatori, W. (2018). Mach wave properties in the presence of source and medium heterogeneity. *Geophysical Journal International*, *214*(3), 2035–2052.

Wald, D. J., & Heaton, T. H. (1994). Spatial and temporal distribution of slip for the 1992 landers, california, earthquake. *Bulletin of the Seismological Society of America*, *84*(3), 668–691.

Walker, K. T., & Shearer, P. M. (2009). Illuminating the near-sonic rupture velocities of the intracontinental kokoxili mw7.8 and denali fault mw7.9 strike-slip earthquakes with global p wave back projection imaging. *Journal of Geophysical Research*, *114*(B2).

Wang, D., & Mori, J. (2011). Frequency-dependent energy radiation and fault coupling for the 2010 Mw8.8 Maule, Chile, and 2011 Mw9.0 Tohoku, Japan, earthquakes. *Geophysical Research Letters*, *38*(22), 1–6.

Wang, D., Mori, J., & Koketsu, K. (2016). Fast rupture propagation for large strike-slip earthquakes. *Earth and Planetary Science Letters*, *440*, 115–126.

Wang, D., Mori, J., & Uchide, T. (2012). Supershear rupture on multiple faults for the Mw 8.6 off Northern Sumatra, Indonesia earthquake of April 11, 2012. *Geophysical Research Letters*, *39*(21), 6–10.

Weertman, J. (2002). Subsonic type earthquake dislocation moving at approximately × shear wave velocity on interface between half spaces of slightly different elastic constants. *Geophysical Research Letters*, *29*(10).

Weng, H., & Ampuero, J.-P. (2019). The dynamics of elongated earthquake ruptures. *Journal of Geophysical Research: Solid Earth*, *124*(8), 8584–8610.

Weng, H., & Ampuero, J.-P. (2020). Continuum of earthquake rupture speeds enabled by oblique slip. *Nature Geoscience*, *13*(12), 817–821.

Wu, F. T., THOMSON, K. C., & KUENZLER, H. (1972). STICK-SLIP PROPAGATION VELOCITY AND SEISMIC SOURCE MECHANISM. *87*(6), 8675–8683.

Xia, K., Rosakis, A. J., & Kanamori, H. (2004). Laboratory earthquakes: The sub-rayleigh-to-supershear rupture transition. *Science*, *303*(5665), 1859–1861.

Xia, K., Rosakis, A. J., Kanamori, H., & Rice, J. R. (2005). Laboratory earthquakes along inhomogeneous faults: Directionality and supershear. *Science*, *308*(5722), 681–684.

Xie, Y., Bao, H., & Meng, L. (2021). Source imaging with a multi-array local back-projection and its application to the 2019 mw 6.4 and mw 7.1 ridgecrest earthquakes. *Journal of Geophysical Research: Solid Earth*, *126*(10).

Xu, X., Tong, X., Sandwell, D. T., Milliner, C. W., Dolan, J. F., Hollingsworth, J., Leprince, S., & Ayoub, F. (2016). Refining the shallow slip deficit. *Geophysical Journal International*, *204*(3), 1843–1862.

Yao, H., Shearer, P. M., & Gerstoft, P. (2013). Compressive sensing of frequency-dependent seismic radiation from subduction zone megathrust ruptures. *Proceedings of the National Academy of Sciences*, *110*(12), 4512–4517.

Yin, J., & Denolle, M. A. (2019). Relating teleseismic backprojection images to earthquake kinematics. *Geophysical Journal International*, *217*(2), 729–747.

Yoffe, E. H. (1951). Lxxv. the moving griffith crack. *The London, Edinburgh, and Dublin Philosophical Magazine and Journal of Science*, *42*(330), 739–750.

Yue, H., Lay, T., Freymueller, J. T., Ding, K., Rivera, L., Ruppert, N. A., & Koper, K. D. (2013). 6. Supershear rupture of the 5 January 2013 Craig, Alaska (Mw7.5) earthquake. *Journal of Geophysical Research: Solid Earth*, *118*(11), 5903–5919.

Yue, H., Lay, T., & Koper, K. D. (2012). En échelon and orthogonal fault ruptures of the 11 april 2012 great intraplate earthquakes. *Nature*, *490*(7419), 245–249.

Zeng, Shengji, W., & Wenbo, W. (2019). Sources of uncertainties and artifacts in back-projection results. *Geophysical Journal International*.

Zeng, Y. (2001). Viscoelastic stress-triggering of the 1999 hector mine earthquake by the 1992 landers earthquake. *Geophysical Research Letters*, *28*(15), 3007–3010.

Zhan, Z., Helmberger, D. V., Kanamori, H., & Shearer, P. M. (2014). Supershear rupture in a Mw 6.7 aftershock of the 2013 Sea of Okhotsk earthquake. *Science*, *345*(6193), 1–4.